

BULGARIAN CHEMICAL COMMUNICATIONS

2024

Volume 56 / Number 1

*Journal of the Chemical Institutes
of the Bulgarian Academy of Sciences
and of the Union of Chemists in Bulgaria*

Application of mobile fluorescence spectroscopy as a method in the determination of varietal differences in black radish (*Raphanus sativus* L. var. Niger) during storage under uncontrolled conditions

V. Slavova

Department of Plant Breeding, Maritsa Vegetable Crops Research Institute, Agricultural Academy, 32, Brezovsko Chaussee, Plovdiv 4003, Bulgaria

Received: September 19, 2023; Revised: January 10, 2024

The present study aims to establish the application of mobile fluorescence spectroscopy as a method to determine varietal differences and water content during storage of black radish (*Raphanus sativus* L. var. Niger) under uncontrolled conditions. The experimental studies were carried out on the farm where the black radish was grown and stored. Fluorescence analysis was performed with a source with an emission wavelength of 285 nm, using an author-developed mobile set up in a fiber-optic configuration generating fluorescence signals. The subject of this research were root crops from Black Spanish round, Black Spanish long, Rattail and Nero Tondo. They were measured after harvesting after 3 and 6 months of storage. The correlation between the emission wavelengths of the samples of different varieties, as well as those of the same variety at different storage intervals, was established. This fact allows mobile fluorescence spectroscopy to be successfully applied as a rapid tool in black radish breeding programs in establishing the origin of unknown root crops in the presence of a rich library of spectra, as well as in the sorting of black radishes in warehouses of food chains and producers. The results of the experiment can be used to optimize the time for the analysis of varietal affiliation of different black radish genotypes during storage under uncontrolled conditions. Fluorescence spectroscopy in a fiber-optic configuration will support the process of determining the affiliation of a particular black radish variety to a given variety (even for samples of unknown origin when it is necessary to qualify and sort in a short time).

Keywords: black radish accessions, fluorescence spectroscopy, variety, emission wavelength, storage under uncontrolled conditions.

INTRODUCTION

The black radish (*Raphanus sativus* L. var. Niger) is a two-year root plant, which in the first year forms a rosette of leaves and a root, and in the second forms a flower-bearing stem [1]. Black radish is common in many places in Europe and Asia (mostly in Korea, China and Japan) [2]. This cultivated plant has a rich chemical composition. It is a source of vitamin A, vitamin B2, vitamin C, vitamin P and vitamin K. The root vegetable contains potassium, calcium, magnesium, phosphorus, etc [3, 4]. This type of turnip is a source of glucosides, pectin, etc [5].

Using liquid chromatography, the oil content of the seeds of selected vegetable crops was found to vary between 15.89 g/100 g (purslane) and 38.97 g/100 g (black radish) [6]. The palmitic acid content of the oil samples was between 2.2 g/100 g (turnip) and 15.0 g/100 g (purslane) [7]. The linoleic acid content of the oils was between 8.9% (black radish) and 57.0% (onion) [8].

The present study aims to establish the function of fluorescence spectroscopy as a mobile method for the analysis of representatives of different varieties of black radish (*Raphanus sativus* L. var. Niger J.

Kern) during storage under uncontrolled conditions. The accessions were kept under uncontrolled storage conditions. This will permit the technique to be applied non-invasively in the quality control of black radish production in unspecified storage outdoors.

MATERIALS AND METHODS

Materials

Accessions from four standard black radish varieties were investigated:

Black Spanish round - root crops are globose, up to 2-1/2 inches in diameter, with crisp hot white flesh that holds well after picking. The variety can be sown from early spring, and the harvest is in winter if sown in July-August.

Black Spanish long - a large-root crop vegetable, dark brown with long pointed roots and white flesh. It can be left in the ground and harvested in winter or stored in dry sand in a frost-free shed. It is believed to aid digestion and is high in antioxidants.

Rattail - root crops are flat-oval to oblong, with an intensively obtuse eye on the surface, with a diameter of 10-12 cm. The covering of the roots is black, and the core is a white, dense and spicy flesh. The accessions of this variety withstand more severe winter conditions during the growing season.

* To whom all correspondence should be sent:
E-mail: vania_plachkova@abv.bg

Nero Tondo - this elite variety is much more uniform and resistant to curling than the common black Spanish variety. Large 2–4" (depending on harvest date) black, round roots with crisp, hot, white flesh. Suitable for mid-spring sowing (soil temperature 60°F/16°C or higher, to prevent warping) until autumn, medium long storage.

Black radishes are harvested in dry sunny weather in the morning. After they are washed, they are spread out on a linen cloth and left to dry well, being turned periodically. The black radishes are dried for 2-3 hours in the sun and then for 7-10 days in a well-ventilated place. Their tops are cut in two stages. The first stage is to cut off just above the root crop, the second stage is to cut off the top of the black radish by 1 cm. Immediately before storage, the black radishes are sorted and only healthy and undamaged root vegetables are set aside for long-term storage. They are stored in a dry warehouse at an average temperature of 4-7 °C.

Fluorescence spectroscopy:

Accessions of four different varieties of black radish storage under uncontrolled conditions were subjected to fluorescence spectroscopic measurements. The mobile spectral installation (Fig. 1) for the study of fluorescence signals was designed specifically for the rapid analysis of plant biological samples.

The mobile experimental installation for fluorescence spectroscopy contains the following blocks:

- A laser diode (LED) with an emission radiation of 245 nm with a supply voltage in the range of 3c V. It is housed in a hermetically sealed TO39 metal housing. The emitter has a voltage drop from 1.9 to 2.4 V and a current consumption of 0.02 A. The minimum value of its reverse voltage is – 6 V.
- Forming optic, which is a hemispherical lens

made of N-BAK2 glass. The post-LED forming optic is defined mainly for its refractive, dispersive and thermo-optical properties, as well as for its transparency in the UV range [240-280 nm].

- Quartz glass area of 4 cm². Its optical properties are to be transparent to visible light and to ultraviolet rays. This allows it to be free of inhomogeneities that scatter light. Its optical and thermal properties exceed those of other types of glass due to its purity. Light absorption in quartz glasses is weak.

- CMOS detector with photosensitive area of 1.9968×1.9968 mm. Its sensitivity ranges from 200 nm to 1100 nm. Its resolution is $\delta\lambda = 5$. The profile of the detector sensor projections along the X and Y axes is also designed for very small amounts of data, unlike widely used sensors.

The obtained fluorescence spectroscopic data were subjected to statistical analysis to distinguish 4 different varieties of black radish during storage under uncontrolled conditions.

RESULTS AND DISCUSSION

Prolonged storage of black radish root crops under uncontrolled conditions leads to a decrease in their water content. This process is directly proportional to the duration of storage.

The optical properties of the black radish are determined by its energy structure, which includes both the occupied and free electronic energy levels, as well as the energy levels of the atomic vibrations of the molecules or the crystal lattice. The possible transitions between these energy levels, as a function of photon energy, are specific to the black radish, resulting in spectra and optical properties unique to it. Black radishes contain particles smaller than the wavelength of visible light. Particles in the turbid medium, such as the black radish, act as independent light sources, emitting incoherently, causing the samples to visibly fluoresce.

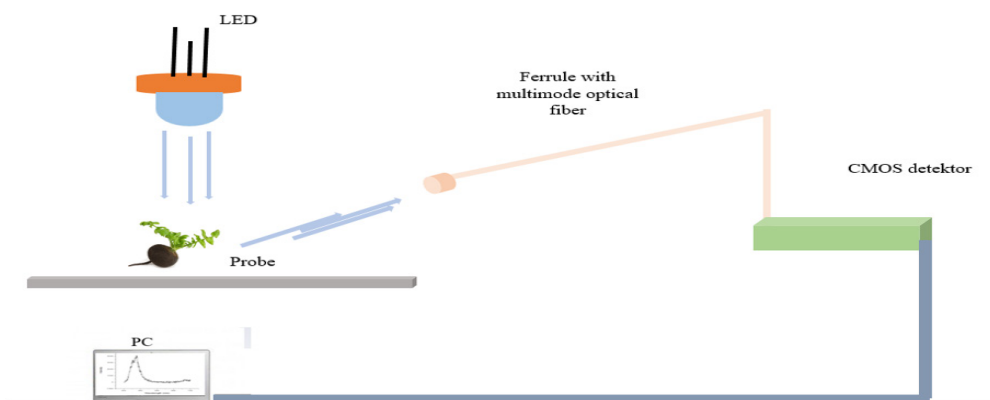


Fig. 1. Mobile experimental installation for fluorescence spectroscopy

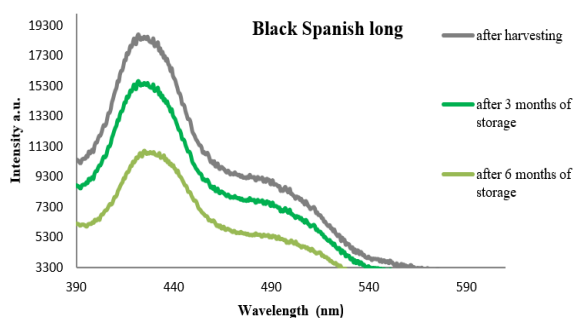


Fig. 2. Difference in emission wavelengths of Black Spanish long variety accessions after harvesting and storage for 3 and 6 months.

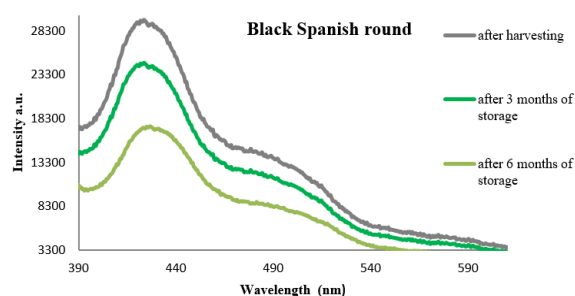


Fig. 3. Difference in emission wavelengths of Black Spanish round variety accessions after harvesting and storage for 3 and 6 months.

Therefore, fluorescence spectroscopy finds application for analysis of this vegetable crop. The optical parameters and spectral properties also change as a function of temperature, pressure, external electric and magnetic fields, etc., which allows obtaining essential information about changes in the chemical and cellular morphological composition of the black radish. The analysis of the graphs established the application of fluorescence spectroscopy for the analysis of root crops during storage in a warehouse under uncontrolled conditions for a period of 3 and 6 months (Figures 2, 3, 4 and 5). The decrease in signal intensity is directly proportional to the duration of storage (and it, in turn, is related to a decrease in root water content due to evaporation).

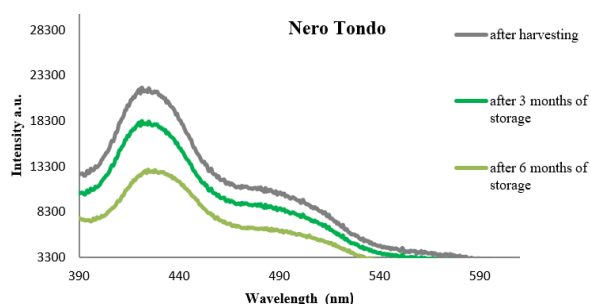


Fig. 4. Difference in emission wavelengths of Nero Tondo variety accessions after harvesting and storage for 3 and 6 months.

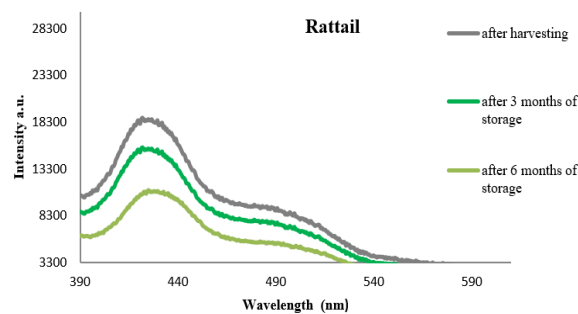


Fig. 5. Difference in emission wavelengths of Rattail variety accessions after harvesting and storage for 3 and 6 months.

The signal intensity is high enough at very low water content, which means that the method is applicable to controlling the quality of root crops during long-term storage of black radishes in storage rooms under uncontrolled conditions. An essential point in fluorescence diagnostics regarding the comparison of accessions after harvesting and after a certain period of storage is that the method is highly sensitive in terms of determining the water content of root crops of black radish stored in a storage room under uncontrolled conditions. This fact allows fluorescence spectroscopy to be applied as a non-invasive method in quality analysis of black radish production kept in storage rooms of farms and commercial establishments.

A literature survey was performed to conduct similar research. It turned out that until now the described experimental approach for the analysis of root crops of black radish has not been applied nationally and internationally.

This gives us reason to claim that mobile fluorescence spectroscopy in a fiber optic configuration has been applied for the first time to analyze black radish samples for their water content and root stability when kept in a storage room under uncontrolled conditions. The three main advantages of fluorescence spectroscopy are that the method is fast, does not require consumables, and can be performed on-site in the warehouse. The decision for local measurements was made to avoid damage to the samples during transport and thus, to ensure fluorescence analysis with high sensitivity.

CONCLUSIONS

- The method of mobile fluorescence spectroscopy is fast-acting in determining the water content of black radishes during storage of the product.
- The method of mobile fluorescence spectroscopy is applicable in controlling the

germination quality of root crops from black radish during storage.

- It was proven that mobile fluorescence spectroscopy will support the breeding process and the control of stock production of black radishes when it is necessary to qualify a large set of samples in a short time.

- A systematic engineering approach for the alignment (optical tuning) of a dedicated mobile fluorescence spectroscopy applied research facility was found to be applicable in the characterization of produced black radish during storage.

Acknowledgement: I express my gratitude to Mrs. Minka Serinska, in whose farm the black radishes were grown and stored, as well as to the entire team of the farm. Without their help, the research would not have been carried out.

REFERENCES

1. B. Matthäus, E. E. Babiker, M. M. Özcan, F. Y. Al-Juhaimi, I. A. Mohamed Ahmed, K. Ghafoor, *J. Oleo Sci.*, **70** (11), 1607 (2021).
2. B. K. Singh, *Vegetable Crops*, 275 (2021).
3. E. Sipiencie, I. Misina, A. Grygier, Y. Qian, M. Rudzinska, E. Kaufmane, D. Seglin, A. Siger, P. Gornas, *Scientia Horticulturae*, **275**, 1083 (2021).
4. H. Jeon, S. Oh, E. Kum, S. Seo, Y. Park, G. Kim, *Pharmaceuticals*, **15**, 1376 (2022).
5. A. Grygier, S. Chakradhari, K. Ratusz, M. Rudzińska, K. S. Patel, D. Lazdiņa, P. Górnaś, *Industrial Crops and Products*, **186**, 251 (2022).
6. E. Njumbe Ediage, J. D. Di Mavungu, M. L. Scippo, Y. J. Schneider, Y. Larondelle, A. Callebaut, J. Robbens, C. Van Peteghem, S. De Saeger, *Journal of Chromatography A*, **1218**, 4395 (2011).
7. A. Yücepepe, G. Altin, B. Özçelik, *Food Science and Technology*, **56**, 1376 (2021).
8. F. Barimani, A. A. Gholami, M. Nabili, *International Journal of Molecular Microbiology*, **10**, 1360 (2020).

Microwave activation of isovaleric acid monoglyceride synthesis and its antimicrobial activity

N. O. Appazov^{1,2*}, M. I. Syzdykbayev³, A. N. Appaz³, E. A. Nazarov¹, K. Kh. Darmagambet¹, G. T. Balykbayeva¹, B. B. Abzhalelov¹, G. Sh. Askarova¹, Yu. A. Kim⁴

¹Korkyt Ata Kyzylorda University, 29A AYTEKE BI STR., KYZYLORDA, REPUBLIC OF KAZAKHSTAN

²Limited Liability Partnership "DPS-Kyzylorda", 11A Amangeldi Str., Kyzylorda, Republic of Kazakhstan

³Nazarbayev Intellectual School Chemical-Biological Direction in Kyzylorda, 6 Sultan Beybars Str., Kyzylorda, Republic of Kazakhstan

⁴Institute of Cell Biophysics of the Russian Academy of Sciences, 3 Institutskaya Str., Pushchino, Moscow Region, Russian Federation

Received: October 01, 2023; Accepted: January 10, 2024

The article describes the microwave synthesis of isovaleric acid monoglyceride by the isopropylidene method using microwave-assisted synthesis. The yield of the target product was 94%. The resulting compound was characterized by ¹H NMR, ¹³C NMR, IR spectroscopy and elemental analysis. The resulting product was studied for antibacterial and antifungal activity. It was found that isovaleric acid monoglyceride has pronounced antibacterial activity against *Pseudomonas aeruginosa* and moderate antifungal activity against *Candida albicans*.

Keywords: microwave-assisted synthesis, isopropylidene protection, isovaleric acid monoglyceride, antibacterial and antifungal activity.

INTRODUCTION

Carboxylic acid esters, representing a large and important class of organic compounds, are widely distributed in nature in the form of essential oils, fats, waxes, phosphatides, tannins and have a variety of applications as solvents, extractants, for preparation of lacquers, drying oils, etc. [1-3]. Many resins and synthetic fibres are produced based on polyesters of polyfunctional acids and polyatomic alcohols. Esters of short- and medium-chain carboxylic acids with short- and medium-chain alcohols, having a pleasant smell, are used as scented substances in perfumery, cosmetic products and sweet-smelling food essences [4,5].

Esters of polyatomic alcohols and carboxylic acids are widely distributed in nature and many of them have biological activity. All fats and oils of vegetable and animal origin almost entirely consist of glycerol esters (triglycerides). Another important class of natural substances present in plants are tannins which are partially a mixture of various esters of gallic acid and glucose [6-8].

Monoglycerides belong to those few nonionic surfactants that have numerous valuable properties. They are non-toxic, do not irritate the skin and mucous membranes, and show surface activity in a broad pH range. These features explain their use in the food, cosmetic, pharmaceutical industry and other national economy sectors as emulsifiers and stabilizers [9, 10].

Polyatomic alcohol esters are also used in the production of synthetic lubricants and applied in small quantities in the production of plasticizers and surfactants of the slag type. Synthetic lubricating oils (SLO) based on polyatomic alcohol esters are used when operating machines and mechanisms in extreme conditions: high or low temperatures, heavy mechanical loads, etc. As for the operational properties, polyatomic alcohol ester-based SLOs have increased thermal stability, increased detergent-dispersing and lubricating properties, lower volatility and viscosity, especially low-temperature, compared with conventional mineral-based lubricants. Despite the higher (3-6 times) cost compared to mineral oils, the use of SLO based on polyatomic alcohol esters provides significant economic benefits by reducing fuel consumption (up to 10%) and exhaust toxicity, reducing oil consumption (2-3 times compared to mineral oil consumption), increasing the life of internal combustion engines and the efficiency of machines and mechanisms [11-14].

There are well-known synthetic methods for the synthesis of esters. The most important of them are esterification, acylation of alcohols and phenols, alkylation of carboxylate anions, alcoholization and acidolysis of esters, transesterification of esters, alcoholization of nitriles, Bayer-Villiger oxidation of aldehydes (formic acid esters) and ketones, alkoxy-carbonylation of the nucleophilic carbon

* To whom all correspondence should be sent:
E-mail: nurasar.82@mail.ru

atom by carbonates and alkoxy carbonylation of the electrophilic carbon atom by oxide carbon and alcohols.

Esters of polyatomic alcohols and carboxylic acids are widely distributed in nature and many of them also have biological activity. All fats and oils of vegetable and animal origin consist almost entirely of glycerol esters (triglycerides). Monoglycerides of C8-C9 acids inhibit the growth of a wide range of bacteria and can be used in the food industry as preservatives since they prevent the formation of moulds [15-19].

There is a known method for producing isovaleric acid monoglyceride by the reaction of hydroalkoxycarbonylation of isobutylene with carbon monoxide and glycerin, but unlike the known method, the Pd(Acac)₂-PPh₃-TsOH system is used as a catalyst in a ratio of 1:7:12, and the process is carried out at a temperature of 100 °C and a pressure of 20 atm for 3 hours [20, 21].

A method for producing isovaleric acid monoglycerides by direct esterification of isovaleric acid with glycerin is known. Isovaleric acid monoglyceride can be also synthesized by the 'isopropylidene' method based on the acylation of α,β -isopropylidene glycerol followed by the removal of the protective isopropylidene group by acid hydrolysis [22].

Research in this direction is of great functional interest because esters of isovaleric acid have several useful properties.

Previously, we synthesized menthylisovalerate and α -bromoethylisovalerate by the reaction of hydroalkoxycarbonylation of isobutylene with menthol and ethanol in the presence of palladium phosphine complexes. These compounds have sedative-antispasmodic properties and are widely used as medicines [23].

It was found that cyclohexyl ether of isovaleric acid has high antibacterial and antifungal activity against pathogens [24].

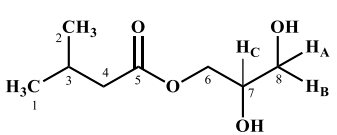
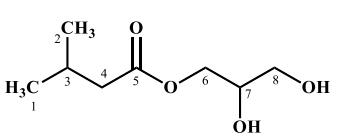
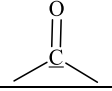
MATERIALS AND METHODS

The IR spectrum was registered on the Shimadzu IR Prestige-21 device (Japan), in the range of 400–4000 cm⁻¹. ¹H and ¹³C NMR spectra were obtained on Bruker DPX 400 (Germany) device, with an operating frequency of 300 MHz. Tetramethylsilane was taken as a reference. The elemental analysis was performed on the CHNS-O elemental analyzer EuroEA3028-HT-OM device (EuroVector S.p.A., Milan, Italy). The physicochemical characteristics are given in Table 1. The IR spectrum of the synthesized isovaleric acid monoglyceride is characterized by typical absorption bands of esters: the carbonyl band at 1735 cm⁻¹ and the 'ether band' (valence vibrations of the C-O-C grouping of the ester bond) at 1188 cm⁻¹. There are absorption bands at 1051 and 1121 cm⁻¹, characteristic of primary and secondary alcohol hydroxyls, and a wide absorption band in the 3403-3466 cm⁻¹ region of associated hydroxyl groups (Table 2).

Table 1. Physicochemical characteristics of isovaleric acid monoglyceride

Compound	T.boiling. °C/mmHg	n _d ²⁰	Molecular formula	Elemental analysis	
				Calculated	Found
Isovaleric acid monoglyceride	187/30	1.4440	C ₈ H ₁₆ O ₄	C – 54.53 H – 9.15	C – 53.60 H – 9.16

Table 2. ¹H and ¹³C NMR of isovaleric acid monoglyceride

Compound	¹ H NMR, δ , ppm (J, Hz)						
	CH ₃	CH	CH ₂ OH	CH ₂ O	CH ₂ OH	CHOH	OH
	0.86 d (6.5)	2.00 d	2.13 d (6.9)	4.02 d (5.4)	3.48 dd (11.8; 6.5) 3.57 dd (11.2; 3.2)	3.82 m	3.6 d 3.66 t
	¹³ C NMR, δ , ppm						
		CH ₂ O	CH ₂ OH	CH ₃	CH	CH ₂ CO	CHO
	173.92	65.21	63.72	22.65	25.92	43.48	70.45

The table shows the ^1H and ^{13}C NMR spectra of the obtained isovaleric acid monoglyceride (Figures 1-2). Protons of the isovaleric acid monoglyceride residue resonate in the strong-field region of the ^1H NMR spectrum. Protons of methyl groups (C^1H_3 and C^2H_3) give a signal of doublets at 0.86 ppm ($J=6.5\text{Hz}$). Methine proton (C^3H) resonates as a multiplet at 2.0 ppm, methylene protons (C^4H_2) manifest as a doublet at 2.13 ppm ($J^3=6.9\text{Hz}$). Protons of the glycerol residue resonate in the weak-field region of ^1H NMR. Methylene protons (C^6H_2) resonate at 4.02 ppm ($J=5.4\text{Hz}$). Methine proton (C^7H) displays as a multiplet at 3.82 ppm. Protons of hydroxyl groups at C^7 and C^8 carbon atoms manifest as an expanded and non-split doublet and triplet at 3.6 and 3.66 ppm. It should be noted that protons on H_A and H_B , due to geminal cleavage among themselves and vicinal cleavage from a neighboring proton (C^7H), have a doublet-doublet multiplet with chemical shifts of 3.48 ppm and 3.57 ppm.

In the ^{13}C NMR spectrum of isovaleric acid monoglyceride, a carbon atom of the carbonyl group $\text{C}^5=\text{O}$ resonates at 173.92 ppm in the form of a peak with weak intensity, which corresponds to a

chemical shift of quaternary carbonyl carbon atoms (Figure 2). The strongest field peak of strong intensity at 22.65 ppm refers to the carbon atoms of the methyl groups C^1 and C^2 of the isovaleric acid. The peaks at 25.92 ppm and 43.48 ppm belong to the carbon atoms C^3 and C^4 . The remaining signals refer to the carbon atoms of the glycerol residue: C^7 – 70.45 ppm, C^6 – 65.21 ppm and C^8 – 63.72 ppm.

The antimicrobial and antifungal activity of isovaleric acid monoglyceride was studied in bacterial strains *Staphylococcus aureus*, *Escherichia coli*, *Pseudomonas aeruginosa* and yeast fungus *Candida albicans* by diffusion into agar (wells). The test sample was dissolved in 96% ethyl alcohol at a concentration of 1 mg/ml.

The cultures were grown at a temperature of 37 °C in 18-24 hours. The grown crops were bred in 0.9% sodium chloride solution; bacteria, 1 ml each were introduced into cups with meat-peptone agar and sown according to the method of obtaining a ‘continuous lawn’. Wells with a diameter of 6 mm were formed, where the drug and 96% ethyl alcohol were introduced as a control.

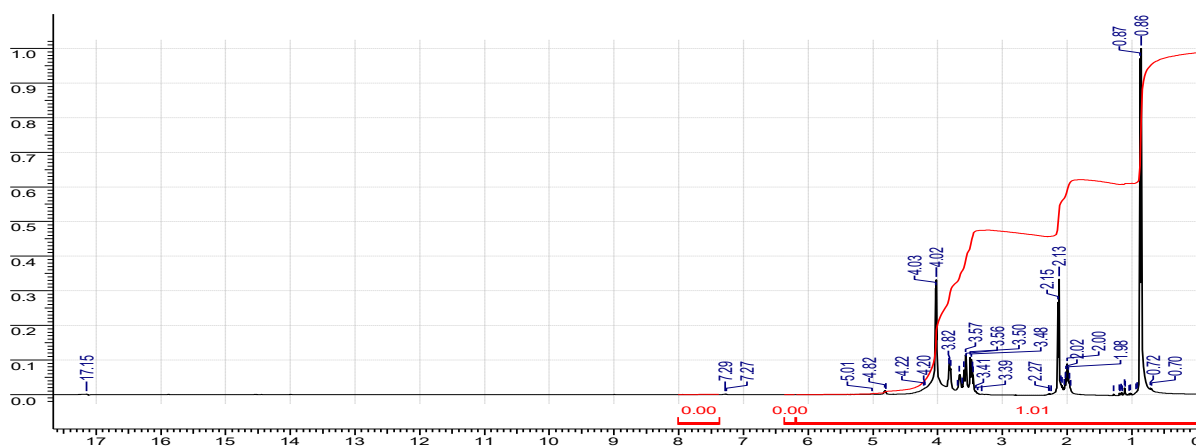


Figure 1. ^1H NMR spectrum of isovaleric acid monoglyceride

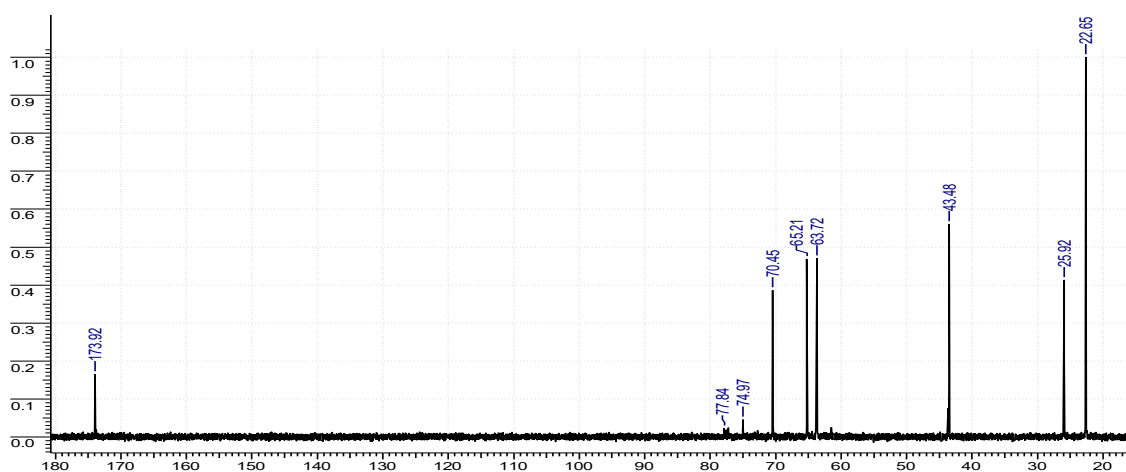
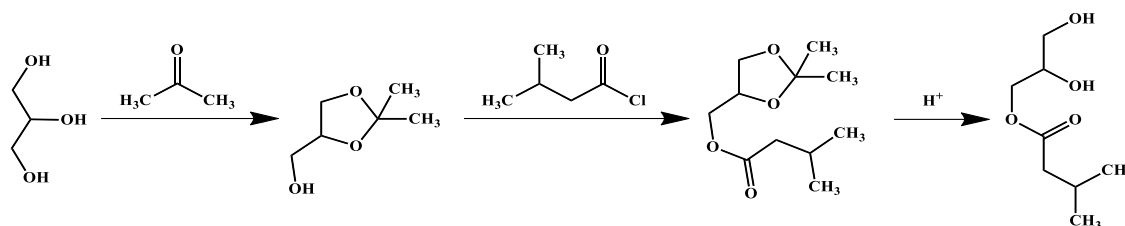


Figure 2. ^{13}C NMR spectrum of isovaleric acid monoglyceride



RESULTS AND DISCUSSION

Isovaleric acid monoglyceride was synthesized by the 'isopropylidene' method with a yield of 94%: 0.1 mol of isovaleryl chloride was added to a stirred mixture of 0.1 mol of α,β -isopropylidene glycerol and 0.12 mol of dry pyridine in chloroform at $-5-0^{\circ}\text{C}$. The reaction mixture was stirred at $-5-0^{\circ}\text{C}$ for 5 h, and then subjected to ultrahigh-frequency irradiation with a frequency of 2450 ± 75 MHz and a power of 100 W for 20 min. The precipitate of pyridine hydrochloride was separated from the chloroform solution, which was further cooled to 0°C and washed with cold water to reach $\text{pH}=7$. The chloroform solution was dried with magnesium sulfate, the solvent was driven away and the left-over was distilled in vacuum at 2 mm Hg. Isovalerate- α,β -isopropylidene glycerol was treated with a 10% aqueous solution of acetic acid under ultrahigh-frequency irradiation with a frequency of 2450 ± 75 MHz and a power of 100 W for 5 minutes until the formed emulsion disappeared. Acetic acid, acetone and water were distilled in vacuum at $40-45^{\circ}\text{C}$. α -Monoglyceride of isovaleric acid was isolated from the residue by column adsorption chromatography on large coarse silica gel (KSK) (0.1-0.16 mm), using chloroform:methanol as an eluent (9:1). The yield of the target product was 94%.

The antimicrobial activity of the sample was estimated by the diameter of the growth retardation zones of the test strain (mm). The diameter of growth retardation zones less than 10 mm was estimated as absence of antimicrobial activity, 10-15 – weak activity, 15-20 – moderate, 20 mm and above – pronounced.

The results of the studies of antimicrobial activity (against *Staphylococcus aureus*, *Escherichia coli*, *Pseudomonas aeruginosa*) and antifungal activity (against *Candida albicans*) are shown in Table 3. As an outcome of the study pronounced antibacterial activity of isovaleric acid

monoglyceride against *Pseudomonas aeruginosa* and moderate antifungal activity against *Candida albicans* was found.

Table 3. Antimicrobial and antifungal activity of isovaleric acid monoglyceride, mm.

<i>Staphylococcus aureus</i>	<i>Escherichia coli</i>	<i>Pseudomonas aeruginosa</i>	<i>Candida albicans</i>
8	11	20±0.1	15±0.1

CONCLUSION

Thus, we synthesized isovaleric acid monoglyceride by the isopropylidene method under microwave irradiation. It was found that the use of microwave irradiation shortens the duration of the process from 20 hours to 20 minutes and increases the yield of the target product from 82% to 94%. Isovaleric acid α -monoglyceride was isolated by column adsorption chromatography on KSK silica gel (0.1-0.16 mm), using chloroform:methanol (9:1) as an eluent. As a result of the studies, it was found that isovaleric acid monoglyceride has pronounced antibacterial activity against *Pseudomonas aeruginosa* and moderate antifungal activity against *Candida albicans*.

Funding: This research has been funded by the Science Committee of the Ministry of Science and Higher Education of the Republic of Kazakhstan (Grant No. AP19677249) and by the Ministry of Agriculture of the Republic of Kazakhstan (BR10764960).

REFERENCES

1. A. El Asbahani, K. Miladi, W. Badri, M. Sala, E.H.A. Addi, H. Casabianca, A. El Mousadik, D. Hartmann, A. Jilale, F.N.R. Renaud, A. Elaissari, *International Journal of Pharmaceutics*, **483** (1-2), 220 (2015).
2. C.R. Manion, R. M. Widder, *American Journal of Health-System Pharmacy*, **74** (9), (2017).
3. H.A.E. Shaaban, A. H. El-Ghorab, T. Shibamoto, *Journal of Essential Oil Research*, **24** (2), 203. (2012).
4. T.B. Adams, M.M. McGowen, M.C. Williams, S.M. Cohen, V.J. Feron, J. I. Goodman, L.J. Marnett, I.C. Munro, P.S. Portoghese, W.J. Waddell, *Food and Chemical Toxicology*, **45** (2), 171 (2007).
5. M. Younes, G. Aquilina, L. Castle, K.H. Engel, P.

- Fowler, M. Frutos, P. Furst, U. Gundert-Remy, R. Gurtler, T. Husoy, P. Moldeus, A. Oskarsson, R. Shah, I. Waalkens-Berendsen, D. Wolfle, R. Benigni, C. Bolognesi, K. Chipman, E. Cordelli, G. Degen, D. Marzin, C. Svendsen, G. Vianello, W. Mennes, *Efsa Journal*, **18**(3), 6029 (2020).
6. S. Molino, N. A. Casanova, J. A. R. Henares, M. E. F. Miyakawa, *Journal of Agricultural and Food Chemistry*, **68**(10), 2836 (2020).
 7. T. Okuda, *Nippon Nogekagaku Kaishi-Journal of the Japan Society for Bioscience, Biotechnology and Agrochemistry*, **69** (9), 1202 (1995).
 8. A. N. Pell, T. K. Woolston, K. E. Nelson, P. Schofield, *Aciaar Proceedings Series [Tannins in livestock and human nutrition, proceedings]. International Workshop on Tannins in Livestock and Human Nutrition, Adelaide, Australia (1999)*.
 9. R. K. Saxena, J. Isar, S. Saran, R. Kaushik, W. S. Davidson, *Current Science*, **89** (6), 1000 (2005).
 10. C. H. Benton, *Candy Ind.*, **118** (8), 21 (1962).
 11. J. Antonio Cecilia, D. Ballesteros Plata, R. M. Alves Saboya, F. M. Tavares de Luna, C. L. Cavalcante Jr., E. Rodriguez-Castellon, *Processes*, **8** (3), Article 257 (2020).
 12. C. H. Chan, S. W. Tang, N. K. Mohd, W. H. Lim, S. K. Yeong, Z. Idris, *Renewable & Sustainable Energy Reviews*, **93**, 145 (2018).
 13. A. M. Danilov, S. A. Antonov, R. V. Bartko, P. A. Nikulshin, *Petroleum Chemistry*, **61**(7), 697 (2021).
 14. P. Pranav, E. Sneha, S. Rani, *Industrial Lubrication and Tribology*, **73** (9), 115 (2021).
 15. Y. Andriana, T. D. Xuan, T. N. Quy, T. N. Minh, T. M. Van, T. D. Viet, *Foods*, **8**(1), Article 21 (2019).
 16. M. Mariani, F. Zaccheria, N. Scotti, R. Psaro, N. Ravasio, *Chemistry Select.*, **1** (12), 2999 (2016).
 17. M. Popova, S. Silici, O. Kaftanoglu, V. Bankova, *Phytomedicine*, **12** (3), 221 (2005).
 18. O. Taglialatela-Scafati, F. Pollastro, G. Chianese, A. Minassi, S. Gibbons, W. Arunotayanun, B. Mabebie, M. Ballero, G. Appendino, *Journal of Natural Products*, **76** (3), 346 (2013).
 19. L. Zino, A. Alsharaa, S. Al-Dossary, A. Alwadey, B. Chanbasha, *International Journal of Pharmaceutical Sciences and Research*, **7** (4), 1710 (2016).
 20. H. A. Suerbaev, E. G. Chepajkin, B. Z. Dzhiembaev, N. O. Appazov, G. M. Abyzbekova, *Petroleum Chemistry*, **47** (5), 345 (2007).
 21. K. A. Suerbaev, E. G. Chepaikin, N. O. Appazov, B. Z. Dzhiembaev. *Petroleum Chemistry*, **52**(3), 189 (2012).
 22. N. O. Appazov, G. M. Abyzbekova, A. F. Artamonov, B. Zh. Dzhiembaev, Kh. A. Suerbaev, *Khimicheskii Zhurnal Kazakhstana*, **2**, 13 (2007). (in Russian).
 23. Kh. A. Suerbaev, G. Zh. Zhaksylykova, N. O. Appazov, *Eurasian Chemico-Technological Journal*, **16**(4), 299 (2014).
 24. N. O. Appazov, S. S. Seitzhanov, A. T. Zhunissov, R. A. Narmanova, *Russian Journal of Organic Chemistry*, **53** (10), 1596 (2017).

Application of mobile fluorescence spectroscopy as a method for the analysis of representatives of different varieties of carrots (*Daucus carota*) during storage under uncontrolled conditions

V. Slavova

Department of Plant Breeding, Maritsa Vegetable Crops Research Institute, Agricultural Academy, 32, Brezovsko Chaussee, Plovdiv 4003, Bulgaria

Received: October 26, 2023; Revised: January 10, 2024

The present study aims to establish the application of mobile fluorescence spectroscopy as a method to determine varietal differences and water content during storage of carrots under uncontrolled conditions. The experimental studies were carried out on the farm where the carrots were grown and stored. Fluorescence analysis was performed with a source with an emission wavelength of 285 nm, using an author-developed mobile set up in a fiber-optic configuration generating fluorescence signals. Root crops from Nantes, Short'n Sweet, Touchon and Flakkee varieties were the subject of this study. They were measured after harvesting after 3 and 6 months of storage. The correlation between the emission wavelengths of the samples of different varieties, as well as those of the same variety at different storage intervals, was established. This fact allows mobile fluorescence spectroscopy to be successfully applied as a rapid tool in carrot breeding programs in establishing the origin of unknown root crops in the presence of a rich library of spectra, as well as in the sorting of carrots in warehouses of food chains and producers. The results of the experiment can be used to optimize the time for the analysis of varietal affiliation of different carrot genotypes during storage under uncontrolled conditions. Fluorescence spectroscopy in a fiber-optic configuration will support the process of determining the affiliation of a particular carrot variety to a given variety (even for samples of unknown origin when it is necessary to qualify and sort in a short time).

Keywords: carrot accessions, fluorescence spectroscopy, variety, emission wavelength, storage under uncontrolled conditions

INTRODUCTION

The carrot (*Daucus carota*) is a biennial, rarely annual or perennial herbaceous plant of the umbel family. It is grown mainly in the Mediterranean, but also in America, Africa, Australia, etc. [1]. The cultivated carrot is a biennial vegetable and fodder plant. It is grown for its root, which is fleshy and, depending on the variety, has a rounded, truncated-conical, spindle-shaped or other shape with a red, yellow-red, yellow or white color [2]. It forms a pale yellow to red-orange root crop in the first year. It forms seeds and flowers in the second year. It is used for food, fodder and as a medicinal agent [3].

The carrot contains an average of 88.8% water [4]. Carrots are a strong-tasting, useful, long-lasting and storable vegetable. It has been shown that during the first five months of storage after peeling, its vitamin A content increases, and if protected from heat or direct sunlight, it can preserve its nutrients for another two to three months [5].

A non-destructive method was developed for the determination of carotene content in carrots using Raman spectroscopy combined with chemometry.

Raman spectra of carotene and carrots were collected to determine the Raman peaks of carotene in the Raman spectrum of carrot. According to the Raman peaks of carotene, the distribution of carotene content in carrots is discussed. The average Raman spectra of different parts of carrots were used to represent the carrot sample. The results of the study provide methodological support for the quantitative analysis of carotene content in carrots [6].

Various analytical techniques have been used to investigate the complex composition of carrots. Among them, fluorescence spectroscopy cannot be neglected in the development of rapid and non-invasive analytical methodologies. It is one of the most sensitive spectroscopic approaches used in the identification, classification, authentication, quantification and optimization of various parameters during food processing and storage. It uses various chemometric tools. Chemometrics helps extract useful information from spectral data used in the characterization of food samples. The potential of fluorescence spectroscopy in the analysis of various foods, such as dairy products, meat, fish, eggs, edible oil, cereals, fruits,

* To whom all correspondence should be sent:
E-mail: vania_plachkova@abv.bg

vegetables, etc., has been demonstrated by qualitative and quantitative analysis with different chemometric approaches [7]. The potential application of front face fluorescence (FFF) to monitor the impact of the industrial process on carrot baby food was evaluated. The effect of using different raw materials, fresh carrots, frozen cubes or pasteurized puree, on the NFC content of the resulting sterilized puree was also tested. FFF is a hopeful tool for monitoring the fast and easy processing of vegetables in a quality control approach [8].

The optical, morphological, structural and compositional properties of water-soluble and blue-emitting carbon quantum dots (CQDs) have been confirmed by various characterization methods. As a fluorescent probe, CQDs showed a good linear response to picric acid (PA) with a limit of detection (LOD) of 18 nM. The sensing mechanism involves a combination of static cooling and fluorescence resonance energy transfer. Fresh carrots were used as a model sample [9].

Through the application of fluorescence spectroscopy, the binding mechanisms of purple corn, grape and black carrot anthocyanin extracts have been successfully investigated. A laser with a wavelength of 280 nm at 25 °C, 35 °C and 45 °C was used as the emission source. The fluorescence intensity decreased (up to 73%) and its λ_{\max} increased (by ~5 nm) with increasing anthocyanin concentration (0–100 μ M). This technique was applied to evaluate the color stability of anthocyanins, expanding the application of anthocyanins as food colorants that better withstand processing and storage [10].

In connection with the demands of consumers for high food quality, the conducted research can serve as a basis for the creation of mobile detecting devices, with which to carry out instant analysis of warehouse production of carrots stored in uncontrolled conditions, both in processing plants and in food retail outlets.

The present study aims to establish the function of fluorescence spectroscopy as a mobile method for the analysis of representatives of different varieties of carrots (*Daucus carota*) during storage under uncontrolled conditions. They will be compared in terms of determining the spectral distribution after harvesting and at different storage periods of 3 and 6 months. The accessions were stored under uncontrolled storage conditions.

This will permit the technique to be applied non-invasively in the quality control of carrot production in unspecified storage and outdoors.

MATERIALS AND METHODS

Materials

Accessions from four standard carrot varieties were investigated.

Nantes - An early (non-hybrid) variety suitable for both greenhouse and field production. They are used for fresh consumption, for processing, for pickles, winter salads, many dishes and natural juices. Their shape is cylindrical and smooth. The average length of Nantes carrots is about 15-16 cm. The root crops are extremely sweet, orange-red, crunchy and aromatic - with very good tasty qualities.

Short`n Sweet - Suitable for growing in soil conditions that are not ideal, such as heavy or poor soil that is rich in clay or difficult to work. This rich, sweet little root is easy to grow and full of vitamins. 'Short `n Sweet' is a 'Chanetay' type that produces compact 4-inch roots with about 68 days to harvest.

Touchon - The variety is suitable for different types of soil, which is why it is grown both in the southern and northern regions. According to the description, if the crops are properly cared for, Touchon carrots bear fruit until the end of July, but the main harvest occurs in early autumn (early September). To be harvested in early June, sowing is done in mid-autumn (October-November).

Flakkee - An early variety. It forms a smooth, deep orange-red, cone-shaped root with a blunt tip, 20 cm long and weighing 200 - 250 g. High tolerance to diseases and high temperatures. An extremely suitable variety for early production. Vegetation period - about 105 days after sowing. The roots are cone-shaped, bright orange, sweet, 18-24 cm long. They do not tend to crack. Suitable for autumn harvest and winter storage. It grows best in cultivated, humus, unirrigated light clay or sandy soil. If the soil is heavy, germination is poor, root crops are short, branched and split.

Carrots are harvested in dry sunny weather in the morning. After they are washed, they are spread out on a linen cloth and left to dry well, being turned periodically. The carrots are dried for 2-3 hours in the sun and then for 7-10 days in a well-ventilated place. Their tops are cut in two stages. The first stage is to cut off just above the root crop, the second stage is to cut off the top of the carrot by 1 cm. Immediately before storage, the carrots are sorted and only healthy and undamaged root vegetables are set aside for long-term storage. They are stored in a dry warehouse at an average temperature of 4-7 °C.

Fluorescence spectroscopy

The mobile fiber-optical spectral installation for the study of fluorescence signals is designed specifically for the rapid analysis of plant biological samples. The mobile experimental setup used by fluorescence spectroscopy includes the following components:

- Laser diode (LED) with an emission radiation of 245 nm with a supply voltage in the range of 3 V. It is housed in a hermetically sealed TO39 metal housing. The emitter has a voltage drop of 1.9 to 2.4 V and a current consumption of 0.02 A. The minimum value of their reverse voltage is – 6 V.

- Rod lens of the achromatic doublet type. It is composed of two bonded lenses with different Schott and Corning dispersion coefficients with an anti-reflective coating. The radii of the two lenses are selected so that the chromatic aberration of one lens compensates that of the other. The tolerance of the diameter of the forming optics is -0.005 mm.

- The multimode optical fiber is FG200LEA. It has a core diameter of 200 μm and a step index of refraction.

- Quartz glass area of 4 cm². Its optical properties are to be transparent to visible light and to ultraviolet and infrared rays. This allows it to be free of inhomogeneities that scatter light. Its optical and thermal properties exceed those of other types of glass due to its purity. Light absorption in quartz glasses is weak.

- CMOS detector with photosensitive area of 1.9968×1.9968 mm. Its sensitivity ranges from 200 nm to 1100 nm. Its resolution is $\delta\lambda = 5$. The profile of the detector sensor projections along the X and Y axes is also designed for very small amounts of data, unlike widely used sensors.

The sample is irradiated by the LED, after which it fluoresces. The emission signal is registered at 45°C by the rod lens which transmits it through the optical fiber to the detector.

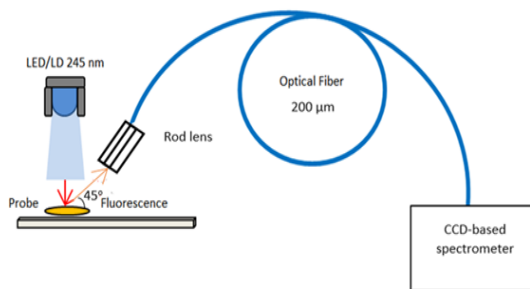


Fig. 1. Mobile experimental installation used by fluorescence spectroscopy

The three unique advantages of this scheme are:

- Inclusion of the HQ lenses in the construction of the system due to their increased light transmission efficiency by almost completely filling the air gaps between the individual lenses.
- Unique design of optical fiber coupling from a headquarters lens in a duralumin housing. In this way, the optimal design for compiling with optical fibers and forming images from laser diodes with low levels of intense losses is achieved.
- Registering of the emission signal at 45°C.

RESULTS AND DISCUSSION

Prolonged storage under controlled conditions of carrot root crops leads to a decrease in their water content. This process is directly proportional to the duration of storage.

The optical properties of the carrot are determined by its energy structure, which includes both the occupied and free electronic energy levels, as well as the energy levels of the atomic vibrations of the molecules or the crystal lattice.

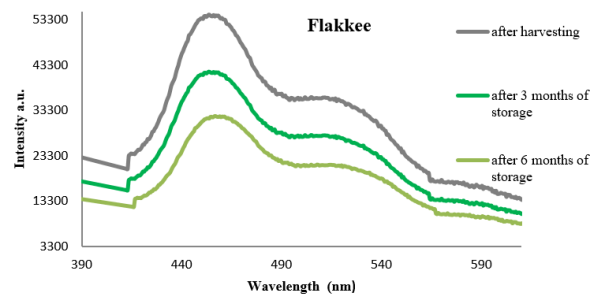


Fig. 2. Difference in emission wavelengths of Flakkee variety accessions of carrots after harvesting and storage for 3 and 6 months.

The possible transitions between these energy levels, as a function of photon energy, are specific to the carrot, resulting in spectra and optical properties unique to it. Carrots contain particles smaller than the wavelength of visible light. Particles in the turbid medium, such as the carrot, act as independent light sources, emitting incoherently, causing the samples to visibly fluoresce.

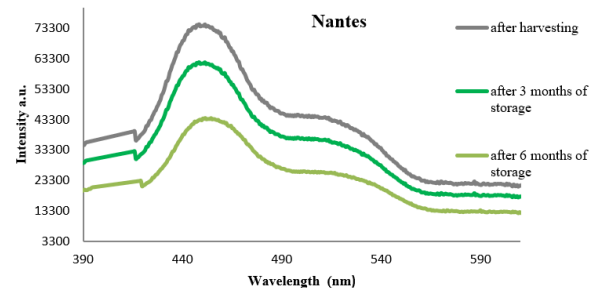


Fig. 3. Difference in emission wavelengths of Nantes variety accessions of carrots after harvesting and storage for 3 and 6 months.

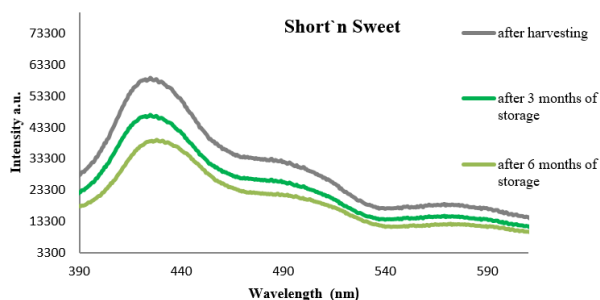


Fig. 4. Difference in emission wavelengths of Short'n Sweet variety accessions of carrots after harvesting and storage for 3 and 6 months.

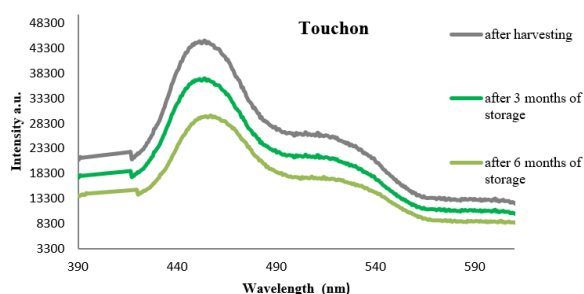


Fig. 5. Difference in emission wavelengths of Touchon variety accessions of carrots after harvesting and storage for 3 and 6 months.

Therefore, fluorescence spectroscopy finds application for analysis of this vegetable crop. The optical parameters and spectral properties also change as a function of temperature, pressure, external electric and magnetic fields, etc., which allows obtaining essential information about changes in the chemical and cellular morphological composition of the carrot.

The analysis of the graphs established the application of fluorescence spectroscopy for the analysis of root crops during storage in a warehouse under uncontrolled conditions for a period of 3 and 6 months (Figures 2, 3, 4 and 5). The decrease in signal intensity is directly proportional to the duration of storage (and it, in turn, is related with a decrease in root water content due to evaporation).

A literature survey was performed to conduct similar research. It turned out that until now the described experimental approach for the analysis of root crops has not been applied nationally and internationally. This gives us reason to claim that mobile fluorescence spectroscopy in a fiber optic configuration has been applied for the first time to analyze carrot samples for their water content and root stability during storage in a storage room under uncontrolled conditions. The three main advantages of fluorescence spectroscopy are that the method is fast, does not require consumables, and can be performed on-site in the warehouse. The decision for local measurements was made to avoid damage to

the samples during transport and thus, to ensure fluorescence analysis with high sensitivity. The signal intensity is high enough at very low water content, which means that the method is applicable to controlling the quality of root crops during long-term storage of carrots in storage rooms under uncontrolled conditions. An essential point in fluorescence diagnostics regarding the comparison of accessions after harvesting and after a certain period of storage is that the method is highly sensitive in terms of determining the water content of root crops kept in a storage room under uncontrolled conditions. This fact allows fluorescence spectroscopy to be applied as a non-invasive method in quality analysis of carrot production kept in storage rooms of farms and commercial establishments.

CONCLUSIONS

- The method of mobile fluorescence spectroscopy is fast-acting in determining the water content of carrots during storage of the product.
- The method of mobile fluorescence spectroscopy is applicable in controlling the germination quality of root crops during storage.
- It was proven that mobile fluorescence spectroscopy will support the selection process and the control of stock production of carrots when it is necessary to qualify a large set of samples in a short time.
- A systematic engineering approach for the alignment (optical tuning) of a dedicated mobile fluorescence spectroscopy applied research facility was found to be applicable in the characterization of produced carrot during storage.

Acknowledgement: I express my gratitude to Mrs. Minka Serinska, in whose farm the carrots were grown and stored, as well as to the entire team of the farm. Without their help, the research would not have been carried out.

REFERENCES

1. J. Stolarczyk, J. Janick, *Chronica Horticulture*, **51**(2), 899 (2011).
2. P. Simon, in: J. Janick (ed.), Carrot (*Daucus carota* L.) Breeding, *Advances in Plant Breeding Strategies*, **19**, 213 (2010). DOI: <https://doi.org/10.1094/PHYTO-02-15-0032-FI>
3. P. W. Simon, I. L. Goldman, in: R. J. Singh (ed.), Genetic Resources, Chromosome Engineering, and Crop Improvement Series, CRC Press, Boca Raton, 2007, vol. 3, p. 497.
4. K. D. Sharma, S. Karki, N. S. Thakur, *J. Food Sci. Technol.*, **49**, 22 (2012), DOI: <https://doi.org/10.1007/s13197-011-0310-7>.
5. S. Terhi, *Scientia Horticulturae*, **85**(1-2), 1 (2000),

V. Slavova: *Application of mobile fluorescence spectroscopy for the analysis of varieties of carrots during storage ...*

DOI: [https://doi.org/10.1016/S0304-4238\(99\)00133-8](https://doi.org/10.1016/S0304-4238(99)00133-8).

6. X. Wang, X. Zhang, H. Hong, Ch. Guan, Ch. Zhao, *European Food Research and Technology*, **247**, 2299 (2021),

DOI: <https://doi.org/10.1007/s00217-021-03788-w>.

7. M. Ahmad, A. Sahar, B. Hitzmann, Fluorescence Spectroscopy for the Monitoring of Food Processes, in: B. Hitzmann (ed.), *Measurement, Modeling and Automation in Advanced Food Processing. Advances in Biomedical Engineering/Biotechnology*, 2017, vol. 161, p. 121,

DOI: https://doi.org/10.1007/10_2017_11

8. A. Acharid, L. Rizkallah, L. Ait-Ameur, B. Neugnot, K. Seidel, M. Särkkä-Tirkkonen, J. Kahl, I. Birlouez-Aragon, *Food Science and Technology*, **49**(2), 305 (2012),

DOI: <https://doi.org/10.1016/j.lwt.2012.06.016>.

9. B. John, Ch. Thara, B. Korah, N. John, B. Mathew, *Journal of Industrial and Engineering Chemistry*, **126** (25), 546 (2023),

DOI: <https://doi.org/10.1016/j.jiec.2023.06.043>.

10. S. Ren, M. Giusti, *Foods* **10**(2), 310 (2021),

DOI: <https://doi.org/10.3390/foods10020310>.

Selected papers presented on the Seventh International Scientific Conference Alternative Energy Sources, Materials and Technologies - AESMT'24, 14 - 15 May, 2024, Sofia, Bulgaria

Increasing the energy efficiency of combustion processes using contact economizer systems and finned tube heat exchanger

D. N. Kolev

Institute of Chemical Engineering, Bulgarian Academy of Sciences, Acad. G. Bonchev Str., Bl. 103, 1113, Sofia, Bulgaria

Received: April, 15, 2023; Accepted: February 19, 2024

The increasing greenhouse gas pollution of the environment and the rising costs of energy resources lead to a search for different methods of waste heat utilization. This paper provides a comparison between two efficient methods for waste heat recovery from flue gases. A system with contact economizer CE and finned tube heat exchangers R is proposed. The comparison between them shows that the CE gives significantly better results both in thermal and economic aspects. For small boiler capacities up to 1-1.5 MW it is advisable to use heat exchangers with finned tubes due to their easier operation.

Keywords: heat exchangers, energy efficiency, CO₂ reduction, contact economizer

INTRODUCTION

Increasing energy efficiency is one of the main objectives of the European Union. Achieving this objective will also achieve the accompanying objectives of reducing greenhouse gas emissions and reducing the use of fossil fuels.

The targets set by DIRECTIVE 2012/27/EU OF THE EUROPEAN PARLIAMENT of 25 October 2012 is to achieve a 20% increase in energy efficiency for 2020 and 32.5% for 2030.

In order to meet these objectives, it is necessary to analyse and propose solutions for a more complete use of fossil fuels [1, 2]. This paper aims to compare existing methods of heat utilization of combustion plants such as finned tube systems [3], and contact economiser systems [4] as well as to provide a solution for the ranges in which they are most efficient.

To be able to compare different heat exchangers we first need to know their characteristics, as well as the characteristics of the flue gases they will work with.

The characteristics of the flue gases produced by the combustion of methane at different excess air coefficients are shown further down in the article.

FLUE GASES HEAT CONTENT

When evaluating heat exchanger apparatuses, it is necessary to know the mean temperature difference. The latter is determined from the change of gas heat contents as a function of the temperature. Because of water vapor condensation, the change of gas heat contents at a given temperature difference is approximately proportional to this difference only

for temperatures higher than the condensation temperature. The latter depends on the coefficient of air excess λ at which the fuel is burned. Fig. 1 represents the temperature dependence of the heat contents of flue gases obtained from burning of 1 kmol natural gas at various values of air excess λ .

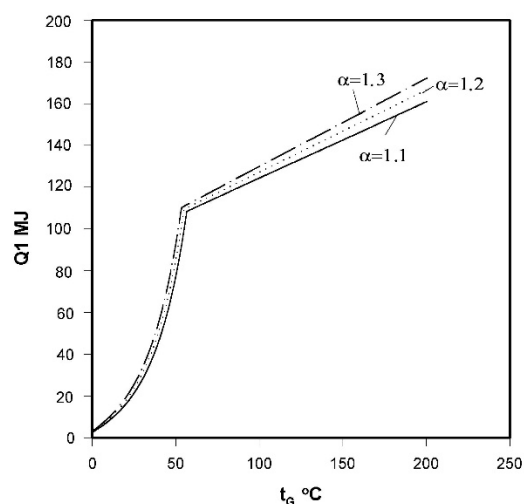


Fig. 1. The heat content of the flue gases, Q obtained from burning of 1 kmol natural gas, as a function of temperature at different values of the coefficient of air excess λ .

Flue gas components are assumed to have ideal gas properties. The temperature dependence of the specific heat at constant pressure C_p is evaluated by the relation:

$$C_{p_i} = A_i + B_i T + C_i T^2 + D_i T^3, \quad (1)$$

where i refers to the corresponding component; A , B , C , and D are experimental constants for each

* To whom all correspondence should be sent:
E-mail: d.kolev@iche.bas.bg

component, given in [5]; T is flue gas temperature in K.

The enthalpy of an ideal gas mixture of components is expressed as:

$$h_i = A_i(T - 273.16) + B_i(T^2 - 273.16^2)/2 + C_i(T^3 - 273.16^3)/3 + D_i(T^4 - 273.16^4)/4 \quad (2)$$

Eq. (2) is obtained by multiplication of Eq. (1) by dT and its integration in the limits from 273.16 to T.

The results of Eq. (2) for non-condensing components using the constants from [5] were compared with existing data [6]. The error was less than 0.1 %.

Water vapor enthalpy was calculated by Eq. (2) adding also water evaporation heat at 0°C equal to 2500 kJ/kg [6] or 45 000 kJ/kg mol.

Comparing with results from [7] it was found that for the existing conditions an assumption for water vapor as an ideal gas introduces an error not higher than 0.15 %.

The equilibrium partial pressure P, expressed as mm Hg column, necessary for determination of water vapor concentration, was calculated by the relation:

$$\lg P = -2892.369/T + 19.301142 - 2.892734 \cdot \lg T - 4.9369728 \times 10^{-3} \cdot T + 0.5606905 \times 10^{-6} T^2 - 4.646 \times 10^{-2} T^3 + 3.787 \times 10^{-12} \cdot T^4 \quad (3)$$

Specialized computer software was developed for determination of the mean temperature difference at given initial and final temperature of the flows.

BRIEF CHARACTERISTICS OF FINNED TUBE HEAT EXCHANGERS

Finned tube heat exchangers can be made in various ways. The most efficient and cheapest are steel pipes with aluminium ribs. They are produced by cold forming of aluminium pipe mounted axially over the steel pipe. Fig. 2 shows a cross-section of the pipe. Substantial advantages of these apparatuses are their high heat transfer ability and low price of about \$20 per square meter of heat transfer surface as of writing of this paper.

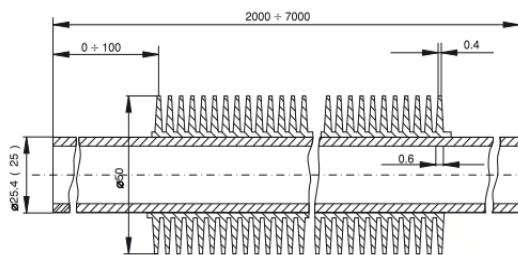


Fig. 2. Cross-section of the finned pipe [8].

An essential shortcoming is the corrosion of aluminium in condensation regime, which does not allow the use of these heat exchangers below the condensation point of the heat-transfer wall. Aluminium doped with magnesium and manganese becomes corrosion resistant to these conditions but is not good for production of ribs over the steel tubes because of its reduced plasticity.

Comparison of various apparatuses should be done at their optimal operating conditions, i.e. at optimal gas velocity. For finned tube heat exchangers, the optimal velocity is that demanding minimum expenses to obtain a desired effect. The expenses are capital and operational. It can be easily calculated that the yearly payment for a 10-year loan will be 20 % of the apparatus price assuming 10 years depreciation period and 15 % interest per year.

The main operational costs are for electricity. The exploitation period is presumed to be 6000 hours per year. The longer this period is, the greater the energy expenses will be. Consequently, the optimal velocity will be lower. On the contrary, the optimal velocity will be higher for a shorter period.

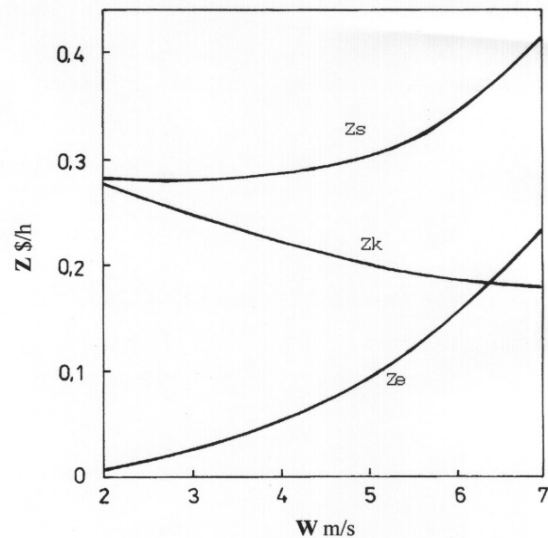


Fig. 3. Dependence of expenses for one-hour operation of an installation with finned tube with aluminium ribs for utilization of 1000 kW waste heat, as a function of gas velocity. Zs-sum of the expenses; Zk – expenses for investments; Ze – expenses for energy consumption.

Fig. 3 shows the expenses for one-hour operation of an installation with a finned tube at various gas flow velocities. Manufacturer's information [8] for heat transfer coefficients and pressure drop under various gas velocities is used to plot the curves. The data is determined under the following additional conditions: initial temperature of heated water 20 °C; final temperature of heated water 55 °C; initial

temperature of flue gases 180 °C; final temperature of flue gases 70 °C; average temperature 81.85 °C; estimated at counter-current operation; van efficiency - 60 %; price of electricity – 0.04 \$/kWh. The expenses for water feeding are neglected. It is seen that the optimal flow velocity in the free cross-section of the apparatus is 2 - 4 m/s. Since the minimum is not very pronounced, we take the value 4 m/s that corresponds to a smaller apparatus. For this velocity, Fig. 4 supplies the following data: heat transfer coefficient - 24 W/(m²°C); pressure drop - 55 Pa, concerning 2 rows of the finned tube. The mean temperature difference does not essentially affect the optimal velocity. When it increases, the heat exchanger surface is proportionally changed. Consequently, the capital 55 Pa, concerning 2 rows of finned tube costs and pressure drop are also proportionally changed.

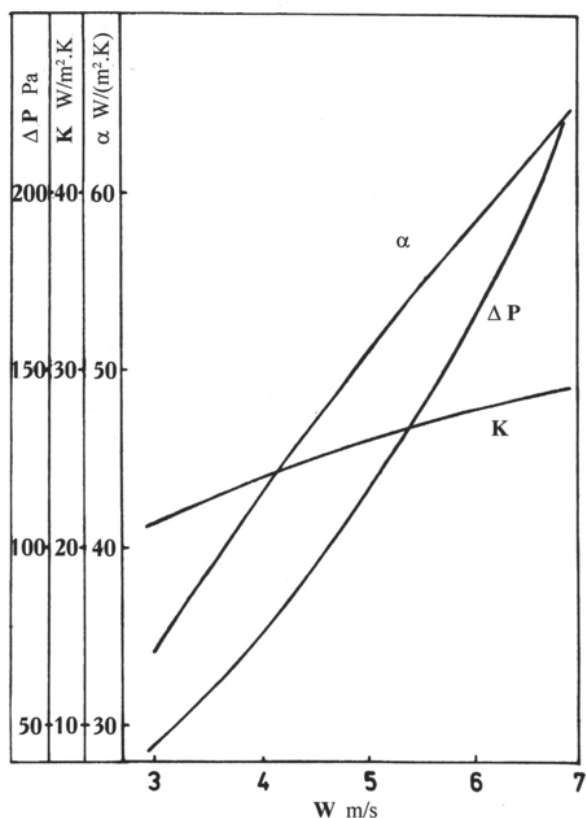


Fig. 4. Dependence of the pressure drop ΔP , K , α as functions of the real air velocity in a heat exchanger with two rows of ribbed pipes arranged in a chess-board order, after data of Klimatech [8].

BRIEF CHARACTERISTICS OF A CONTACT ECONOMIZER

The main quantity of heat in the flue gases, especially when burning natural gas, is the condensation heat of water vapor. The stoichiometric amount of the vapor is 2.25 kg for each kilogram of burned methane. The condensation

temperature depends on the apparatus pressure and air excess in the boiler. Normally, it is about 55.5 – 57.5 °C. The contact economizers systems are created mainly to utilize the condensation heat. Contact economizers utilize heat that can be used mainly for warming of relatively cold flows, such as technical water for feeding of boilers or central heating systems. The maximal temperature of heating is that of the wet thermometer in the flue gases leaving the boiler (about 60 °C). Profitable heating of water is possible at temperatures of about 4 - 5 °C lower than that.

A contact economizer system is presented on Fig. 5. The contact economizer system consists of 1 boiler, contact economizer 2, circulating pump 3 and plate heat exchanger 4. Flue gases are scrubbed with circulating water in the packing of the contact economizer 2. As a result, the water is heated and then transported by the pump 3 to the heat-exchanger 4 where it heats a pure water flow. Afterwards the recirculating water is returned to the liquid distributor 5 of the contact economizer 2. The condensed water vapor in the apparatus 2 is evacuated through a hydro-locking device 7. A part of the flue gases can bypass the contact economizer through valve 6.

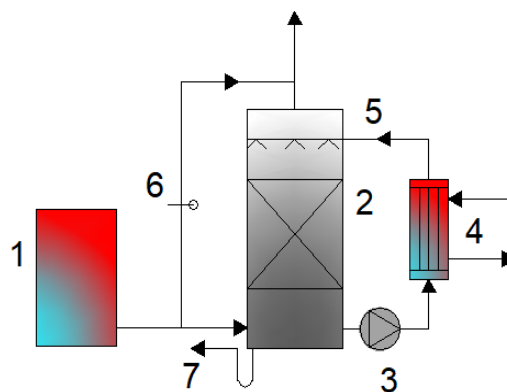


Fig. 5. Technological scheme of a contact economizer system CE [9, 10].

At initial temperature of the flue gases 120 - 130 °C, the maximal quantity of utilized heat is up to 13 % of the heat produced in the boiler. At 190 - 200 °C flue gases temperature, the amount of utilized heat is up to 16 %.

The main advantage of a contact economizer system is the extremely high heat transfer coefficient of its plate heat exchanger. It is more than 100 times higher than that of finned tube. Main shortcoming of these systems is the sharp driving force reduction due to adiabatic gas cooling during the initial contact with the circulating water flow.

COMPARISON OF FINNED TUBE HEAT EXCHANGERS AND CONTACT ECONOMIZERS

Finned tube heat exchangers have the essential advantage of being able to heat circulating water flow for central heating purposes, while contact economizers are not applicable for this case. In order to be precise, the comparison between them is made considering the case where both systems can be used - heating of feeding water flow for boilers and for central heating networks. Each of them is able to reduce flue gas temperature to the same value, so capital costs and energy consumption can be compared for equal quantity of utilized heat.

For evaluation of the capital costs, it is convenient to compare apparatus price divided by the quantity of heat utilized for unit of time and unit of temperature difference. It should also be accounted that in the contact economizer about 1°C is lost.

From equation:

$$Q = K.F. \Delta t_m \quad (4)$$

it follows:

$$F = Q/(K. \Delta t_m), \quad (5)$$

where:

Q [W] is the heat quantity transferred through the heat exchange surface for a unit of time;

F - heat transfer surface;

K [W/(m²·°C)] is heat transfer coefficient;

Δt_m [°C] is mean temperature difference.

The price Z of an installation for production of 1 kW heat power is:

For finned tube heat exchangers:

$$Z_R = F_R.Z_{1R} = Z_{1R}/(0.001. K_R. \Delta t_{mR}), \quad (6)$$

where:

$$K_R=24 \text{ [W/m}^2\text{.K]};$$

$$Z_{1R}=20 \text{ [$/m}^2\text{]}.$$

Subscript "1" refers to 1 m²; subscript "R" refers to finned tube.

For contact economizer systems "CE":

$$Z_{CE} = F_{CE}. Z_{1CE} = Z_{1CE}/[0.001.K_{CE}.(\Delta t_{mCE} - 1)], \quad (7)$$

where:

$$K_{CE}=4650 \text{ [W/m}^2\text{.K]};$$

$$Z_{1CE}=247 \text{ [$/m}^2\text{]}.$$

In both cases the price of 1 m² heat exchanger surface also includes the price of the accompanying equipment needed for operation.

The coefficient 0.001 is for conversion of values of Q from W to kW.

In the case of a plate heat exchanger, the temperature difference is reduced with 1 °C consumed in the contact economizer.

Price calculations for the finned tube heat exchanger are done assuming it to be made of carbon steel.

If the temperature difference of the plate heat exchanger is 3 °C (i.e., Δt_m = 4°C), Z_{CE} is equal to 17.6 [\$/kW].

For the same Δt_m the price of finned tube heat exchangers made of carbon steel with aluminium ribs is Z_R = 208.3 [\$/kW], which is 12.15 times more than that of the contact economizer system. Consequently, in order to have the same capital costs per unit of utilized heat, a finned tube heat exchanger has to work at a mean temperature difference equal to 12.15 × 4 = 48.6 °C when made of carbon steel pipes with aluminium ribs. It means that it is expedient to use the first type finned tube for cooling flue gases to temperatures of about 49 °C higher than the cooling water temperature. Further cooling should be done in a contact economizer system.

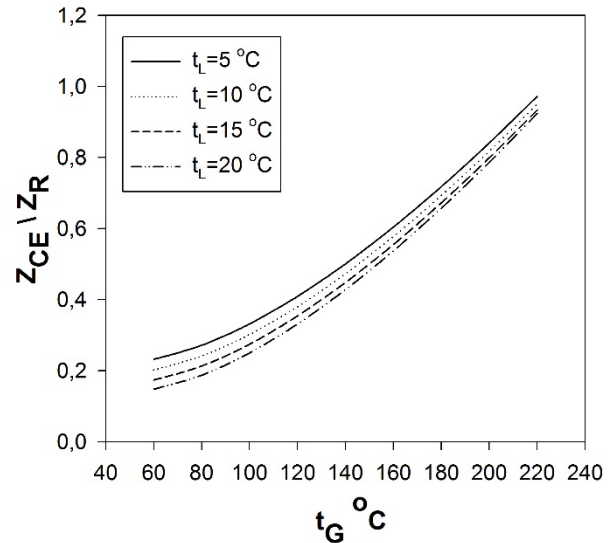


Fig. 6. Dependence of the ratio of the investments Z for constructing CE to the investments for finned tube heat exchangers R at equal quantities of heat utilized from the two systems, as a function of the input temperature of the flue gases, at different values of the input temperature of the water being heated λ=1.1. The temperature of the heated water is 55 °C.

Fig. 6 represents the ratio of capital costs for CE and finned tube heat exchangers utilizing an equal quantity of heat in relation to the gas temperature. Curves for various values of the initial temperature of heated water t_L are shown. The coefficient of air excess is kept constant and equal to λ = 1.1. The mean temperature difference for plate heat exchangers is 3 °C. For finned tube heat exchangers its value is obtained assuming conditions of full counter-current flow, which means that the value Z_{CE}/Z_R is slightly overestimated. The additional

conditions used in the calculation of the curves on Figs. 6&7, are stated in the figure captions.

As it was mentioned, finned tube heat exchangers are unsuitable for condensation processes.

The energy consumption for transportation of water flow through both types of heat exchangers is approximately equal and it is not taken into account. For estimation of electrical energy expenses, it is necessary to compare the energy consumption for transportation of gas flow through the finned tube with the sum of energy consumed for gas transportation through the contact economizer and for liquid circulation in the contact economizer system. Gas fans and water pumps have nearly the same efficiency. So, comparison of their theoretical consumption of electricity can be made. Fig. 7 shows the ratio of electric energy consumption for operation of CE and for finned tube heat exchangers at their optimal gas velocity, as a function of the flue gases initial temperature. The curves show various initial temperatures of the heated water. They are obtained using the equations and particular values already given above.

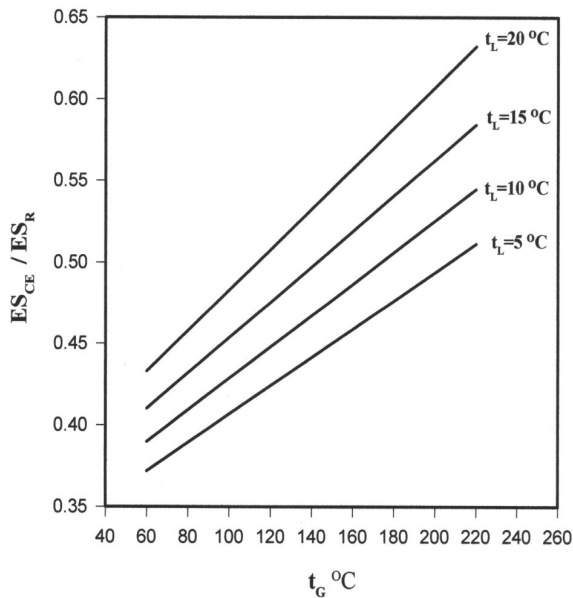


Fig. 7. Ratio of electric energy consumption for operation of CE and for finned tube heat exchanger at their optimal gas velocity, as a function of the flue gases initial temperature t_G at different values of the input temperature t_L of the water being heated.

The water - gas ratio, used for calculation of the liquid phase energy consumption in contact economizers systems, is determined from the heat energy balance.

CONCLUSION

The comparison clearly shows the superiority of the systems with contact economizer over the heat exchangers with finned tubes, both in terms of capital costs and heat recovery.

An advantage of the finned tube heat exchangers, in comparison to contact economizers systems, is their simple technological scheme and simple operation. That is why, in case of small boilers with capacity of 1 - 1.5 MW, where the difference in the efficiency for both types of installation is not too large, it may be better to use the finned tube heat exchangers. It must be considered that condensation of water vapor on the heat exchanger fins leads to corrosion. In Fig. 8 below is a graph with a condensing temperature of 55 °C and an air excess $\lambda=1.1$ showing the area in which the finned tube heat exchanger can be used.

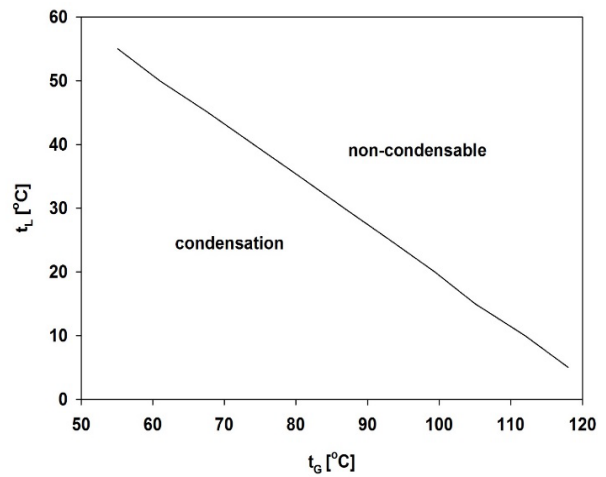


Fig. 8. Curve along which the fin temperature of the finned heat exchanger is 55°C condensation point, t_L is the supply temperature for heating cold water, t_G is the outlet temperature of the boiler operating at an air excess $\lambda=1.1$.

INNOVATION

The greatest economic effect would be the simultaneous operation of both apparatuses finned tube heat exchangers and contact economizers. The flue gases first pass through the finned tube heat exchanger 8 (Fig. 9) and then through the contact economizer 2 [11]. The heating water first passes through the plate heat exchanger 4 and then through the finned tube heat exchanger 8. This circuit solution makes it possible to utilise a greater amount of heat than with finned tube heat exchangers, and to raise the temperature of the heated water above the wet thermometer.

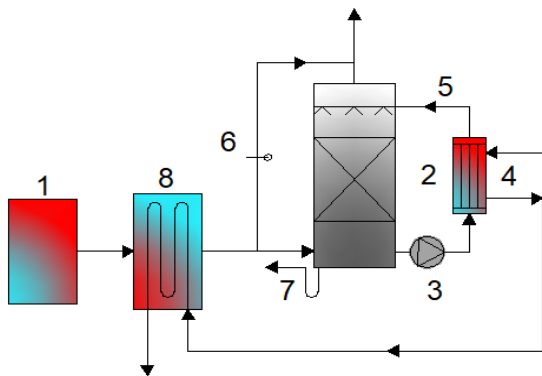


Fig. 9. Technological scheme of the proposed innovation [11]. Boiler 1, contact economizer 2, circulating pump 3, plate heat exchanger 4, liquid distributor 5, bypass valve 6, hydro-locking device 7, finned tube heat exchanger 8.

NOMENCLATURE

A, B, C and D - experimental constants given in [5];

C_p - specific heat at constant pressure, kJ/kgmol;

h - enthalpy, kJ/kgmol;

K - heat transfer coefficient, $W/(m^2 \text{ } ^\circ C)$;

P - partial pressure of water steam, mm Hg column;

Q - amount of heat in flue gases obtained by burning of 1 kmol natural gas, kJ;

T - flue gas temperature, K;

Z - price of an installation producing 1 kW heat power, $\$/m^2$;

α - gas-phase heat-transfer coefficient, $W/(m^2 \text{ } ^\circ C)$;

ΔP – pressure drop, Pa;

Δt_m - mean temperature difference, $^\circ C$;

λ - coefficient of air excess.

Subscripts

i refers to the corresponding component;

CE contact economizer;

R ribbed-pipes;

G gas;

L liquid.

REFERENCES

1. I. Iliev, Methods and means for efficient utilization of waste heat from low potential steam-gas streams, Academic Publishing Center of Ruse University "A. Kanchev", 2023, ISBN: 978-619-90013-9-4 (2013) (in Bulgarian).
2. D. Kolev, N. Kolev, *Applied Thermal Engineering*, **22**, 1919 (2002).
3. M. Yuan, G. Liu, X. Zhang, W. Zhang, Y. Yang, J. Song, H. Chang, L. Lim, *International Journal of Heat and Mass Transfer*, **205**, 1 (2023).
4. D. Kolev, *Bulgarian Chemical Communications*, **35** (3), 153 (2003).
5. R. C. Reid, J. M. Prausnitz, T. K. Sherwood, The Properties of Gases and Liquids, Third edn., McGraw-Hill Book Company, ISBN-13978-0070517998, (1987).
6. Chemist's manual, vol. III, Chemistry, Gosudarstvennoe nauchno - technicheskoe izdatel'stvo khimicheskoi literatury, Moscow, 1964 (in Russian).
7. S. Rivkin, A. Aleksandrov, Thermodynamic properties of water and water steam, Technics, (1978) (in Bulgarian).
8. Klimatech prospect, 8400 Dimitrovgrad, 1 Brodsko chaussee str. (in Bulgarian).
9. I. Z. Aronov, Contact heating of water by burning natural gas, Nedra, Leningrad, 1985 (in Russian).
10. N. Kolev, Kr. Semkov, R. Daraktchiev, *Heat Energetics*, **3** (8, 9), 6 (1990) (in Bulgarian).
11. N. Kolev, D. Kolev, R. Daraktchiev, Bulgarian Patent: A method for utilization of heat of humid gases and an installation for its realization, Reg. No. 101 404, April 10, 1997.

Influence of a weak pulsed magnetic field on the recovery and recrystallization in aluminum

A. Brusov, M. Azoulay, G. Orr, G. Golan*

Ariel University, Science Park, Ariel 40700, Israel

Received: April, 15, 2023; Accepted: February 19, 2024

Pulsed Magnetic Field (PMF) is an easy and effective method for changing the properties of various materials. In this work we present the influence of a weak pulsed magnetic field (WPMF) on the recovery and recrystallization processes in 99.99% aluminum. The state of the material before and after processing was determined by the method of Internal Friction (IF). It was found that if WPMF is carried out simultaneously with heating and annealing of deformed aluminum, then the recrystallization process is observed at lower temperatures. Pre-treatment with WPMF for 72 hours before annealing reduces the height of the IF peak and causes a more intense decrease in the level of IF at temperatures of 350°-400°C. Thus, the aftereffect of the WPMF during the recrystallization of deformed aluminum can be monitored.

Keywords: aluminum, weak pulsed magnetic field, internal friction, recovery, polygonization, recrystallization

INTRODUCTION

In recent years, interest has grown in processing with pulsed magnetic fields, as it is an easy and effective method for changing the properties of various materials, including non-magnetic ones. Of particular interest is the use of processing pulsed fields in the range of treatment with weak magnetic pulses ($H < 10^6$ A/m) or the so-called weak "magnetic field processing" (MFP). Magnetoplastic effect in non-magnetic crystals, internal friction and the effect of constant magnetic field on mechanical properties and dislocation structure of Nb and Mo are detailed in [1, 2] originated the topic on weak pulsed fields. This topic clarified the issue of the effectiveness of the impact of such magnetic treatment on non-magnetic materials. Subsequent studies [3-5] are in good agreement with this concept. It is known that MFP changes the state of impurity-defect complexes on dislocations, and therefore affects materials that are in an unstable transition state and can change properties that depend on the dislocation structure. MFP affects the processes of microplastic deformation, irreversible temper brittleness, and strain aging [6]. Aluminum is used as a substitute for more expensive metals, and the possibility of its use in various applications increases every year. A feature of aluminum (as a metal with a high energy of stacking faults) exhibits the tendency to creep dislocations, and facilitates the formation of structural defect complexes. As a result, there is a strong dependence of its plastic and strength properties on the dislocation structure. Therefore, it can be assumed that treatment with a weak pulsed magnetic field will be effective when exposed to aluminum under conditions of a change in the

dislocation structure during the processes of recovery, polygonization, and recrystallization. The method of internal friction (IF) was used, as the most sensitive one in the study of structure-dependent properties. Kong and Fang [7] observed a relaxation peak of internal friction on pure polycrystalline aluminum with a maximum temperature of 280°C at a frequency of 1 Hz. They showed that this peak is attributed to grain boundary, since it could not be found in single-crystal aluminum. The torsion pendulum method was used to detect bismaleimide triazine (BT) peaks on copper, iron, manganese, bismuth, and other metals. It was believed that they have a grain-boundary nature and are associated with viscous intergranular slip. Later, Woïrgard discovered IF peaks on deformed single crystal metals using the low-frequency flexural vibration method. The appearance of these peaks was associated with the glide of dislocations. According to a later representation [7], the IF peak was found to consist of at least two components, low- and high-temperature components. Despite the fact that the solution of this issue continues to be relevant [7], all researchers agree that internal friction is a very sensitive indicator for changes in the dislocation structure of a material. The method of internal friction can predict the interaction of vacancies, impurity atoms and dislocations. Also, it can predict the processes of formation of impurity defect complexes (IDCs) on dislocations. Therefore, in the current work, it was found that this method is useful to study the effect of WPMF on the dynamics of structural rearrangement of aluminum during processes of recovery, polygonization, and recrystallization, as well as the effect of magnetic

* To whom all correspondence should be sent:
E-mail: gadygolan@gmail.com

treatment on low-temperature peaks at 80°C, 150°C and the Ke peak.

MATERIALS AND PROCESSING

The object of the study was 99.99% aluminum, details are shown below in Table 1. Samples of 3×3×25 mm were deformed by tension of 10%.

Table 1. Residual impurities in 99.99% aluminum

Al	Fe	Si	Mn	Zn	As	N
base	0.006	0.002	0.001	0.0004	0.0002	0.0005

The internal friction was studied on a low-frequency apparatus of the inverted torsion pendulum type. The scheme of the setup is shown in Fig. 1. This laboratory setup makes it possible to simultaneously carry out magnetic processing and heat treatment, such as annealing, hardening, tempering, and to measure internal friction during the entire process. The setup consists of three main elements: 1 - installation for measuring internal friction of the type of reverse torsion pendulum with low oscillation frequencies of 0.5-1 Hz; 2- magnetic solenoids (6 in diagram) which are connected to the installation for processing with magnetic field pulses; 3- heating furnace (5 in diagram).

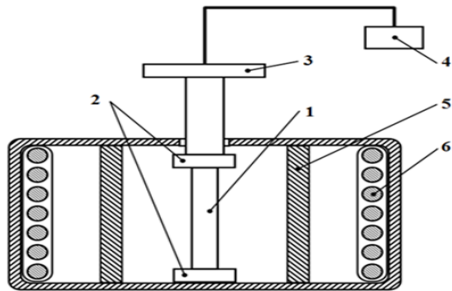


Fig. 1. Setup to study the effect of a pulsed magnetic field on a material, simultaneously with heat treatment. 1- sample; 2- clamps; 3- inertial detail; 4- counterweight; 5- heating chamber; 6- magnetic solenoid.

The processing parameters of the pulsed magnetic field were: magnetic field amplitude $H=3 \cdot 10^5 \text{ A/m}$, pulse repetition rate 0.5 Hz, pulse leading edge duration 10^{-4} s .

The study of the effect of a pulsed magnetic field on the recovery process was carried out at an annealing temperature of 100°C. The deformed aluminum specimens were rapidly heated (6-7 min) from room temperature to 100°C and then kept at this temperature for 1 hour. The influence of the magnetic field was studied directly during heating, annealing, and IF (internal friction) measurements. To study the processes of polygonization and recrystallization, the deformed samples were heated

at a rate of 4 °C/min to annealing temperatures, kept for 40 minutes, and slowly cooled at a rate of 15 °C/h to room temperature. The annealing temperature was varied from 200°C to 600°C with an interval of 100 °C. The aftereffect was studied in the following way: aluminum was treated with magnetic field pulses for 5 minutes at room temperature, then the samples were kept for 3 days, after which they were annealed, and the IF was measured. We studied the temperature dependence of the internal friction at relative strain amplitude of the material $\epsilon = 2 \times 10^{-5}$. The measurement error did not exceed 10%.

RESULTS AND DISCUSSION

The temperature dependence of the internal friction of aluminum with and without magnetic field treatment during the recovery process is shown in Fig. 2.

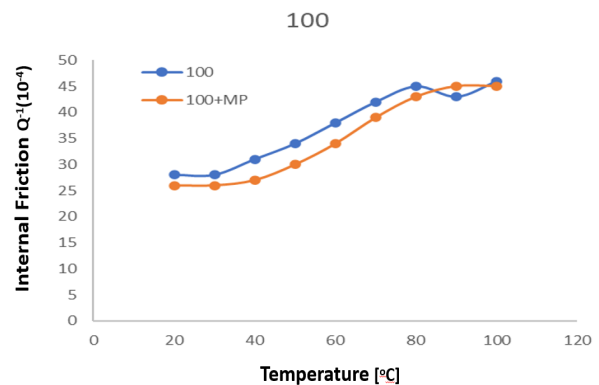


Fig. 2. Temperature dependence of internal friction in aluminum (purity 99.99%) during annealing at a temperature of 100 °C: 1-without a pulsed magnetic field; 2-with a pulsed magnetic field.

The results of studying the temperature dependences of IF show that under normal conditions of sample heating in the return temperature range, there is a monotonous increase in the level of IF. A slight increase in IF value is observed around 80 °C. This small peak flattens out after MFP treatment, while the background level of IF is somewhat lower than the level without treatment.

The effect of MFP on recrystallization and polygonization processes was studied on samples that were annealed as described previously. Then the samples were mounted in a setup and heated to a temperature of 500°C at a rate of 25 °C/h. IF was measured without WPMF treatment and with treatment by heating at intervals of 10°C to a temperature of 110°C, at intervals of 20°C to a temperature of 400°C, and at intervals of 50°C to a temperature of 500°C. The results obtained are presented in Figs. 3-6.

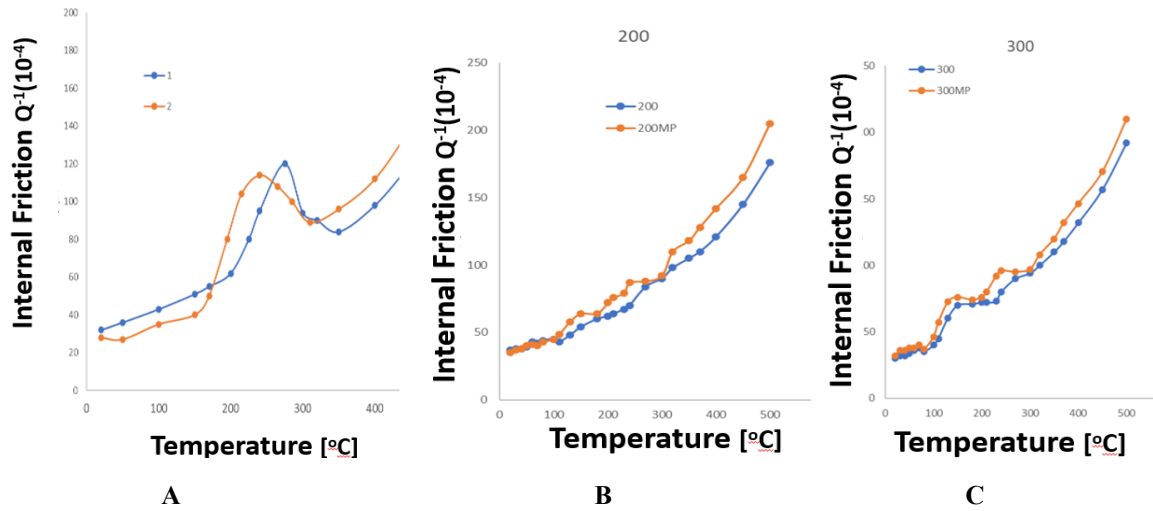


Fig. 3. Temperature dependence of internal friction in aluminum (purity 99.99%): A-deformation 10% without annealing; annealing at temperature: B-200°C; C -300°C. Curve 1 - without pulsed magnetic field; curve 2 - in a pulsed magnetic field.

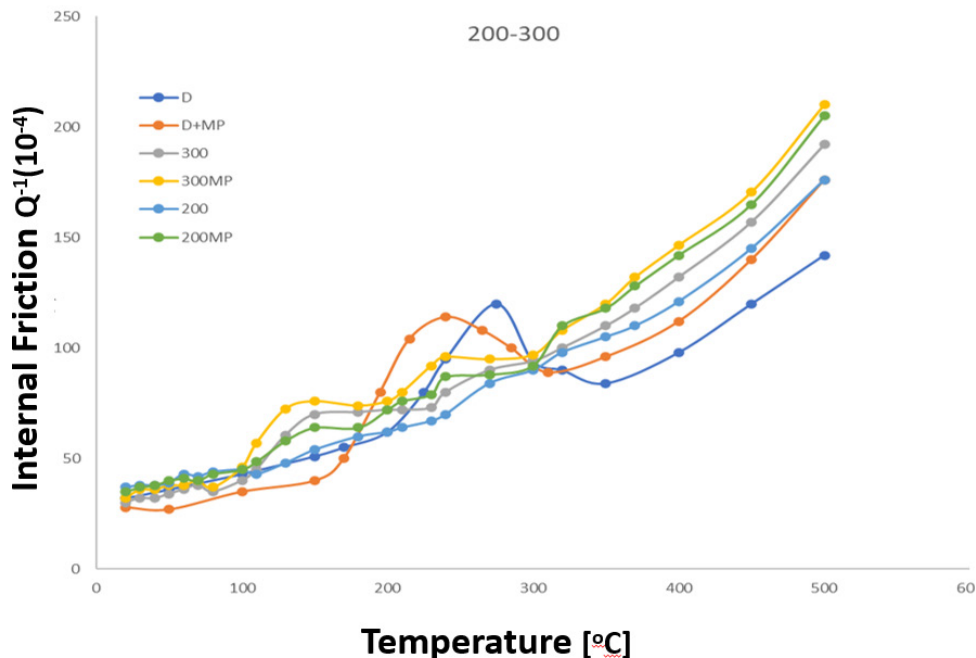


Fig. 4. Summary graph of temperature dependences of internal friction after: D - 10% deformation without annealing, after annealing 200°C and 300°C. Lines 200 and 300 without pulsed magnetic field; D+ MP, 200MP, 300MP - in a pulsed magnetic field.

Peak K_e , located in the region of 270°C, is the highest one and has the largest half-width after deformation, but after annealing at 200°C, it practically disappears (Fig. 4). This peak becomes very small in the curve after annealing at 300°C. After annealing at 300°C, another peak appears around 150°C (Fig. 3c, curve 1). This peak is associated with lattice dislocations. After annealing at 200°C without PMF treatment, no peaks are observed (Fig. 3b, curve 1). MFP treatment affects

the processes of structural rearrangement during annealing of deformed aluminum, which is confirmed by changes in the temperature dependences of IF. All types of peaks are shifted to lower temperatures by about 30°C, after pulsed magnetic treatment (Fig. 3). Also, after MFP treatment, small peaks appear on the curves after annealing at 200°C (Fig. 3b, curve 2) at the same temperatures, namely 150°C and 240°C, as during annealing in a magnetic field at 300°C.

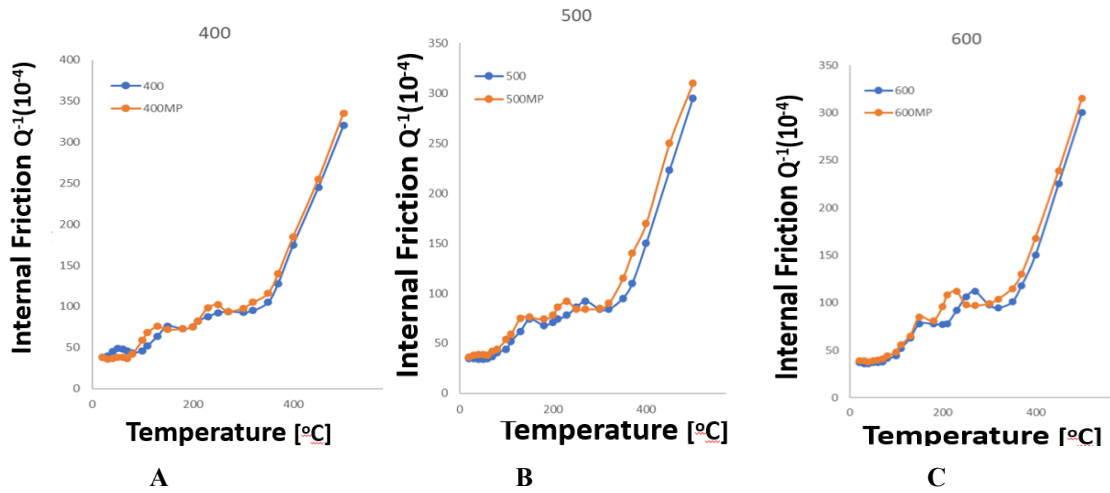


Fig. 5. Temperature dependence of internal friction in aluminum (purity 99.99%) after annealing at temperature: A-400°C; B-500°C; C-600°C. Curve 1 - without pulsed magnetic field; curve 2 - in a pulsed magnetic field.

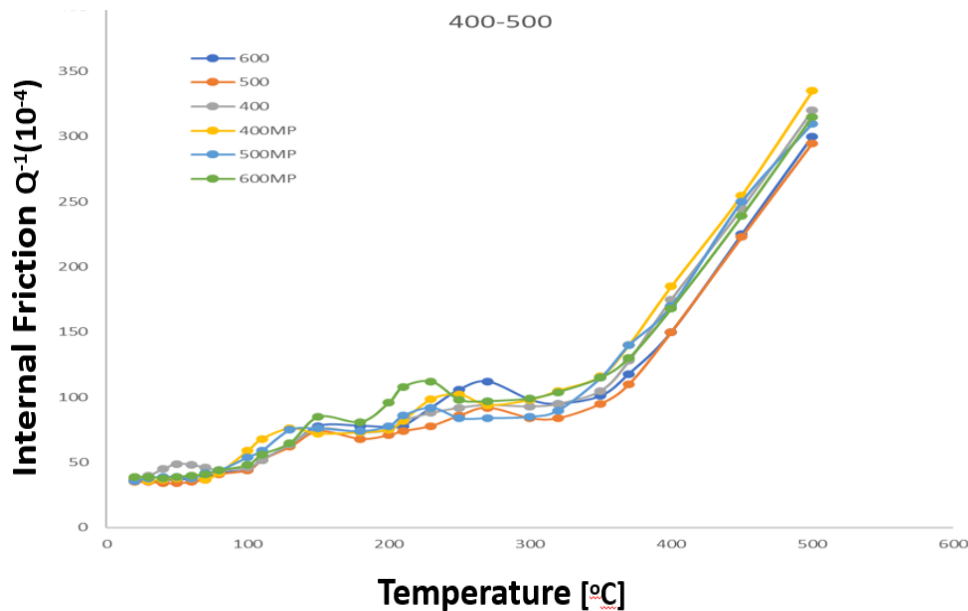


Fig. 6. Summary graph of temperature dependences of internal friction after deformation of 10% and annealing at temperatures of 400°, 500°C, and 600°C. Curves 400, 500, and 600 without pulsed magnetic field; curves 400MP, 500MP, 600MP - in a pulsed magnetic field.

The temperature dependences of IF during further annealing at higher temperatures are shown in the graphs 5-6. Peak K_e (270°C) is clearly seen after annealing at 400°C, gradually increasing with the annealing temperature and strongly increasing at annealing at 600°C (Fig. 6, curves 400, 500, 600). However, the height of the main peak does not restore its original value before deformation. The peak at 150°C, which appeared after annealing at 300°C, slightly increases with increasing annealing

temperature. Treatment in a pulsed magnetic field leads to a shift of the K_e peak by approximately 25–35°C to lower temperatures, while the peak height remains approximately at the same level; this trend is typical for all annealed states. The low-temperature peak (150°C) also shifts towards low temperatures by 20-30 degrees (curve 2 in Figs. 5 a, b, c). The results of the study of the aftereffect are presented in Fig. 7.

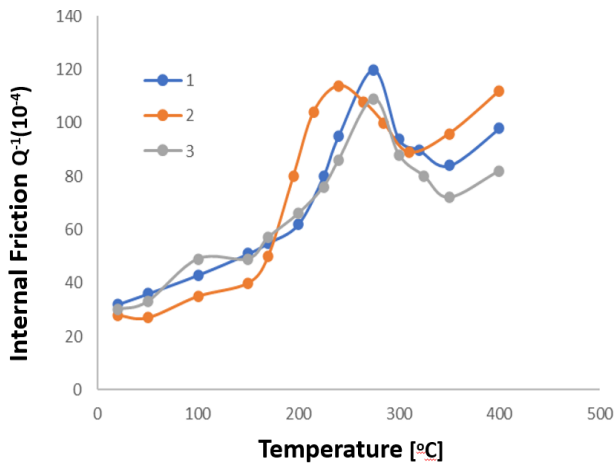


Fig. 7. Temperature dependence of the internal friction in deformed aluminum with a purity (99.99%): 1- without a pulsed magnetic field; 2- in a pulsed magnetic field; 3- aftereffect of the magnetic field.

On the curve with MFP aftereffect (Fig. 7, curve 3), a slight decrease in the IF peak is observed, but in general, this curve coincides with the curve without MFP. The decrease in the level of internal friction on the aftereffect curve at temperatures of 350–400°C occurs more intensively than on the other two curves. The data obtained confirm the possibility of the influence of a weak pulsed magnetic field on the processes of structural rearrangement during the processes of polygonization and recrystallization of deformed polycrystalline aluminum with a purity of 99.99 (annealing at 200°-600°C). The processes of change in the dislocation structure, which are characteristic of polygonization and recrystallization, proceed more intensively and begin earlier under the influence of MFP. This corresponds to the fact that the MFP treatment, acting on the dislocation system - impurity-defect complexes, leads to a decrease in the activation energy of grain-boundary relaxation, a decrease in the dislocation density and a shift of the Ke peak to lower temperatures. The effect of MFP on the recovery process on the temperature dependences is not significant (annealing at 100°C).

The observed changes in the nature of the peaks at 150°C confirm that these peaks are associated with dislocation relaxation, which also proceeds more actively and begins at lower temperatures under the action of magnetic fields.

CONCLUSIONS

From the above results it can be deduced that the exposure to a weak pulsed magnetic field simultaneously with heating and annealing leads to a shift of the grain boundary peak of IF by 20-30°C lower, that is, it accelerates the processes of structural rearrangement occurring during polygonization and recrystallization, which begin at lower temperatures. Moreover, the aftereffect of the MFP (the effect of magnetic treatment on the material before heating and tempering) is manifested by a decrease in the height of the peak of internal friction and a more intense decrease in the IF level at temperatures of 350°- 400°C. It is also printed out that the MFP affects low-temperature IF peaks (150°C) which are caused by lattice dislocations. This means that the magnetic field affects not only the grain boundary relaxation but also the dislocation relaxation, while the dislocation relaxation behaves similarly to the grain boundary relaxation.

REFERENCES

1. V. I. Alshits, E. V. Darinskaya, O. L. Kazakova, E. Yu. Mikhina, E. A. Petrzhik, *Journal of Alloys and Compounds*, **211/212**, 548 (1994).
2. V. A. Pavlov, I. A. Pereturina, I. L. Pecherkina, *Physica Status Solidi A*, **57**, 4491 (1980).
3. S. Akram, A. Babutskyi, A. Chrysanthou, D. Montalvão, M. J. Whiting, N. Pizurova, *Wear*, **480**, 203940 (2021).
4. C. Z. Liao, Y. Qin, Y. Yang, G. L. Xu, G. Yang, H. J. Gao, M. X. Wu, *J. Manuf. Processes*, **81**, 798 (2022).
5. M. Yan, C. Wang, T. Luo, Y. Li, X. Feng, Q. Huang, Y. Yang, *Acta Metall. Sin.*, **34**, 45 (2021).
6. O. I. Datsko, V. I. Alekseenko, A. L. Brusova, *Zh. Tekh. Fiz.*, **69**, 122 (1999).
7. Q. P. Kong, Q. F. Fang, *Critical Reviews in Solid State and Material Sciences*, **41**(3), 79, (2016).

Solar and heat pump hybrid heated greenhouse in Latvia: energy storage and CO₂ reduction

A. Auce^{1*}, A. Jermuss², A. Rucins², I. Auce³, I. A. Horns¹

¹University of Latvia, Institute of Chemical Physics, Raiņa bulvāris 19, Riga, Latvia

²Latvia University of Life Sciences and Technologies, Lielā iela 2, Jelgava, LV-3001, Latvia

³Institute of Advanced Technologies, Ciekurkalna 1. Linija 33, Riga, LV-1026, Latvia

Received: April, 15, 2023; Accepted: February 19, 2024

In the agricultural sector, heating greenhouses are one of the largest consumers of heat, and the cost of heat is a major part of total expenses. The volatile prices of fossil fuels and their negative impact on climate change make it necessary to find solutions for more efficient use of alternative energy sources. The aim of this study was to investigate possible solutions for converting an existing natural gas-heated greenhouse into a carbon-neutral greenhouse. This study investigates the use of solar energy to heat a 50 m² experimental tomato greenhouse (EG) with a hybrid module consisting of integrated installations of 8 kW solar photovoltaic (PV) panels combined with a 5.0 kW air-to-water heat pump (AWHP), 15.0 kW solar collectors (SC), a 10 kWh solar energy accumulator (SEA) and a 1600 L water heat accumulator (WHA). The interaction between the different parts of the heating system and the energy storage was investigated and compared with a reference industrial greenhouse (RG) on the same site. Excess solar energy was stored in a hot water storage tank (36 L m⁻²) and in a battery (0.2 kWh m⁻²). The energy storage requirement was determined to be 3-10 kWh m⁻² for the tomato production season from March to October. For a day/night cycle, 0.2-0.3 kWh m⁻² of electricity storage or 1 kWh m⁻² of heat storage was found to be sufficient. The use of an air-to-water heat pump optimises the amount of energy to be stored and the cost of energy storage, while reducing CO₂ emissions by at least a factor of 8 compared to natural gas heating. The electricity cost of the hybrid module is estimated to 30 % lower than natural gas heating in the 2021 and 2022 seasons. The calculations are based on the Nordpool day-ahead electricity price and the natural gas market price.

Keywords: Solar energy, air-to-water heat pump, CO₂ reduction, greenhouse, Latvia, energy storage

INTRODUCTION

According to the FAO, an estimate of 405 000 ha of greenhouses are spread throughout the EU [1], a figure that includes both glass- and plastic-covered structures. In 2022, there were 62.2 ha of greenhouses in Latvia, of which 32.2 ha heated [2].

Greenhouse agricultural production is generally seen as one of the most intensive parts of agricultural production [3, 4] as compared to energy use in open-field agriculture [5]. However, the role of greenhouse agriculture in the European food systems is not well-documented [6], while a small number of studies have been conducted that document energy use in greenhouse production.

EU Green Deal [7] announced the need for broad changes in the energy in all sectors of the economy including agriculture. The production of thermal energy accounts for 65.6 % of the total greenhouse gas emissions in Latvia [8]. The heating energy demand represents about 70-80 % of the total greenhouse energy consumption [9].

Increasing fossil fuel prices [5], scarcity of fossil fuel resources [10], and the global warming problem resulted from the combustion gases emittance has

prompted turning to alternative energy sources or enhancing the thermal efficiency of the existing heating systems [5, 11].

In this context, greenhouse cultivation is a significant energy consumer but there is relatively little data available and taking into account the implementation of EU climate targets and its farm-to-fork strategy in agriculture, it is apparent that there is a need to move towards sustainable production practices. To understand the future of greenhouse production in the EU and how they can contribute to a sustainable transformation of our agricultural systems, it is necessary to understand the energy use in greenhouses [12].

One of the most heat-intensive productions in agriculture in Latvia are greenhouses. Greenhouses in Latvia climatic conditions require heating during most of the year, the precise heating regime being dependent on the culture produced. Therefore, the transition of the greenhouses to CO₂-neutral heating systems is an important part of the overall efforts to reduce greenhouse gas emissions.

The velocity of the transition to new technologies can be made a very important factor as are the costs

* To whom all correspondence should be sent:
E-mail: agris.auce@lu.lv

of transforming the greenhouse industry to low CO₂ emission model.

In Latvia, a lot of the existing industrial greenhouse fleet use hot water central heating with natural gas. One of the ways for fast and relatively inexpensive transition is to replace the natural gas with another heat source leaving the rest of the technology intact. For example, to replace the gas boilers with biomass boilers. An alternative approach is by replacing natural gas with the combination of solar collectors (SC), electricity from photovoltaic (PV) panels and air-to-water heat pump. Their emission payback time is about one year but PV panels and solar collectors heating systems can be repaid in a short time period [13, 14].

The aim of this study was to investigate possible solutions for converting an existing natural gas-heated greenhouse into a carbon-neutral greenhouse. Particular attention was paid to requirements of heat storage for the greenhouse heated by a hybrid combination of solar energy and air-to-water heat pump.

An experimental greenhouse heated with the combination of SC, electricity from PV panels and air-to-water heat pump (AWHP) was designed and built to test the technology and the interaction between different heat sources. It is well known that the use of solar energy requires energy storage, and the affordability of proper energy storage facilities can be a limiting factor for the use of solar energy [15].

MATERIALS AND METHODS

The investigated 50 m² experimental greenhouse with beef type tomato *Solanum Lycopersicon* L. was detached from an industrial facility near the city of Jekabpils in South-East of Latvia (56.500197, 25.775123), 80 m high above sea level. The design, heating system and data acquisition system are detailed in [16, 17]. The warmest month in Jekabpils is July, its average air temperature is +18.1 °C. On the other hand, the coldest months of the year with an average air temperature of -4 °C are January and February. The last 10 years average in year intensity of solar radiation is 983 kWh m⁻², but the local weather station of the greenhouse recorded 1150 kWh m⁻² of solar radiation intensity in 2022, 1900 hours of sunshine, 4400 hours of light and 4300 hours of darkness, Figure 1. The actual climatic data were obtained from the weather station of the industrial facility located near the experimental greenhouse.

A solar hot water heating system with 15 kW peak power (0.3 kW m⁻²) and solar photovoltaic (PV) panels with 8 kW peak power (0.15 kW m⁻²) optimized for spring/autumn were installed. 1600 L

water heat accumulator system and 2 batteries of 5 kWh each were used, Figure 2.

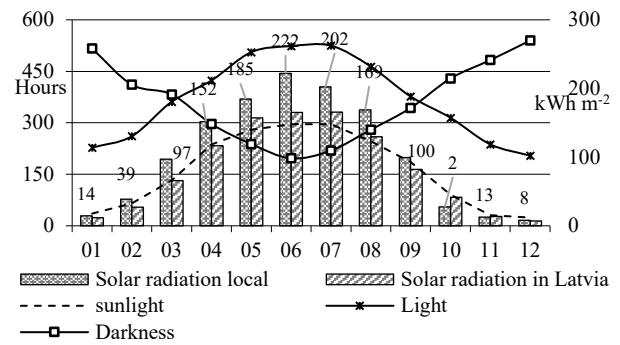


Fig. 1. Intensity of solar radiation in Latvia, 2022.

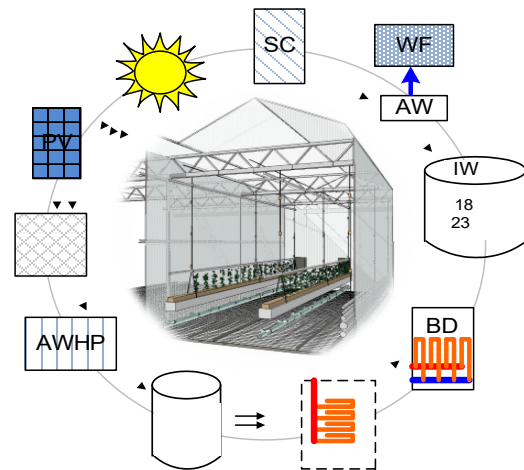


Fig. 2. Provision of heat supply of the experimental greenhouse with solar energy, a full-cycle scheme, where: PV - solar panels; SC - solar collectors; EA - storage battery for solar electricity; AWHP - air-to-water heat pump; WHA - water heat accumulator; GH - experimental greenhouse heating system; AW - irrigation water; WF - irrigation water filter; IWH - irrigation water heating; BD - drying of biomass; AW - Artesian well water, ~10 °C.

One Hitachi RWH-4.0VNFE air-to-water heat pump (AWHP) of 5.33 kW electrical power (10 kW heat power) was installed. The energy from the grid made up the difference when there was insufficient energy from the solar system. The need for energy accumulation for the day/night cycle was calculated to be 0.2-0.3 kWh m⁻² for electrical power storage or 1.0 kWh m⁻² for the heat power storage. These power storage requirements are economically affordable and are comparable to the cost of the PV cells. As for the heat power storage, usually, industrial greenhouses already have this capacity installed as a part of the existing heating system. In the experimental greenhouse a computerized temperature measurement system with 23 temperature sensors was used to control the temperature in the different parts of the heating system and in the greenhouse itself, as well as in the

reference greenhouse. Particular attention was paid to measuring the temperature of the heating water in different parts of the heating system. This was considered important because the coefficient of performance (COP) of the heat pump strongly depends on the temperature of the heating water. Using producers COP data at 4 outdoor temperature points and 2 heating water temperatures we interpolated the COP of the heat pump for all outdoor and heating water temperature combinations. The temperature measurement system read the data from the sensors with 30 second interval and the data were stored in a server that was accessible online for data downloads and analysis.

The study was done from the summer 2021 till winter 2023. Because of the huge volatilities of the energy prices (for both electricity and natural gas) the timing of the experiment was unfortunate for the economic analysis of the performance of the experimental system.

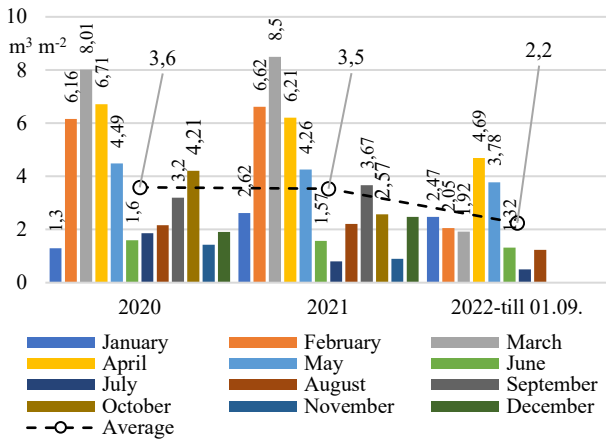


Fig. 3. Gas consumption and price in the reference greenhouse.

Due to the start of the war in Ukraine the energy prices for year 2022 were too extreme in Latvia to be used in any meaningful economic estimates. Therefore, the 2021 Nordpool day ahead electricity prices and the market prices of natural gas were used for the economic analysis, Figure 3.

RESULTS

In Latvia climate condition the greenhouse should be heated almost all the year with exception of sunny warm weather in summer. The greenhouse we studied – both the experimental greenhouse and the industrial reference greenhouse, were used for the part of the year with winter reserved for the servicing needs with minimal heating and thus minimal energy consumption during the winter time. Obviously, the highest need for heating energy is at the early spring and the late autumn. Due to the climatic conditions in Latvia and the dynamics of the

industrial production, the end of the season is the most important factor defining the requirements for the energy storage as the stored energy defines how long the productive season can be extended in autumn.

In this research the experimental greenhouse was heated with the combination of solar collectors and heat pump while the PV panels were used in two setups – in direct DC heating of hot water boiler to test a low-capital investment setup without DC/AC conversion and in a second mode with PV output converted to AC and used to drive the heat pump.

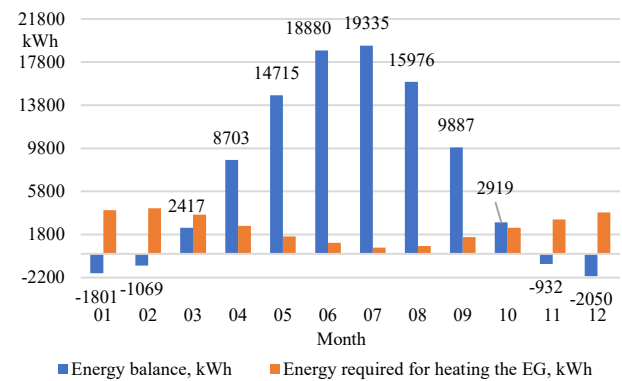


Fig. 4. Energy balance and required energy for heating, 2022, kWh.

In the combined regime of heating the experimental greenhouse with solar collectors and air-to-water heat pump the energy consumption of the heat pump was studied as it defines the potential need for the electricity storage or alternatively the costs of the electricity from the grid to supplement the renewables. The heat pump used on average 0.3-0.5 kWh m⁻² a day during May-August, 0.7-0.8 kWh m⁻² a day during April and August/September and 1-1.2 kWh m⁻² a day during October and March, Figure 4.

Availability of solar energy is out of phase with the need for heating both during the day/night and the seasonal cycles. Figure 5 shows the monthly distribution of the total energy used for heating by AWHP and the total energy produced by solar PV and solar collectors as the percentage of the total energy over the whole period.

The amount of the electrical energy for the heat pump depends on its COP that in turn is related to both heating water temperature and outdoor air temperature. COP can be increased designing the greenhouse in a way that minimizes the heating water temperature but, in this work, the experimental greenhouse was built to replace the existing industrial greenhouse heating system - fitted to gas boiler and using relatively high heating water temperatures of up to 60 °C by colder weather.

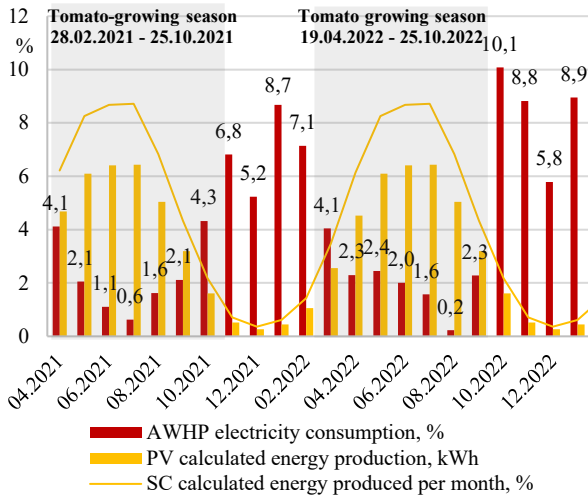


Fig. 5. Monthly energy distribution from various heating and energy sources. Grey area is the active tomato growing season. Energy represented as a part of total energy used in each of the months expressed as a percentage of the total energy over the whole period.

COP of air-to-water heat pump varies between 2 and 6.5 in the outdoor temperature range between -7 °C and +7 °C while difference in COP between heating water temperatures of 35 °C and 55 °C can be up to 30 %. During the warm season, from April to October, outdoor air heat pumps operate with a high COP. This means that for every unit of energy used to run the heat pump, we get 3 to 5 units of heat energy. As the temperature of the outdoor air decreases, the efficiency of use decreases. Our findings showed that the average COP in 2022 is 4.3, while it is 5.6 in the warm season from April to October and 2.8 in the hot season. The measurements of heating water temperatures in the experimental greenhouse stated that heating water temperatures are not directly related to the outdoor air temperatures as can be seen in Figure 6. There are a number of other factors like daily indoor temperature changes and solar irradiation that influence the heating water dynamics in the greenhouse [18]. As the COP of the AWP depends on the heating water temperatures, a performance of heat pump cannot be calculated using only outdoor temperature data because heating water can have any temperature for a given outdoor air temperature. In our work we used the theoretical performance of AWP from the experimentally measured heating water temperatures in the experimental greenhouse. Using the heat pump's factory-specified COP and comparing energy expenses – prices of electricity for AWP in the experimental greenhouse and gas for the gas boiler in the reference industrial greenhouse we estimated that the heat pump is economically a twice more efficient way of heating greenhouse than natural gas until the end of September 2021.

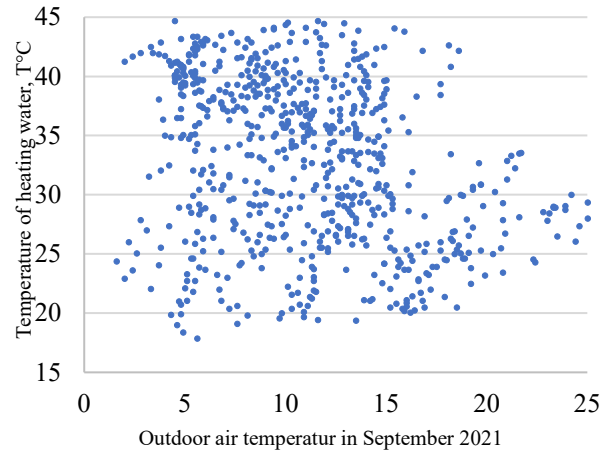


Fig. 6. The temperature of incoming heating water in the experimental greenhouse as function of outdoor air temperature.

2021 energy price data were used because of the war in Ukraine and the following energy price shock in the Baltic States. The 2022 price data were not suitable for analysis. As can be seen in Figure 7, the energy cost of AWP was considerably (more than twice) lower than the cost of natural gas heating. The fluctuations in the cost ratio in Figure 7, are due to day/night electricity price differences in Nordpool day ahead market.

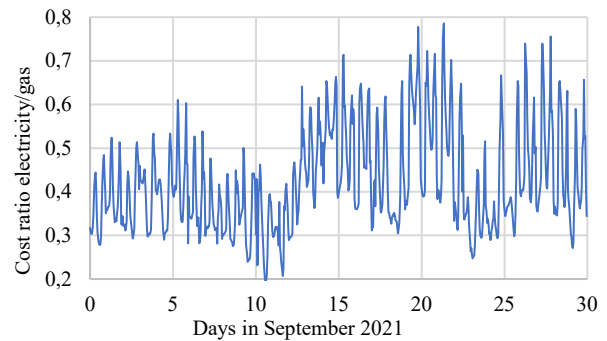


Fig. 7. Calculated cost ratio between grid electricity for AWP and gas for boiler in September 2021.

Hourly electricity consumption was calculated from interpolated COP values for hourly outdoor and heating water temperatures. The amount of natural gas to produce the same amount of energy was calculated using COP of 0.94 for the natural gas boiler installed at the reference industrial greenhouse.

Energy Storage

Several time intervals – intraday, day/night and finally the longer cold cloudy weather periods that should be covered by the energy storage, were identified. Intraday storage should accumulate the heat energy for cloudy periods of the day that might last several hours. Day/night cycle is further

complicated by the dynamics in the indoor temperature regime for the plants. The indoor temperature is some centigrades lower during night time that shifts heating energy consumption for some time delaying the need for heating in the evening and requiring more energy in the morning. The need for energy accumulation for the day/night cycle was calculated to be 0.2-0.3 kWh m⁻² for electrical power storage or 1 kWh m⁻² for heat power storage. These power storage requirements are economically affordable and are comparable to the cost of the PV cells. As for the heat power storage, industrial greenhouses already have this capacity installed as a part of the existing heating system.

In Latvia, the cold, cloudy periods may last up to 7–10 days or even longer. Some research has reported that changes in the polar vortex can bring longer periods of both warm and cold weather [19, 20]. Dunkelflaute’s studies, e.g. [21] will bring more insight into this climatic condition. We estimate that the requirements for the energy storage are defined by the requirement that the greenhouse heating system should be able to withstand at least 10 days’ cloudy cold spell during the productive season.

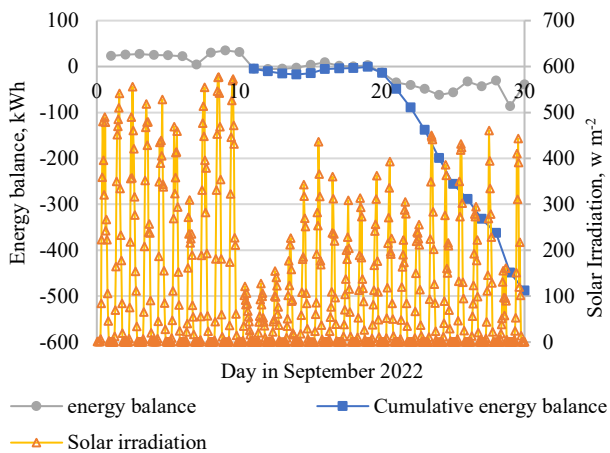


Fig. 8. Solar irradiation and both daily and cumulative energy balance in greenhouse in September 2022.

Clear sky conditions at the beginning of September come together with larger daily day/night temperature differences and the need for energy storage to cover heating for colder nights and surplus electrical energy produced by PV. Cloudy weather with more stable outdoor air temperatures in mid-September demonstrates conditions with energy balance close to zero. Solar irradiation and both daily and cumulative energy balance in the greenhouse in September 2022 are shown in Figure 8. With lower temperatures and partially cloudy skies the cumulative energy deficit starts to rise fast in the 2nd half of September and it cannot be covered by energy storage in an economically feasible way. Electricity

from the grid or other heat source like biomass or natural gas boiler should be used to cover the periods when there is not enough solar and stored energy.

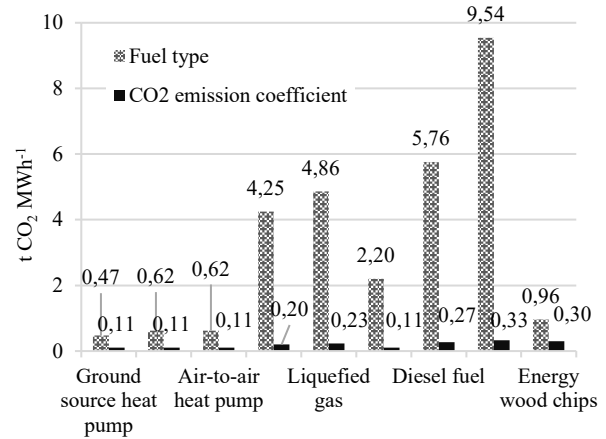


Fig. 9. CO₂ emissions associated with the EG heating.

When estimating CO₂ reduction in a hybrid heated greenhouse as compared to traditional natural gas heated greenhouses (Figure 9) an assumption should be made about the ratio of CO₂-free electricity in the grid. In Latvia, the electricity from the grid is approximately 75% CO₂-free, the overall effect of using the electricity from the grid is at least 5-8-fold reduction in CO₂ emissions as compared to gas.

CONCLUSIONS

Hybrid system using solar power by solar collectors and PV-driven air-to-water heat pumps can be used for greenhouse heating in Latvia, but it can’t cover the beginning and the end of the productive season of greenhouses and the current energy storage technologies do not allow heating with solar energy only.

Energy storage for the day/night cycle was calculated to be 0.2-0.3 kWh m⁻² for electrical power storage or 1.0 kWh m⁻² for the heat power storage. The costs for such storage facilities are economically affordable.

Grid-connected solar collector and PV driven air-to-water heat pump heating system for greenhouses reduces CO₂ emissions at least 8-fold as compared to natural gas heating. The cost of heat pump was lower than the cost of gas heating for temperatures above -3 °C at 2021 energy prices.

A topical issue for further research is the possibility of storing the excess energy produced by the system over a longer period of time in an ecologically and economically safe manner.

Acknowledgement: This research was funded by European regional development fund (ERDF) 2014-

2020 for operational groups, Project no. 18-00-a01620-000023.

Credit authorship contribution statement: Agris Auce: Conceptualization, Investigation, Funding acquisition, writing – original draft, Aivars Jermuss: Writing – review & editing, Adolfs Rucins: Writing – review & editing, Project administration, Ivars Auce: Conceptualization, Resources. Indulis Arnis Horns: Investigation, Methodology, Data analysis.

Declaration of competing interest: The authors declare that they have no known competing financial interests or personal relationships that could have appeared to influence the work reported in this paper.

REFERENCES

1. W. Baudoin, A. Nersisyan, A. Shamilov, A. Hodder, D. Gutierrez, S. Nicola, V. Chairperson, R. Duffy, Good Agricultural Practices for Greenhouse Vegetable Production in the South East European Countries Food and Agriculture Organization of the United Nations Plant Production and Protection Division Principles for Sustainable Intensification of Smallholder Farms; FAO: Rome, Italy, 2017, ISBN 978-92-5-109622-2. [Google Scholar].
2. Official Statistics Portal of Latvia (2023) [online] [31.03.2023]. Available at: https://data.stat.gov.lv:443/api/v1/en/OSP_PUB/ST_ART/NOZ/LA/LAG/LAG120
3. F. Tittarelli, *Agronomy*, **10**, 72 (2020). [Google Scholar] [CrossRef][Green Version]
4. EGTOP. Final Report On Greenhouse Production (Protected Cropping); EGTOP: Brussels, Belgium, 2013, p. 37, https://agriculture.ec.europa.eu/system/files/2019-03/final-report-etop-greenhouse-production_0.pdf
5. S. R. Yan, M. A. Fazilati, D. Toghraie, M. Khalili, A. Karimipour, *Renewable Energy*, **170**, 133 (2021), ISSN 0960-1481, <https://doi.org/10.1016/j.renene.2021.01.081>.
6. G. Popsimonova B. Benko, L. Karic, Gruda, N. *Acta Hortic.*, 137 (2017), <https://doi.org/10.17660/ActaHortic.2021.1326.18>
7. European Commission. A European Green Deal. [online] [16.03.2023]. Available at: https://commission.europa.eu/strategy-and-policy/priorities-2019-2024/european-green-deal_en
8. Latvia's National Inventory Report 1990 – 2018 under the United Nations Framework Convention on Climate Change (UNFCCC), the Kyoto Protocol.2020. Ministry of Environmental Protection and Regional Development of the Republic of Latvia.
9. S. Sanford, *Energy*, **3907**(01), 2011, p. 16, University of Wisconsin–Extension.
10. Sh.-R. Yan, M. A. Fazilati, R. Boushehri, E. Mehryaar, Da. Toghraie, Q. Nguyen, S. Rostami. *Journal of Energy Storage*, **29**, 101448 (2020), ISSN 2352-152X, <https://doi.org/10.1016/j.est.2020.101448>.
11. X. He, P. Wang, W. Song, G. Wu, C. Ma, M. Li, *Renewable Energy*, **198**, 1148 (2022), ISSN 0960-1481, [Accessed on 30.05.2023] Available at: <https://doi.org/10.1016/j.renene.2022.08.100>
12. B. Paris, F. Vandorou, A. T. Balafoutis, K. Vaiopoulos, G. Kyriakarakos, D. Manolakos, G. Papadakis, *Applied Sciences*, **12**(10), 5150 (2022). <https://doi.org/10.3390/app12105150>
13. D. Nikolic, J. Skerlic, J. Radulovic, A. Miskovic, R. Tamasauskas, J. Sadauskienė, *Renewable Energy*, **189**, 1063 (2022), [Accessed on 29.05.2023]. Available at: <https://doi.org/10.1016/j.renene.2022.03.075>
14. A. Bazgaou, H. Fatnassi, R. Bouharroud, K. Ezzaeri, L. Gourdo, A. Wifaya, H. Demrati, F. Elame, Á. Carreño-Ortega, A. Bekkaoui, A. Aharoune, L. Bouriden, Effect of active solar heating system on microclimate, development, yield and fruit quality in greenhouse tomato production, **165**, Part 1, 237 (2021) [Accessed on 29.05.2023] Available at <https://doi.org/10.1016/j.renene.2020.11.007>
15. Md M. Rana, M. Uddin, Md R. Sarkar, G. M. Shafiullah, H. Mo, M. Atef, *Journal of Energy Storage*, **51**, 104597 (2022), ISSN 2352-152X, <https://doi.org/10.1016/j.est.2022.104597>
16. A. Auce, A. Rucins, A. Jermuss, I. A. Horns, U. Grinbergs, 21st International Scientific Conference, May 25–27, 2022, Jelgava, Latvia, Conference Proceedings, Latvia University of Life Sciences and Technologies, 2022, **21**, p. 30, [online] [31.03.2022]. Available at: <https://www.tf.llu.lv/conference/proceedings2022/Papers/TF096.pdf>
17. A. Auce, I. A. Horns, S. Ivanovs, A. Jermuss, U. Grinbergs, A. Rucins, 21st International Scientific Conference, May 24–26, 2023, Jelgava, Latvia, Conference Proceedings, Latvia University of Life Sciences and Technologies, 2023, p. 636.
18. J. Pospisil, M. Špiplaček, L. Kudela. *Energy*, **154**, 415 (2018).
19. D. Hu, Z. Guan, W. Tian et al., *Nat. Commun.* **9**, 1697 (2018). [online]
20. J. Huang, P. Hitchcock, A. C. Maycock et al., *Commun. Earth Environ.*, **2**, 147 (2021). <https://doi.org/10.1038/s43247-021-00215-6> [31.03.2023]. Available at: <https://doi.org/10.1038/s41467-018-04138-3>
21. B. Li, S. Basu, S. J. Watson, H. W. J. Russchenberg, *Energies*, **14**(20), 6508 (2021); [online] [31.03.2023]. Available at: <https://doi.org/10.3390/en14206508>

Selection of the optimal kinetic scheme for the formation of nitrogenous substances in the simulation of low-quality coal combustion

S. Bolegenova^{1,2}, A. Askarova^{1,2}, A. Georgiev³, M. Beketayeva^{1,2*}, S. Bolegenova², V. Maximov¹, N. Adilbayev²

¹ETP SRI of Al-Farabi Kazakh National University, Al-Farabi av., 71, 050040 Almaty, Kazakhstan

²Al-Farabi Kazakh National University, Department of thermal physics and technical physics, Al-Farabi av., 71, 050040 Almaty, Kazakhstan

³University of Telecommunications and Post, Department of General Engineering, 1 Acad. Stefan Mladenov str., 1700 Sofia, Bulgaria

Received: April, 15, 2023; Accepted: March 01, 2024

The methods used to reduce emissions of harmful substances (mainly nitrogen oxides) at the moment still do not meet environmental requirements and don't give the desired result. In this article, a study was carried out by methods of 3D computer modeling of mass transfer processes using the example of low-quality coal combustion in the furnace chamber of a real heat-power facility. The choice of the kinetic model of the formation of nitrogenous substances is important for determining the most realistic scheme of the technological process of fuel combustion. The novelty of the proposed work is that in order to choose the optimal chemical model, two kinetic schemes for the formation of NO are considered, these are the Mitchell Tarbell model and the De Soete model. As a result of the conducted computational experiments, the high efficiency and adequacy of the Mitchell Tarbell kinetic model was noted in relation to the high-ash coal under study. This allows to conclude that the use of the Mitchell Tarbell model to reproduce the process of burning low-grade coals is preferable. The results obtained will help to realistically estimate the amount of NO emissions, as well as to design and implement various approaches to their minimization.

Keywords: emissions, 3D computer modeling, kinetic model, nitrogenous substances, low-grade coal

INTRODUCTION

Global coal consumption will hit a record high this year, the International Energy Agency (IEA) predicts. The world is close to the peak of fossil fuel use, and coal will be the first to be reduced, but we have not yet reached this. Despite the fact that the leading countries of the world announce their plans for 2020-2060 about achieving carbon neutrality, the rate of coal production does not seem to decline (Fig. 1).

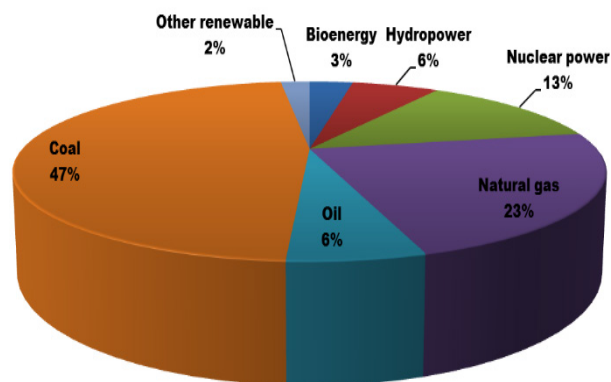


Fig. 1. World consumption of fuel resources

Demand for coal remains unwavering and is likely to hit record highs this year, pushing up global emissions. Top 10 countries by coal reserves: USA, Russia, China, Australia, India, Germany, Ukraine, Kazakhstan, South Africa, Indonesia. Top 10 countries by coal production: China, Indonesia, India, Australia, USA, Russia, South Africa, Kazakhstan, Poland, Colombia.

According to the World Energy Outlook (WEO) countries that have set targets for coal power phase-outs account for about 3% of global electricity generation. Unfortunately, in the first half of 2022 (H2), global coal consumption little changed (we estimate a decrease of less than 0.5%) compared with the first half of 2021 (H1), with the economic slowdown more than offsetting any demand increase resulting from higher natural gas prices (Fig. 2). For 2022, as a whole, WEO expects global coal demand to increase by 0.7% from 2021 to about 8 billion tons [1, 2].

In this term, WEO noted the two main aspects to phasing out coal in the energy sector: 1) stopping the construction of new power plants and 2) managing the reduction of emissions from existing assets.

* To whom all correspondence should be sent:
E-mail: beketayeva.m@gmail.com

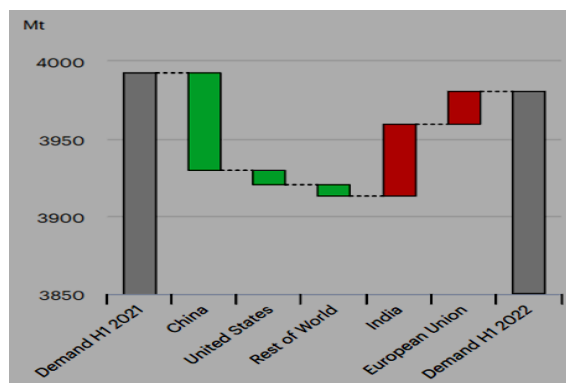


Fig. 2. Changes in global coal consumption by 2021-2022 (H1).

Advanced economies are seeing a faster phase-out of coal in the energy and industrial sectors. Demand will collectively decline by about 40% by 2030. This is due to climate policy and the rapid growth of renewable energy. Ensuring reductions in emissions from the existing fleet of coal-fired power plants is a major challenge for public policy. Given the dependence of a number of countries and regions on coal, the closure or conversion of coal mines and power plants can have serious economic and social consequences. Therefore, the use of coal, on the contrary, is expanding in many emerging markets and developing countries [2].

The thermal efficiency and environmental safety of energy enterprises is largely determined by the quality of the coals used. It is known that in developed countries (Germany, USA, etc.) only specially prepared fuel is burned, which is subjected to pre-enrichment, sorting, desulfurization, which certainly improves its quality [3-6].

In conditions of depletion of natural energy resources and environmental pollution, the rational use of energy fuel, increasing the efficiency of energy production and solving environmental problems are an urgent and important task that needs to be solved. The main energy fuel in Kazakhstan is coal. The poor quality of coal from the main Kazakh coal deposits leads to industrial and environmental problems during its operation. In this regard, studies of the processes of burning low-grade coals are relevant.

Conducting detailed and in-depth research in real conditions is much more expensive than conducting computational experiments using computer modeling methods. At the same time, the results obtained by computational methods can also ensure the development of effective technological solutions [7-9]. However, it is worth emphasizing here that the correct formulation of the problem in modeling plays a crucial role. Currently, there are various software packages and approaches being developed to obtain

adequate and most realistic results. Unfortunately, there are no universal approaches yet. Therefore, it is important to consider and study each task separately, thereby at least grouping the main points.

THE CONSIDERED SCHEMES FOR THE FORMATION OF NITROGEN OXIDES

Combustion processes occur under conditions of strong turbulence and non-isothermal flow, multiphase medium with significant influence of nonlinear effects of thermal radiation, interphase interaction and multistage flow of chemical reactions. Such phenomena play an important role in the study of the natural phenomenon of low-grade coal burning [10-14]. All these factors must be taken into account in the formulation of the physical, mathematical and chemical model of the problem. A number of kinetic schemes based on global reaction rates have been developed to describe the processes of formation and destruction of nitrogen oxides [15, 16].

The choice of the most optimal scheme for the formation of nitrogen oxides during the combustion of low-grade pulverized coal fuel will provide adequate research results. This will give a chance to really estimate the amount of nitrogen oxide emissions, as well as to design and implement various approaches to minimize it. In the process of burning coal, nitrogen oxides are formed during homo- and heterogeneous reactions of air, volatile substances and charcoal. Nitrogen oxides occur in combustion gases in the form of NO, N₂O, and NO₂ compounds. Fig. 3 shows a simplified diagram of the mechanism of their formation.

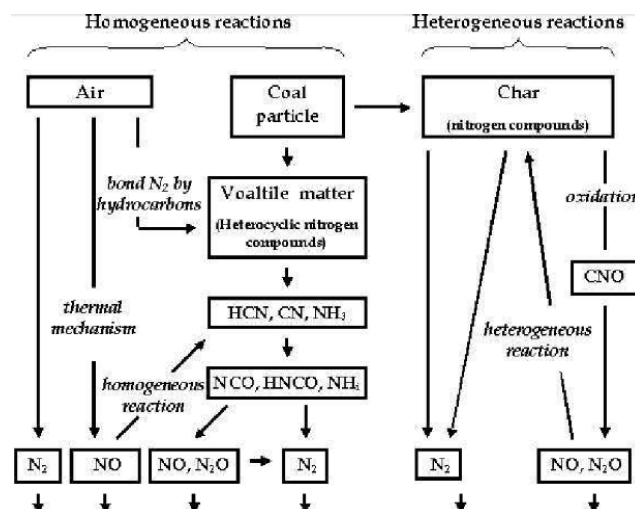


Fig.3. A simplified diagram of the mechanism of NOx formation

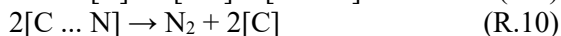
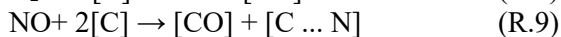
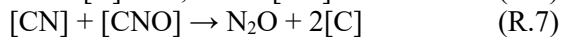
The complex mechanisms of nitrogen oxide formation during coal combustion are classified

using a nitrogen source and divided into two main groups:

- fuel processes: oxidation of nitrogen compounds that are chemically bound to the organic matter of the fuel;
- thermal processes: reactions of atmospheric nitrogen with atomic oxygen, which is formed at high temperatures.

Nitrogen associated with coal (fuel) is released during the removal of volatile components. A portion of the nitrogen is rapidly converted to HCN, and the remainder of the fuel nitrogen reacts to form NH₃. These two species react and produce either NO or N₂, depending on local conditions. The NO formed can be reduced by a heterogeneous reaction with carbon particles. Global reaction rates are usually measured under controlled conditions over the temperature range of interest and are applicable to both high fuel and low fuel conditions. Various values for global reaction rates have been proposed by De Soete, Mitchell and Tarbell, *et al.*

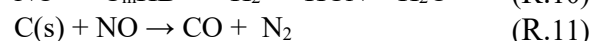
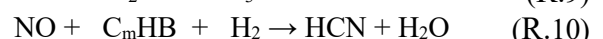
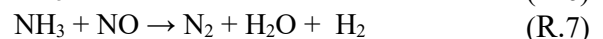
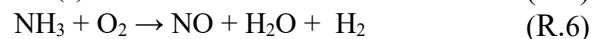
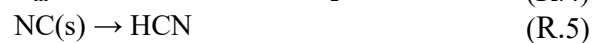
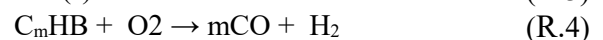
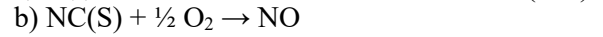
In the proposed article, the processes of formation of nitrogen oxides are considered, according to two kinetic models of their formation – the Mitchell Tarbell model and the De Soete model. De Soete was the first researcher to develop a heterogeneous model of the formation and decomposition of NO and N₂O based on surface reactions with active sites [CN] and [CNO]. De Soete model is based on ten NO and N₂O production and reduction reactions:



The disadvantage of this model is the lack of diffusion in the pores. However, at temperatures above 800 K, the formation of NO and N₂O is controlled by the diffusion of oxygen in the pores of the coal. At the same time, the probability of obtaining accurate results of modeling nitric oxide emissions from coal combustion without previous experiments is low.

In the case of coal combustion, the Mitchell Tarbell kinetic model of fuel NO formation takes into account coal pyrolysis, homogeneous combustion of hydrocarbons and heterogeneous

coke burning. The general reaction mechanism used in the kinetic model is given below:



Coal pyrolysis is described by R.3 and R.5, coal combustion - by R.1a, combustion of hydrocarbons formed in the process of the release of volatile coal components, is described by R.2, R.4 and R.12. R.8 - describes the mechanism of formation of thermal NO. The mechanism of formation of fuel NO is presented in R.1b, R.6, R.7 and R.9-11.

THE BASICS OF COMPUTATIONAL EXPERIMENTS AND RESULTS

To conduct computational experiments in the simulation of low-quality coal combustion, the FLOREAN software package [17-19] was used, which is based on solving conservative equations for the gas-fuel mixture using the control volume method.

The computer software package consists of a sub-model of the balance of momentum, energy, matter components, *k-ε* turbulence model, SIMPLE pressure correction method, six-stream thermal radiation model. This software package has been used to calculate flows in the combustion chambers of many thermal power plants both abroad and in Kazakhstan [20-26].

Based on the kinetic mechanism of the formation of nitrogen oxides NO_x according to the models of De Soete and Mitchell-Tarbell, computational experiments were carried out to determine the concentration characteristics of the formation and destruction of nitrogen oxides (NO and NO₂) in the furnace chamber of the boiler BKZ 75 Shaktinskaya CHP when burning high-ash Kazakh coal (see the characteristics of Karaganda coal in Table 1) in it.

Table 1. Characteristics of Karaganda coal

Name	Value
Grinding fineness (R_{90}), %	20
Density of coal, kg/m^3	1350
Heat of combustion of coal, kJ/kg	$3.4162 \cdot 10^4$
Heat of combustion of coke, kJ/kg	$3.2814 \cdot 10^4$
A^c , %	35.10
V^T , %	22.00
W^P , %	10.60
C, %	79.57
H ₂ , %	6.63
O ₂ , %	9.65
S ₂ , %	1.92
N ₂ , %	2.23

Figs. 4 and 5 show a plot of the distribution of maximum, minimum and average values of nitric oxide NO concentration over the height of the combustion chamber for two models of NO_x formation.

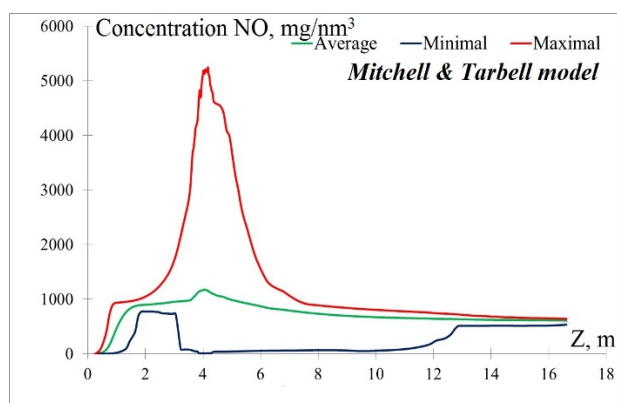


Fig. 4. Distribution of nitrogen oxide NO concentrations along the height of the combustion chamber of the BKZ-75 boiler for the NO formation model according to the Mitchell & Tarbell model

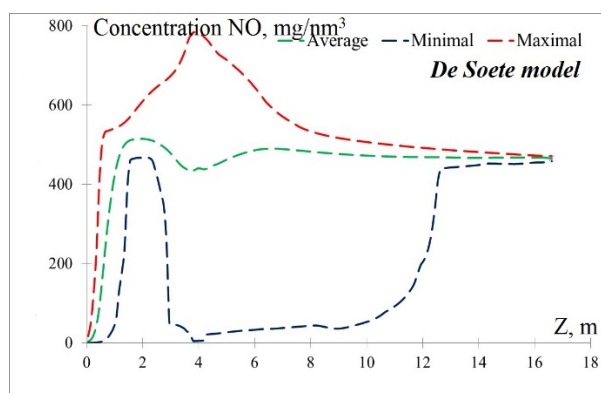


Fig. 5. Distribution of nitrogen oxides concentrations NO along the height of the combustion chamber of the BKZ-75 boiler for the NO_x formation model according to the De Soete model

An analysis of the graphs shows that the distribution curves of NO concentrations calculated using different models of their formation differ not only quantitatively, but also qualitatively. This is due to the fact that in the De Soete model, the calculation is made mainly in strict dependence on the oxygen concentration in the oxidizing medium. Also, the De Soete model is not sensitive enough to temperature changes at high temperatures, which affects the final results.

It can be seen that according to the Mitchell-Tarbell model, we have higher values of NO concentration compared to the De Soete model. So, at the outlet, the concentration of NO is equal to 606.14 mg/nm³ (Fig. 4) and equal to 467.6 mg/nm³ (Fig. 5). The difference in NO concentrations is significant and amounts to almost 23%.

The maximum concentrations of nitric oxide NO in the area of burners are associated with the oxidation of nitrogen N in the composition of the fuel (volume content 2.23%) and nitrogen N in the air (volume content ~ 77%), which enter here into the combustion chamber through the burners.

Figs. 6 and 7 show the results of three-dimensional distributions of nitric oxide NO concentrations in the furnace volume in the cross-section in the area of the burners: Z=3.98 m according to two models of NO_x formation (Mitchell-Tarbell and De Soete). From the analysis of the figures, it can be noted that the distribution of the concentration of nitric oxide NO in both models of NO_x formation for the selected section of the combustion chamber has a relative symmetry.

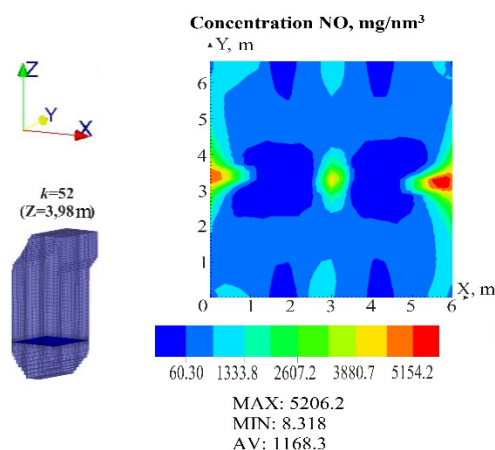


Fig. 6. Three-dimensional distribution of the concentration of nitrogen oxides NO in the cross-section ($Z = 3.98m$) of the combustion chamber of the BKZ-75 boiler for the NO_x formation model according to the Mitchell-Tarbell model

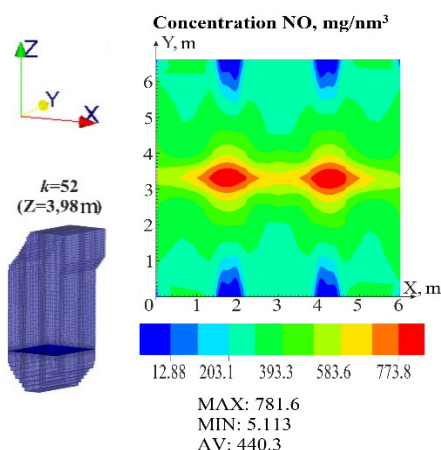


Fig. 7. Three-dimensional distribution of the concentration of nitrogen oxides NO in the cross section ($Z = 3.98\text{m}$) of the combustion chamber of the BKZ-75 boiler for the NO_x formation model according to the De Soete model

From the analysis of the distributions of the concentrations of nitrogen oxides NO in this section for both cases, it can be seen that they differ significantly (Figs. 6 and 7). The values of NO concentrations calculated according to the Mitchell-Tarbell model are higher everywhere in this section (average value is 1168 mg/nm^3) than the values of NO concentrations calculated according to the De Soete model (average value is 440 mg/nm^3).

The results of the distribution of NO concentrations calculated using the De Soete model (Fig. 7) are associated with a more idealized kinetic mechanism of this model, which is not sensitive enough to changes in temperature fields at high temperatures. As for the Mitchell-Tarbell model, it should be noted that it takes into account such factors as the size and composition of fuel particles, the degree of oxidation, changes in temperature fields, which, in turn, can have a significant impact on the processes of NO_x formation and distribution of NO concentrations in the sections of the combustion chamber.

A comparison of the results of the study using two models and field experimental data allows us to conclude that the Mitchell-Tarbell model is the most adequate describing model. From the analysis of the concentration fields of nitrogen oxides shown in Figs. 8 and 9, it can be noted that the results of calculating NO concentrations during computational experiments for the two models are significantly different.

From the distribution of the average concentrations of nitrogen oxide NO according to the results of the computational experiment, it was determined that the data of known field experiments are closer to the values obtained by the Mitchell-Tarbell model.

At the output, the average concentration of nitrogen oxide NO for the Mitchell-Tarbell model is 613 mg/nm^3 , for the De Soete model is 463 mg/nm^3 . At the same time, in the work, the experimental value (full-scale experiment at a thermal power plant) of the NO concentration at the output is 530 mg/nm^3 .

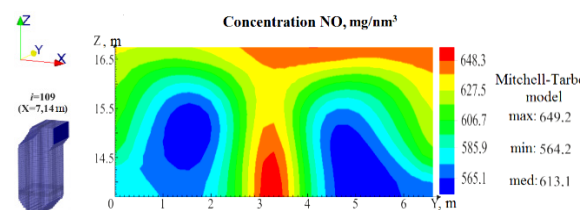


Fig. 8. Three-dimensional distribution of the concentration of nitrogen oxides NO in the longitudinal section at the outlet ($X = 7\text{ m}$) from the furnace chamber of the boiler BKZ-75 according to two models of NO_x formation

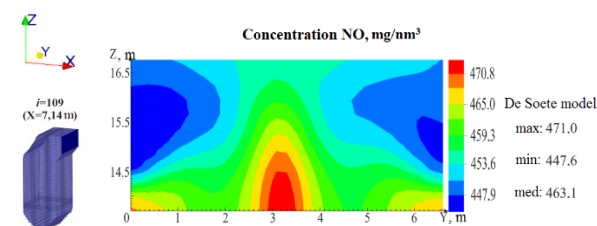


Fig. 9. Three-dimensional distribution of the concentration of nitrogen oxides NO in the longitudinal section at the outlet ($X = 7\text{ m}$) from the furnace chamber of the boiler BKZ-75 according to two models of NO_x formation

CONCLUSION

Based on the results of the work, the following conclusions can be drawn:

- Physico-chemical processes were studied during the combustion of high-ash energy fuel in the combustion chamber of an industrial energy facility, taking into account the main stages of coal combustion, the formation and destruction of harmful dust and gas emissions.
- A technique for 3D computer modeling of heat and mass transfer processes was developed, taking into account the kinetics of chemical reactions, multiphase and turbulent flow, nonlinear effects of thermal radiation during the movement of high temperature and chemically reacting flows in the combustion chambers of a thermal power plant.
- Physical, mathematical and chemical models of the problem were created that adequately describe the complex processes of physical and chemical transformations that occur during the combustion of high-ash Karaganda coal grade KR-200 in the combustion chamber of the BKZ-75-39FB boiler at Shaktinskaya CHPP.

• Computational experiments were carried out to study the concentration characteristics of the components in the combustion chamber BKZ-75-39 using two kinetic models of the formation of nitrogen oxides NO_x (Mitchell-Tarbell and De Soete). It was established that the choice of models affects the formation of NO concentration fields. So, at the outlet of the combustion chamber, the calculated value of the NO concentration according to the Mitchell-Tarbell model is 613 mg/nm³, and according to the De Soete model is 463 mg/nm³. Comparison with the experimental data obtained at the CHPP showed that the results of the numerical calculation of the concentration fields of NO according to the Mitchell-Tarbell model are closer to the results of a full-scale experiment and to the MPC values for coal-burning TPPs.

Thus, as a result of the conducted computational experiments, the high efficiency and adequacy of the Mitchell Tarbell kinetic model was noted in relation to the high-ash coal under study. This allows us to conclude that the use of the Mitchell Tarbell model to reproduce the process of burning low-grade coals is more preferable. The results obtained will help to realistically estimate the amount of nitrogen oxide emissions, as well as to design and implement various approaches to their minimization.

Acknowledgement: This work was funded by the Science Committee of the Ministry of Education and Science of the RK (Grant No. AP14870834, AP19679741).

REFERENCES

1. Coal ordered green energy to wait: dreams and reality diverged. EAD, <https://eadaily.com/ru/news/2021/12/17/ugolprikazal-zelenoy-energetike-podozhdad-mechty-i-realnost-razoshlis>; 2021 [accessed 08 November 2022].
2. World Energy Outlook, www.iea.org/weo.
3. G. Ni, et al. *Energy*, **261**, 125 (2022).
4. P. Rousse, R. Laubscher, *Energy*, **198**, 117 (2020).
5. B. M. Paredesa, J. P. Paredesa, R. García, *Energy*, **263**, 125 (2022).
6. P. Safarik, *Journal Acta Polytechnica*, **59**, 543 (2019).
7. M. Beketayeva, A. Georgiev, S. Bolegenova, et al., *Energy*, **258**, 124826 (2022).
8. E. Heierle, A. Ergaliev, S. Bolegenova, *Bulg. Chem. Commun.*, **48**, 260 (2016).
9. E. Karpenko, I. Loktionova. *J Thermal Engineering*, **51**, 488 (2004).
10. P. Safarik, N. Askarov, et al., *Chemical Engineering and Technology*, **44(11)**, 1970 (2021).
11. V. Messerle, V. Maximov, A. Nugymanova, et al., *Journal of Physics: Conference Series*, **1261**, 12 (2019).
12. Zh. Baizhuma, R. Manatbayev, A. Nugymanova, *Bulg. Chem. Commun.*, **50**, 53 (2018).
13. M. Beketayeva, S. Bolegenova, *IERI Procedia*, **10**, 252 (2014).
14. R. Leithner, S. Vockrodt, A. Schiller, *VDI Gesell. Energietechn.*, **1492**, 93 (1999).
15. S. Gil, Fuel-N conversion to NO, N₂O and N₂ during coal combustion, in: Fossil Fuel and the Environment, InTech, 2012.
16. S. C. Hill, L. D. Smoot, *Progress in Energy and Combustion Science* **26**, 417 (2000).
17. R. Leithner, M. Beketayeva, V. Maximov, *MATEC Web of Conf.*, **76** (2016).
18. M. Beketayeva, V. Maximov, *High Temperature*, **56**, 738 (2018).
19. A. Bekmuhamet, A. Askarova, S. Bolegenova, et al. *Procedia Engineering*, **42**, 1150 (2012).
20. P. Safarik, A. Nugymanova, V. Maximov, *Acta Polytechnica*, **59**, 98 (2019).
21. Zh. Shortanbayeva, S. Bolegenova, *Bulg. Chem. Commun.*, **48**, 229 (2016).
22. Zh. Shortanbayeva, A. Askarova, *4th Intern. Conf. on Math. and Comp. in Sciences and in Industry (MCSI 2017), Corfu Island, Greece*, 92 (2017).
23. A. Aldiyarova, A. Boranbayeva, *Bulg. Chem. Commun.* **48**, 272 (2016).
24. V. Messerle, A. O. Nugymanova, et al. *Thermophysics and Aeromechanics*, **28(2)**, 271 (2021).
25. S. Bolegenova, V. Maximov, *Intern. Journal Mechanics*, **10**, 320 (2016).
26. V. Maximov, M. Beketayeva, *Thermophysics and Aeromechanics*, **26**, 295 (2019).

Carbon materials used as additives to active mass of semi-traction lead-acid batteries

R. Płowens¹, M. Baraniak^{2*}, K. Lota³, J. Baraniak⁴, M. Bajsert¹, G. Lota^{2,3}

¹Jenox Akumulatory Sp. z o.o. Notecka 33,64-800 Chodzież, Poland

²Poznan University of Technology, Institute of Chemistry and Technical Electrochemistry, Berdychowo 4, 60-965 Poznan, Poland

³Lukasiewicz Research Network Institute of Non-Ferrous Metals Division in Poznan Central Laboratory of Batteries and Cells, Forteczna 12, 61-362 Poznan, Poland

⁴Institute of Natural Fibres and Medicinal Plants National Research Institute Department of Pharmacology and Phytochemistry, Kolejowa 2, 62-064 Plewiska, Poland

Received: April, 15, 2023; Accepted: February 19, 2024

The continuous increase of power consumption, together with the pressure to reduce greenhouse gas emissions, requires the generation of more and more electricity from renewable energy sources (RES). However, this implies other consequences. The electrical grid is an example. In this case, there are not only fluctuations in daily and seasonal levels of power consumption, but also fluctuations in power production. This is particularly related to energy obtained from photovoltaic panels and wind turbines. Energy storage systems (ESS) are a method to temporarily store energy as a buffer for sudden changes of electricity consumption or production. Energy storage methods are based on various technologies. One of the most important, especially for small systems, is based on chemical power sources. In this field, one of the most popular chemical power sources is the Pb/PbO₂ cells system, and especially its variants known as semi-traction and stationary batteries. Despite their disadvantages, lead-acid batteries are inexpensive, easily recycled and offer acceptable performance. Extensive research is being conducted to improve their electrical properties. The present research focuses on the effect of additives of different carbon materials to the electroactive mass on the properties of semi-traction lead-acid batteries such as formation process, capacitance, charge acceptance and cycle life.

Keywords: Semi-traction lead-acid battery, carbon additives, energy storage

INTRODUCTION

In the small system of renewable energy source (RES) installations, wind and solar energy are the most popular, while electrochemical batteries, such as lead-acid batteries [LAB], metal hydride [Ni-MH] batteries, or lithium-ion [Li-ion] batteries, are the most often used for energy storage. Lithium-ion batteries have the highest specific power, but their big disadvantage is their price and difficulty in recycling [1-3]. Lead-acid batteries are characterized by lower specific energy (~25-50 Wh kg⁻¹), energy density (~60-70 Wh dm⁻³), but the low production cost (~50-600 \$ kWh⁻¹) [4, 5] and the possibility of full recycling make them an interesting alternative, especially in small renewable energy installations. Semi-traction and stationary LAB are the most commonly ones used for this type of application [6-8]. The average new LAB contains about 80% of recycled material [9, 10]. The global production volume of lead-acid batteries is reported to have quadrupled between 1990 and 2020. Currently, more than 50% of the market share in terms of power demand is met by the lead-acid battery industry [11]. Although effective recycling programs for LAB have been developed, the main disadvantages

include low energy-to-weight ratio and low endurance under high-rate partial state of charge (HRPSoC) [12-15]. Therefore, research is constantly being conducted to improve the performance of LAB cells. This research involves many elements, such as grid alloy, active mass additives, electrolyte additives, etc. [13-17].

One of the most common undesirable processes occurring in Pb/PbO₂ cells, resulting in their faster failure, is sulfation. The growth of the coarse-grained crystalline layer may occur on both electrodes, and in particular on the negative electrode during the high-rate partial state of charge (HRPSoC) operation. Slowly over time, sulfation becomes permanent as some crystals expand and resist dissolution [18, 19]. Conversion of PbSO₄ to Pb or PbO₂ is inefficient with standard charging methods. To increase the use of negative active mass (NAM), mixtures of lignin, barium sulfate and carbon, known as expanders, are added to the production of negative plates [20]. Lignosulfonate is incorporated into the NAM to increase cycle life, prevent passivation and improve active mass utilization [21-23]. Barium sulfate (BaSO₄) is a nucleating agent (nucleant) for the formation and

* To whom all correspondence should be sent:
E-mail: marek.baraniak@put.poznan.pl

growth of small PbSO_4 crystals. In addition, it facilitates the distribution of these crystals on the surface of the pores of the active mass. This property of BaSO_4 is based on the isomorphism between lead and barium sulfate crystals [24]. Carbon materials are added to the paste mainly to improve the electrical conductivity of the active mass at the end of the discharge, when the content of PbSO_4 crystals in NAM significantly increases [25-27]. The addition of carbon improves strength, and increases the surface area, which can contribute to an increase in energy density [28]. It also facilitates the crystallization of fine PbSO_4 crystals over the entire plate surface by promoting electrochemical reactions [29].

The present research focuses on the effect of carbon material additives to the negative electroactive mass (NAM) on the electrochemical properties of semi-traction lead-acid batteries. Two types of graphite, one type of carbon black (commercially available) and carbon material obtained from flax fibers after carbonization were used in the study.

EXPERIMENTAL

Commercially available graphites included: expanded natural graphite (Superior Graphite abbreviation - SG), synthetic graphite (Cybrid 1 Imerys - CG), carbon black (SuperP Imerys - CB). Carbon material (CF) was obtained during carbonization of natural flax fibers. Conditions for carbonization of plant material were: time: 2h, $T = 700^\circ\text{C}$, gas: N_2 . Capacitance measurements of the selected carbon materials were carried out on electrode material which contained 85% tested carbons, 10% binder polytetrafluoroethylene (Sigma–Aldrich) and 5% acetylene carbon black (Super C65, Imerys). Electrodes were prepared in the form of pellets (12 mm in diameter). The carbon composite electrodes were used to prepare symmetric electrochemical capacitors (ECs) in Swagelok[®] cell systems with 316 L stainless steel current collectors. The electrolyte was 1 M H_2SO_4 , potential range 0.000-0.800 V in a two-electrode system, scan rate 5 mV/s. Tests were carried out at ambient temperature with a VMP3 potentiostat/galvanostat (Biologic, France) and results were analysed using EC-Lab[®] software. The specific conductivity of carbon materials was measured at a pressure of 40 bar, on a Carlo De Giorgi S.R.L. hand press in a cylindrical vessel. NAM was based on lead powder produced in a ball mill with a composition of about 75% PbO and 25% Pb . This powder was mixed with a standard expander used for SLI batteries (standard sample), which contains 0.3 wt%

carbon black, 0.3 wt% sodium lignosulfonates and 1.0 wt% BaSO_4 . The modified masses were enriched in carbon materials in the amount of 0.5 wt% (or 0.2% of CF). The smaller addition of CF was due to the observed viscosity difficulties during pasting. In addition, a mixture of graphite CG and carbon black CB in a mass ratio of 4:1 was also used. The addition of the mixture to the active mass was also 0.5 wt%. Other technological operations (including the process of curing and formation) were carried out in accordance with the technology of the Jenox company. 2V cells and 12V batteries were produced. The 2V cells were thermostated at 45°C during the formation process. The cells contained standard positive electrodes. Negative electrodes for 2V cells were handmade pasted. The open circuit voltages (OCV) and internal resistance (IR) of the cells were measured using a HIOKI BT-3554 (Japan) battery tester. Electrical tests of model cells were performed using a Digatron UBT - 50-18-10 tester (Germany). Electrochemical tests of Pb/PbO_2 systems were carried out with the use of VMP-III BioLogic potentiostat/galvanostat (BioLogic, France) with current booster and EC-Lab v. 11.10 software. SEM images were obtained using the scanning electron microscope Quanta 250 FEG, FEI ThermoFisher scientific device with energy dispersive spectroscopy module.

RESULTS

Research of pure carbon materials

The morphology and microstructure of carbon graphite are shown in Figs. 1 and 2.

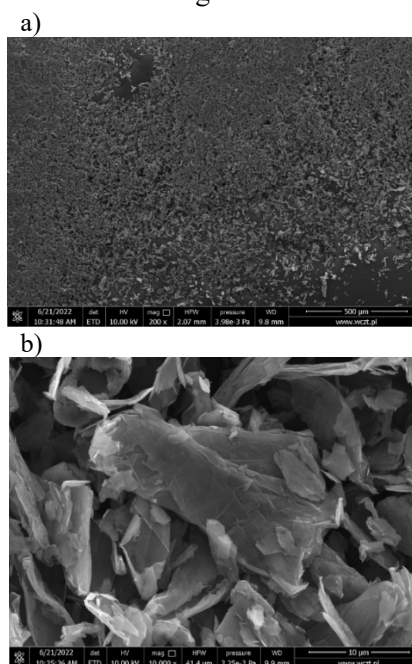


Fig. 1. Morphology (a) and microstructure (b) of graphite SG.

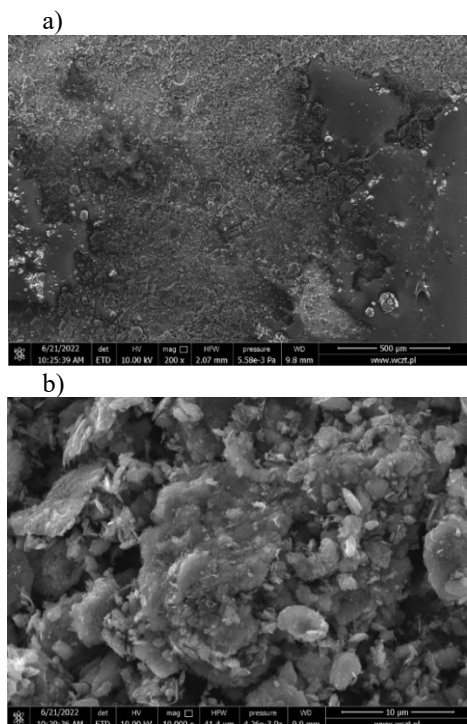


Fig. 2. Morphology (a) and microstructure (b) of graphite CG.

The morphology and microstructure of the carbon black and carbon material obtained from the flax fibers are shown in Figs. 3 and 4, respectively.

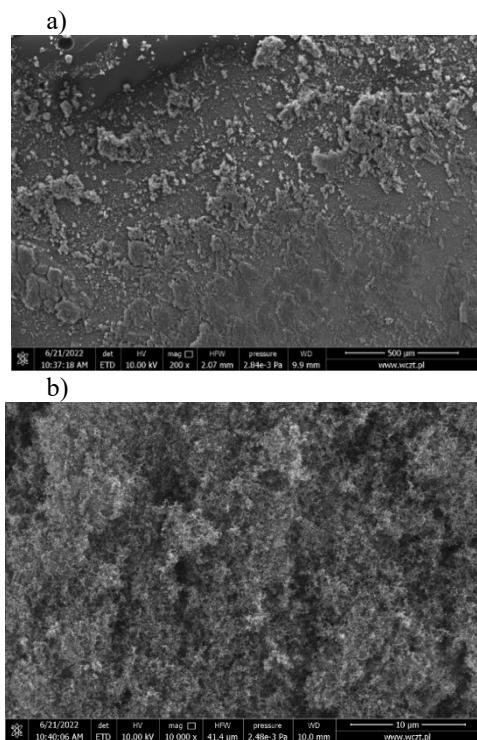


Fig. 3. Morphology (a) and microstructure (b) of carbon black CB.

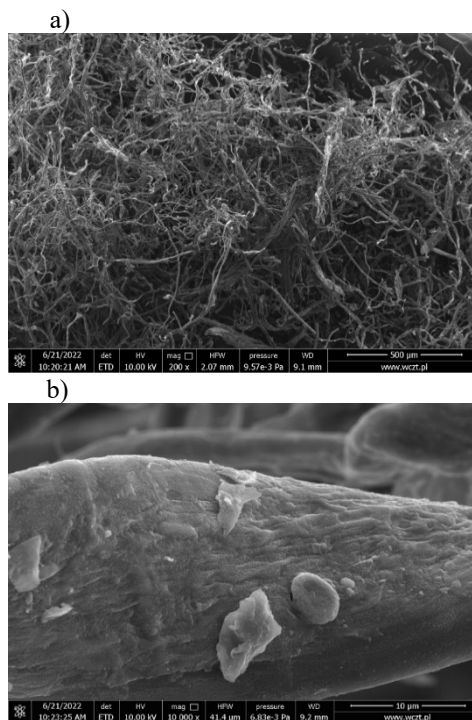


Fig. 4. Morphology (a) and microstructure (b) of carbon materials CF.

From Figs. 1-4, it can be noted that there are significant differences in the morphology and microstructure of the analysed carbon materials. These differences are observed even for both types of graphite used in the research. The specific conductivity (under pressure of 40 bar) and capacitance of the double layer of the tested carbon materials are shown in Fig. 5 and Table 1.

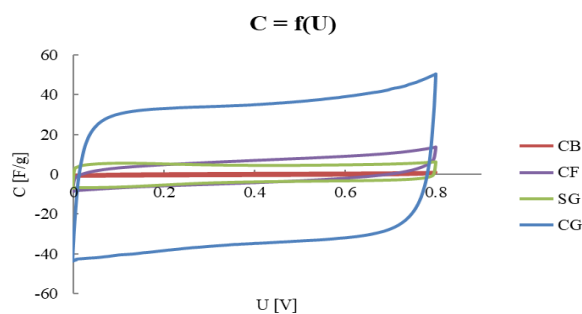


Fig. 5. Cyclic voltammety of tested carbon materials.

Table 1. Capacitance and specific conductivity of carbon materials.

	Capacitance	Conductivity
	F/g	S/cm
SG	4.5	4.1
CG	33.8	3.3
CB	<1.0	3.5
CF	5.2	0.2

As expected, each of the carbon materials exhibited significantly different electrochemical properties. The capacitance of the double layer of CF material was unexpectedly high. For CB material, on the other hand, it was very low. It should be also noted that the conductivity of the CF material was very poor.

2V cell testing

The 2V cells were assembled from two positive plates and one negative plate. The intended capacitance of the cell was 8 Ah. The soaking time with sulfuric acid was 30 min. The formation program is shown in Table 2.

Table 2. 2 V cell formation program

Step	Time	Current
	h	A
1	0.5	0.2
2	0.5	1.0
3	0.5	2.2
4	6.0	3.5
5	1.5	2.8
6	2.0	2.2
7	2.0	1.5

The overall time of the formation process was 13 h, and the total charge delivered to the cells was equal to 34.3 Ah. After the formation process, the plates containing only CB additive exhibited degradation of the active mass (Fig. 6) and therefore subsequent tests were carried out on active masses containing CG+CB additive in the ratio of 4:1.



Fig. 6. Negative plate with CB additive after formation process.

Table 3 presents the first three C₂₀ capacities of the tested cells. It can be noted that the NAM with CF material required 3 charge/discharge cycles to achieve a capacitance similar to the other cells. The highest C₂₀ capacities were obtained for cells containing NAM with the addition of CG and CG+CB.

Table 3. C₂₀ capacities for 2V cells (three charge/discharge cycles)

Additive	Electrical capacitance C ₂₀		
	I	II	III
	Ah	Ah	Ah
Standard	7.94	7.73	7.83
SG	7.62	7.48	7.60
CG	7.88	7.95	7.95
CG+CB	7.99	7.91	7.83
CF	3.43	5.99	7.80

Fig. 7 presents the relative values of the cells' internal resistance obtained in the charged condition (cell containing NAM without additives=100%).

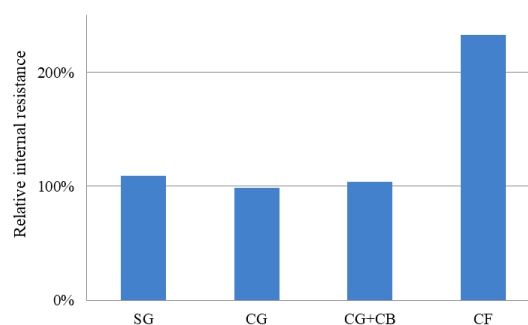


Fig. 7. Relative internal resistance of the cells (100%-cell containing NAM without additives)

The internal resistance of the cells containing carbon compounds was similar to that of the reference sample. The significantly higher resistance of the electrode with added CF material may be indicative of decrease of active mass cohesion or resistance at the grid/active mass interface. The higher resistance can also be explained by the fact that the negative active mass consists of pure lead, and any addition to the electrode can be considered as an element that increases resistance. The conductivity of pure carbon CF-type material was about 5-6% of that of SG and CG graphites. Graphite-based carbon materials, on the other hand, exhibited relatively good conductivity for a non-metallic material and as an additive to NAM did not affect the internal resistance of the negative electrodes.

Based on the experimental data from stages one and two, it was decided to focus on SG, CG and CG+CB material additives in further studies.

12V battery tests

The last stage of the research was to make 6-cell batteries with a theoretical capacitance of 45 Ah. At this stage, the tests included the determination of the discharge capacitance with currents from C₂₀

($I=2.25A$) to 3C ($I=135A$) (Fig. 8) and the endurance in cycle test according to EN 50342-1:2015 standard.

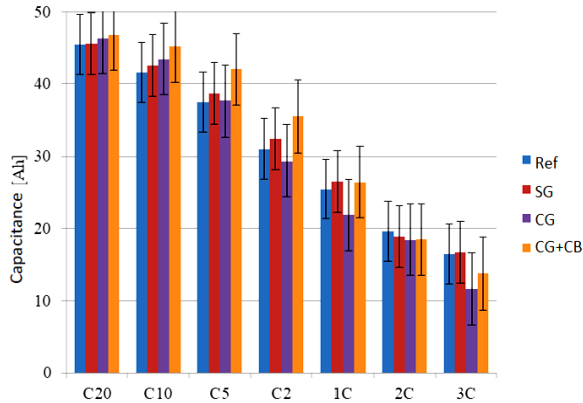


Fig. 8. Battery capacities for different discharge currents.

Based on the discharge times of the different currents, all the batteries exhibited similar electrical characteristics. However, LAB with modified NAM demonstrated modestly better properties up to a value of 1C (45A). Among them, only plates with CG had lower discharge characteristics over a wide range of currents.

The dependence of the discharge times for different currents (Equation 1) allowed to determine the Peukert coefficient (Table 4). Peukert coefficient (k) expresses the approximate change in capacitance of LAB at different discharge rates:

$$C = I^k t \quad (1)$$

where:

- C - capacitance, Ah;
- I - discharge current, A;
- t - discharge time, h.

Table 4. Peukert coefficients

k	

Standard	1.246
SG	1.250
CG	1.317
CG+CB	1.293

Based on Equation (1), it can be concluded that the lower the Peukert coefficient, the higher is the available capacitance during high current discharge. Standard and SG batteries showed the lowest Peukert coefficients. However, high-power discharges are rare in semi-traction systems.

A more important factor is the endurance of the system for operation in charging/discharging (CH/DCH) mode. Cyclic life test included endurance cycles. At first, fully charged batteries were discharged for 2 h with

a current of 11.25 A, next charged at $U_{con} = 15.6$ V, total charge $Q=1.08$ (108% of discharge capacitance) and again discharge. The CH/DCH cycle was repeated until voltage during discharge fell below 10.5 V. Fig. 9 presents the results of cyclic life test in relation to the standard battery.

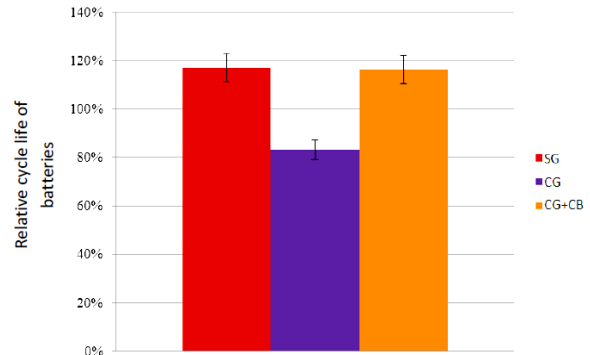


Fig. 9. Relative cycle life of batteries (100% - cell containing NAM without additives)

Batteries with NAM and SG or CG + CB demonstrated the highest cyclic resistance. The improvement in cyclic resistance was 17% and 16%, respectively, relative to the reference cell. In contrast, cells with the addition of CG had an approximately 18% lower durability cycle life test result.

CONCLUSIONS

Due to the practically unlimited number of types of carbon material precursors and modifications of the conditions for obtaining these materials, it is possible to constantly search for new additives to active masses. Based on presented experiments, it can be concluded that mixtures of carbon materials with different physicochemical properties are a very promising area of research. Studies of the physicochemical and electrochemical properties of pure carbon materials do not allow to predict their effect on the performance properties of plates in the battery. The 2+1 plate Pb/PbO₂ single-cell systems are more useful in the preliminary estimation of the electrochemical properties of modified electrode materials and their selection. However, owing to the complex relationships between the active mass (PAM, NAM) and the electrolyte, as well as thermal phenomena, it is necessary to verify the obtained data on multi-cell and multi-plate systems.

Acknowledgement: This work was supported by the Polish Ministry of Education and Science. The authors would also like to thank JENOX for providing samples.

NOMENCLATURE

LAB – lead-acid battery;
PAM – positive active mass;
NAM – negative active mass;
RES – renewable energy sources;
OCV – open circuit voltage [V];
IR – internal resistance [$m\Omega$].

REFERENCES

- G. J. May, A. Davidson, B. Monahov, *J. Energy Storage*, **15**, 145 (2018).
- Etacheri, R. Marom, R. Elazari, G. Salitra, D. Aurbach, *Energy Environ. Sci.*, **4**, 3243 (2011).
- R. D. Prengaman, A. H. Mirza, in: *Lead-acid Batteries for Future Automobiles*, Elsevier, Amsterdam, 2017.
- X. Luo, J. Wang, M. Dooner, J. Clarek, *Applied Energy*, **137**, 511 (2015).
- E. Schoch, M. Königsmann, J. Kizler, C. Schmucker, B. Kronenberg, M. Bremmer, J. Schottle, M. Ruch, in: *Lead-acid Batteries for Future Automobiles*, Elsevier, Amsterdam, 2017.
- L. T. Lam, R. Louey, *J. of Power Sources*, **158**, 1140 (2006)
- A. I. Stan, M. Swierczynski, D. I. Stroe, R. Teodorescu, S. J. Andreasen, K. Moth, INTELEC, Int. Telecommun. Energy Conf., Vancouver, 2014.
- M. Perrin, Y. M. Saint-Drenan, F. Mattera, P. Malbranche, *J. Power Sources*, **144**, 402 (2005).
- A. J. Davidson, S. P. Binks, J. Gediga, *Int. J. Life Cycle Assess.*, **21**, 1624 (2016).
- J. Garche, P. T. Moseley, E. Karden, in: *Advances in battery technologies for electric vehicles*, Cambridge, 2015, p. 75.
- Ch. Pillot, F. Renard, ELBC, The Global Battery Innovation Conf., Lyon, France, 2022.
- W.-L. Zhang, J. Yin, Z.-Q. Lin, J. Shi, C. Wang, D.-B. Liu et al., *J. of Power Sources*, **342**, 183 (2017).
- J. Shi, N. Lin, Y. Wang, D. Liu, H. Lin, *J. Energy Storage*, **30**, 101392 (2020).
- J. Yin, N. Lin, Z. Lin, Y. Wang, C. Chen, J. Shi et al., *Energy*, **193**, 116675 (2020).
- J. Yin, N. Lin, Z.-Q. Lin, Y. Wang, J. Shi, J.-P. Bao, et al., *J. Energy Storage*, **24**, 100756 (2019).
- K. Kopczyński, A. Gabryelczyk, M. Baraniak, B. Legosz, J. Pernak, P. Kędzior, G. Lota, *Int. J. Electrochem. Sci.*, **13**, (11) 11058 (2018).
- K. Kopczyński, A. Gabryelczyk, M. Baraniak, B. Legosz, J. Pernak, E. Jankowska, W. Rzeszutek, P. Kędzior, G. Lota, *J. Energy Storage*, **2**, 100996-1-100996-10 (2019).
- D. Pavlov, P. Nikolov, *J. Electrochem. Soc.* **159**, 1215 (2012).
- P. T. Moseley, D. A. J. Rand, A. Davidson, B. Monahov, *J. Energy Storage*, **19**, 272 (2018).
- D. Pavlov, in: *Lead-Acid Batteries: Science and Technology*, Elsevier, Amsterdam, 2nd edn., 2017.
- D. von Borstel, G. Hoogestraat, W. Ziechmann, *J. of Power Sources*, **50**, 131 (1994).
- B. O. Myrvold, *J. of Applied Electrochemistry*, **35**, 573 (2005).
- K. Sawai, T. Funato, M. Watanabe, H. Wada, K. Nakamura, M. Shiomi, S. Osumi, *J. of Power Sources*, **158**, 1084 (2006).
- R. Marom, B. Ziv, A. Banerjee, B. Cahana, S. Luski, D. Aurbach, *J. of Power Sources*, **296**, 78 (2015).
- X. Zou, Z. Kang, D. Shu, Y. Liao, Y. Gong, C. He, J. Hao, Y. Zhong, *Electrochimica Acta*, **151**, 89 (2015).
- J. Lach, K. Wróbel, J. Wróbel, P. Podsadni, A. Czerwiński, *J. of Solid State Electrochemistry*, **23**, 693 (2019).
- P. T. Moseley, R. F. Nelson, A. F. Hollenkamp, *J. of Power Sources*, **157**, 3 (2006).
- K. Yanamandra, D. Pinisetty, N. Gupta, *Renewable and Sustainable Energy Reviews*, **173**, 113078, (2023).
- P. T. Moseley, D. A. J. Rand, K. Peters, *J. of Power Sources*, **295**, 268 (2015).

Selected papers presented on the seminar Sustainable Processes and Systems in Chemical and Biochemical Technologies - SPSCbBT-2023, 30th November, 2023, Sofia, Bulgaria

Horizontal expanded metal sheet packing (Holpack) for mass and heat transfer processes in column apparatuses – study of research, mathematical modeling and industrial application

K. Semkov, R. Darakchiev, T. Petrova*, S. Darakchiev

*Institute of Chemical Engineering, Bulgarian Academy of Sciences,
Acad. G. Bonchev Str., Bl. 103, 1113 Sofia, Bulgaria*

Revised: February 12, 2024

The horizontal expanded metal sheet packing is designed and investigated for carrying out mass and heat transfer processes in column apparatuses. The packing is made of expanded metal sheets, placed horizontally on certain distance from one another along the column height. This construction creates conditions for highly effective heat and mass transfer at comparatively low gas pressure drop. This packing has low specific weight and specific effective packing surface area, significantly larger than its specific geometric one.

The present study article is an overview of the most important results regarding the development and investigation of the packing giving all necessary information for its application. The packing is studied in detail; mathematical models and dimensioning methodology of apparatuses are provided and tested. As a result, the packing was successfully implemented in many processes in the chemical and power industry, as well as in the environmental protection. On this base analysis is made and opportunities for its further improvement are discussed. The configuration of the sheets could be improved in order to intensify the mass and heat transfer processes without increasing the pressure drop.

Keywords: Horizontal expanded metal sheet packing, Holpack packing, Packed columns, Pressure drop, Mass transfer, Direct contact heat transfer, Process intensification

INTRODUCTION

The horizontal metal sheet packing is a physical realization of the patented method for performing of mass transfer processes [1]. It is made of expanded metal sheets, placed horizontally on a certain distance along the column height. The sheets are produced on a die by shearing with specially formed knives and subsequent sheet extension, whereupon staggered openings with inclined walls are formed. This product is standardized and is applied for many purposes; if made by thicker metal sheet it usually is used for production of stairs and platforms on different equipments. At first the packing was known as “Horizontal sheet packing”, but later for the sake of convenience it was called “Holpack”.

The investigations carried out confirmed its very good hydrodynamic and mass transfer characteristics. The favorable indicators of Holpack packing made it tempting to use in a large number of technological processes where it found industrial application,

The aim of this study article is to present the most important performance characteristics of the packing, mathematical models and dimensioning methodology, as well as the industrial application in various mass and heat transfer processes. Most of the characteristics are compared to those of some

modern highly effective packings. For the industrial design of the apparatuses different models are used depending on the process specific conditions, e.g., the piston flow (plug-flow) model [2] and the dispersion model [3-5].

The results of the research and the experience of the implementation of many years created preconditions for improvement of the packing towards further intensification of processes and equipment. The possible ways of such improvement are also commented.

PRINCIPLES OF THE PACKING DESIGN, MAIN GEOMETRIC AND HYDRODYNAMIC DIMENSIONS

Amongst the known heat and mass transfer apparatuses the hollow irrigated scrubbers are distinguished by the lowest, near to zero pressure drop. However, they are low-effective because of the non-uniform distribution of the gas across the apparatus cross-section and the low values of the mass transfer coefficients. This is due to the absence of elements/structures in which the liquid phase to be hit and turbulized while interchanging its phase surface. A comparison between the hollow irrigated scrubbers and packed columns shows that the latter avoid the disadvantages of the hollow scrubbers at the expense of a significant increase of the apparatus

* To whom all correspondence should be sent:

E-mail: t.petrova@iche.bas.bg

pressure drop. Consequently, the development of a hybrid apparatus combining a high mass transfer coefficient and uniform gas velocity distribution in the column with a pressure drop close to that of the hollow irrigated scrubbers appears to be an attractive task.

One convenient solution of this task is replacing the packing by horizontal perforated sheets with large free section, situated horizontally at a distance between them of a few centimeters [1, 6]. The additional pressure drop of the sheets improves the radial uniformity of the gas flow velocity profile. At the same time, the hit of the liquid upon the sheets contributes to the liquid phase turbulization and surface renewal [3, 7-9]. The contradiction between the need of large free section for low gas pressure drop and possibly larger sheet surface, where the irrigating liquid to be hit, can be solved through appropriate sheet profile and packing geometry optimization. Particularly suitable for design of such packing is the material known as “expanded metal sheet” (Figure 1). A good presentation of the technology of its production is given in [10]. It is prevalent for building of factory platforms and stairs, as well as some plate columns constructions. As a very popular manufacturing article it is standardized (e.g., GOST 8706-78). The high productivity of the machines for expanded metal sheets production, the lack of waste of material (like many new metal packings) and the significant (up to 75 %) lengthening of the sheets during its processing to expanded metal sheet determine its low cost. The expanded metal sheets are also used to produce some corrugated structured packings, e.g., Montz packing type BSH [11], Rib mesh packing type BSH [12].

An essential advantage of this type of sheets is the flow directing action of the inclined lamellae forming the slits. They orientate the gas at an angle towards the sheet cross-section contributing to its radial redistribution. This slope also leads to an increased liquid spreading which is favorable for the simplification of the commonly used multipoint liquid distributors. To avoid the one-sided direction of the liquid by the lamellae forming each sheet, the sheets are arranged one above another by rotating at 90° in the same direction – the so called “crosswise” arrangement. Thus, at every fourth sheet the orientation of the lamellae is the same. The distance between the sheets is kept by vertical distancing strips. For comparison, another configuration called “opposite” arrangement rotating the sheets at 180° was also investigated but has not found industrial application due to its lower efficiency. So created packing is mounted in column sections as illustrated by a top-view photograph in Figure 2.

The most important hydrodynamic dimensions of the packing can be determined from its geometric sizes using the following equations (see Figure 1):

$$d_h = \frac{s(B+4A)}{8X+B} \quad a = \frac{8X(s_l/2+\delta)+B(s_l+\delta)}{BC(h_1+h_2)} \quad (1)$$

$$\varepsilon_l = 1 - \frac{2\delta(B/4+2X)}{BC}$$

where the subsidiary parameter X is determined as follows:

$$X = \frac{1}{2} \sqrt{s^2 + \left(A - \frac{B}{4}\right)^2} \quad (1-a)$$

For comparison with other packings the Holpack void fraction (free packing volume) can be determined:

$$\varepsilon = \frac{\varepsilon_l h_1 + h_2}{h_1 + h_2} \quad (1-b)$$

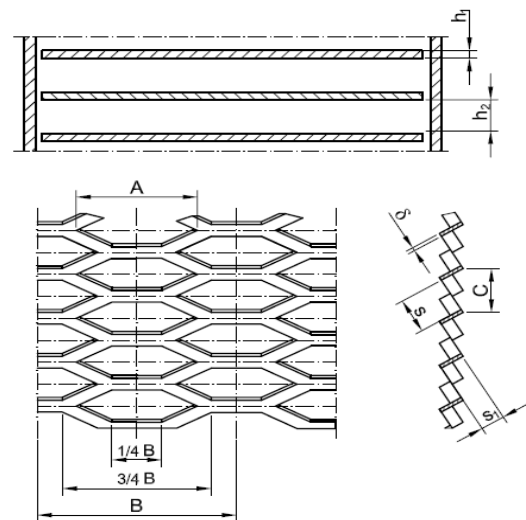


Fig. 1. Packing sheet made of expanded section from metal sheet with main dimensions



Fig. 2. Photograph of a column with Holpack packing

According to this parameter (for example, from Table 1), for the packing No. 6 with one of the lowest

sheet free cross-section $\varepsilon_1 = 0.80$ the void fraction is $\varepsilon = 0.974$ and for No. 26 with maximum $\varepsilon_1 = 0.96$ it is $\varepsilon = 0.985$. In both packings the distance between the sheets is equal ($h_2 = 20$ mm). Hence, the void fraction of the Holpack packing is very large (mainly due to the empty volume between the sheets) which is a good precondition for low pressure drop.

For implementing this packing into practice, a thorough research was needed to be accomplished with a view to the most appropriate cases for its use, as well as for collecting data and working out equations for determination of its main characteristics included in the corresponding mathematical models. Such are pressure drop, loading point, liquid hold-up, liquid and gas distribution across the column cross-section, effective specific surface area, axial mixing of the phases, and coefficients of mass transfer, controlled by gas and liquid boundary layer. Only such detailed investigations can be of use for dimensioning of

industrial equipment for every specific case. In this way the expedience of using the packing in each heat and mass transfer process at minimal expenses can be estimated.

For the results from the pilot study to be transferrable to industrial objects, the geometric dimensions of the investigated packings and the physicochemical properties of the flowing liquid must vary in a sufficiently wide range. Moreover, it is necessary to verify the influence of the column diameter on the results. On this basis, fundamental research of Holpack packing was carried out at the following limits of the geometric sizes (see Tables 1 to 3) and physical parameters of the liquid phase: L_0 - density of irrigation ($1.5 \times 10^{-3} \div 6.6 \times 10^{-2}$ m³/m².s); ρ_L - liquid density ($1000 \div 1230$ kg/m³), ν_L - liquid kinematic viscosity ($4.0 \times 10^{-7} \div 1.5 \times 10^{-6}$ m²/s). As gas phase air was used. The main characteristics and symbols of the investigated packings are given in Tables 1-3. Further, all symbols which differ, will be noted in the figures themselves.

Table 1. Main characteristics of Holpack packings, used at the research of pressure drop and the mass transfer coefficients, as well as implemented at industrial applications

No.	Sym- bol	<i>A</i> mm	<i>B</i> mm	<i>C</i> mm	δ mm	<i>s</i> mm	<i>s</i> ₁ mm	<i>h</i> ₁ mm	<i>h</i> ₂ mm	<i>d</i> _h mm	ε_1 %	<i>a</i> m ² /m ³	<i>D</i> _c mm
1	○	22.2	30.7	6.4	0.8	5.0	4.0	3.0	5	6.5	81.3	202	190
2	●	22.2	30.7	6.4	0.8	5.0	4.0	3.0	10	6.5	81.3	125	190
3	△	22.2	30.7	6.4	0.8	5.0	4.0	3.0	20	6.5	81.3	70.0	190
4	▲	22.2	30.7	6.4	0.8	5.0	4.0	3.0	40	6.5	81.3	38.0	190
5	×	22.2	30.7	6.4	0.8	5.0	4.0	3.0	20	6.5	81.3	70.0	470
6	⊙	22.2	30.7	6.4	0.8	5.0	4.0	3.0	20	6.5	80.0	70.0	190
7	⊖	22.2	30.7	6.4	0.8	5.0	4.0	3.0	20	6.5	80.0	70.0	190
8	◐	22.2	30.7	6.4	0.8	5.0	4.0	3.0	20	6.5	80.0	70.0	190
9	⊕	22.2	30.7	6.4	0.8	5.0	4.0	3.0	20	6.5	80.0	70.0	190
10	◑	22.2	30.7	6.4	0.8	5.0	4.0	3.0	20	6.5	80.0	70.0	190
11	◒	22.2	30.7	6.4	0.8	5.0	4.0	3.0	20	6.5	80.0	70.0	190
12	●	22.2	30.7	6.4	0.8	5.0	4.0	3.0	40	6.5	80.0	38.0	190
13	□	22.2	30.7	6.4	0.8	5.0	4.0	3.0	40	6.5	81.3	38.0	190
14	◇	22.2	30.7	6.4	0.8	5.0	4.0	3.0	10	6.5	81.3	125	190
15	⊕	22.2	42.7	7.7	1.0	4.5	6.2	4.6	20	6.5	86.0	63.0	190
16	▽	85.0	114	36.0	4.0	16.0	24.0	17.5	0	20.8	83.0	96.7	470
17	■	85.0	114	36.0	4.0	16.0	24.0	17.5	10	20.8	83.0	61.6	470
18	▼	85.0	114	36.0	4.0	16.0	24.0	17.5	50	20.8	83.0	25.1	470
19	⊕	90.0	121	27.0	1.5	13.0	16.5	13.2	15	17.0	91.6	49.5	190
20	⊕	90.0	121	27.0	1.5	13.0	16.5	13.2	50	17.0	91.6	22.0	470
21		22.2	30.7	6.4	0.8	5.0	4.0	3.0	50	6.5	81.3	31.0	470
22		90.0	122	23.8	3.0	13.0	13.0	11.0	50	17.0	81.0	24.0	470
23		82.0	109	28.0	1.0	18.3	18.3	14.3	20	23.5	95.0	42.0	800
24		72.0	124	18.5	1.5	15.0	15.0	13.0	50	21.0	90.2	25.0	400, 800, 1200
25		19.0	27.0	7.7	0.6	5.3	4.2	3.5	20	6.8	88.4	56.0	207
26		92.0	120	32.0	0.8	20.0	20.0	13.2	20	25.6	96.0	41.6	207-800

For packings Nos. 1-4 – the packing sheets are rotated at 180° to one another. Nos. 6 – 12 – the sheets are covered with polyethylene. Nos. 7 – 11 – the irrigation density varies from 1120 to 1230 kg/m³ and dynamic viscosity from 2.6×10^{-3} to 15×10^{-3} Pa.s.

MATHEMATICAL MODELS AND PARAMETERS

Gas flow pressure drop and loading point

The experimental investigations of the pressure drop of Holpack was carried out [6, 13, 14] mostly in an air–water system. The following packings were tested (Table 1): Nos. 1÷4, 13, 15, 17 and 20. To estimate the influence of liquid phase viscosity some experiments were also carried out with irrigation by an aqueous solution of sugar [6, 13, 14].

Figure 3 depicts the typical dependence of the pressure drop for Holpack No. 4.

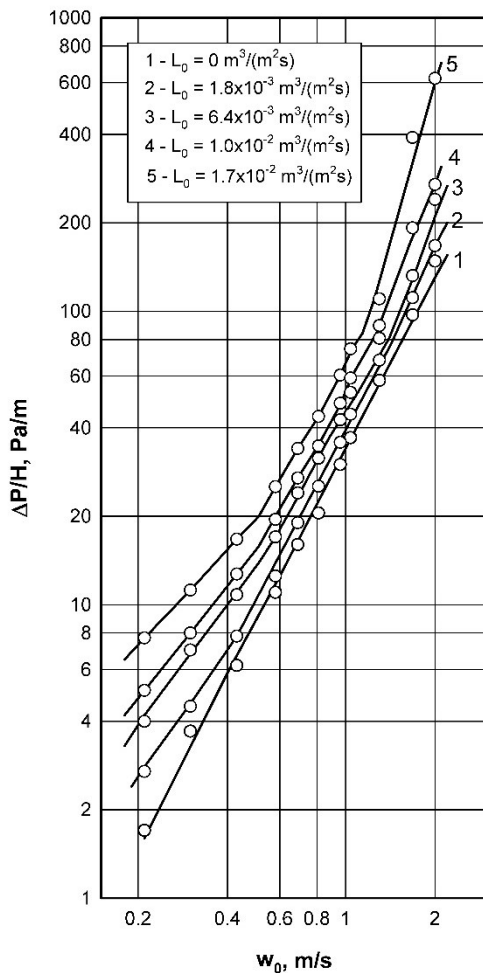


Fig. 3. Pressure drop of packing Holpack No. 4 (Table 1) depending on the gas velocity

Analogous dependencies are observed for the other investigated packings. The obtained experimental data are compared with the pressure drop of metal structured packings Montz B1-250, Mellapak 250 X, Mellapak 250 Y and Sulzer BX [15-19]. Closest to their dry packing pressure drop is the packing No. 20 (Table 1). The comparison of the wet packings Montz B1-250 and Mellapak 250 X [16-18] with packing No. 20 shows about two times lower pressure drop of Holpack at similar

conditions. In the same works, the earlier models and equations for determination of the pressure drop of dry and irrigated Holpack packing, as well as for loading point gas velocity were also proposed. Subsequently, after a careful critical analysis on the base of many years' practical (incl. industrial) experience some imperfection of these dependences and, respectively, opportunities for substantial improvement were found. As a result, new more accurate models and equations for determination of gas pressure drop characteristics were developed [20].

It should be underlined that in the new equations the same experimental data are used as in the old ones. The principal differences evolve from the new structure of the equations, proposed striving to be closer to the real physical phenomena typical of the gas pressure drop in tubes and channels [20]. In this way, using the dimensional analysis, a more realistic estimation of the influence of the geometric dimensions (mainly the packing sheet free cross-section) can be made. For example, this parameter appears in the new structure only as a part/term of the dimensionless numbers, not as a separate one. Further, in the new derived equations the packings Nos. 1÷4 were excluded because of their "opposite" arrangement. As will be shown later, this arrangement has about 14% less effective specific area of the irrigated packing than the "crosswise" arrangement at equal conditions and didn't find practical application due to lower efficiency.

The new equations, presented below, were derived using dimensional analysis and least-square approach regression. Here the equation form reflects the flow pressure drop in tubes and channels. The *Euler* number (*Eu*) is defined as a ratio between the static pressure drop of the packing and the dynamic pressure (see Eq. 5). The main difference from the old equation is that the free cross-section of the packing sheet (ε_1) is not involved as a main dimensionless variable. After each equation the main statistic parameters as the mean arithmetic error (MAE) (absolute value) and the standard deviation (SD) are given.

- Pressure drop of dry Holpack packing (ΔP_0)

$$Eu = \left(0.0343 + \frac{2.16}{Re_G} \right) N_1 \left(\frac{H}{d_h} \right) \left(\frac{h_l}{d_h} \right)^{2.47} Re_G^{0.112};$$

$$MAE = 7.88\%; SD = 12.6\% \quad (2)$$

- Pressure drop of irrigated Holpack packing (ΔP)

$$\frac{\Delta P}{\Delta P_0} = 0.884 Re_L^{0.17} \left(\frac{s_1}{d_h} \right)^{-0.25} Re_G^{0.054}; \quad (3)$$

MAE = 5.5%; SD = 8.6%

➤ Loading point gas velocity (w_{0G})

$$MFr_G = 1.97 \left(\frac{s_1}{d_h} \right)^{-0.90} Fr_L^{-0.112}; \quad (4)$$

MAE = 4.56%; SD = 7.67%,

where the dimensionless numbers are defined as:

$$Eu = \frac{2\Delta P_0 \varepsilon_1^2}{w_0^2 \rho_G} \quad Re_G = \frac{w_0 d_h}{\nu_G \varepsilon_1} \quad Re_L = \frac{L_0 d_h}{\varepsilon_1 \nu_L} \quad (5)$$

$$Fr_L = \frac{L_0^2}{g d_h \varepsilon_1^2}; \quad MFr_G = \sqrt{\frac{w_{0G}^2}{\varepsilon_1^2 d_h g} \left(\frac{\rho_G}{\rho_A} \right)}$$

Here the *Euler* number (Eu) reflects the ratio between the static pressure drop of the packing and the dynamic pressure. It should be pointed out again that ε_1 is the packing sheet free cross-section and is not equal to the packing void fraction \mathcal{E} (see Eq. 1b).

Dynamic liquid hold-up

The liquid hold-up of the packing is a sum of static and dynamic hold-up. Because of the construction of Holpack packing its static hold-up can be neglected. The research of the dynamic hold-up of Holpack packing [14, 21] is carried out using packings with diverse characteristics (Table 1). The irrigation density is varied between 1.5×10^{-3} and $1.7 \times 10^{-2} \text{ m}^3/(\text{m}^2\text{s})$. The whole research is done without gas flow because it is known that up to the loading point, packing hold-up does not depend on the gas velocity. Liquid viscosity is changed within the limits from 1.0×10^{-3} to $1.3 \times 10^{-2} \text{ Pa}\cdot\text{s}$ and the density – from 1000 to 1230 kg/m^3 . The results are shown in Figure 4 as a dependence on the water irrigation density.

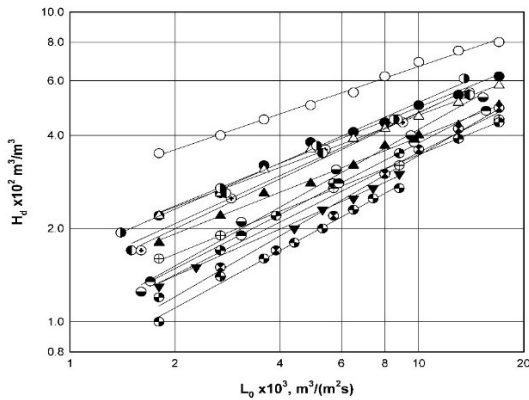


Fig. 4. Experimental data for the hold-up of Holpack packing (Table 1), depending on the irrigation density

For determination of the dynamic hold-up of Holpack packing (below the loading point) the following equation is derived [14, 21]:

$$H_d = 0.47 Ga_L^{-0.05} Fr_L^{0.22}, \quad (6)$$

where the numbers of *Galilei* and *Froude* are defined by the expressions:

$$Ga_L = \frac{g}{a^3 \nu_L^2}; \quad Fr_L = \frac{L_0 a}{g}. \quad (7)$$

The deviation between the experimental data and Equation (6) is within $\pm 20\%$.

A careful consideration of Figure 4 shows very low values of the liquid hold-up of Holpack packing, which is due to its construction. It should be noted that this is a very good characteristic with a view to its industrial application, which makes the technological apparatuses with this packing quite flexible at variation of the operating regimes.

It can be said that liquid hold-up values for Holpack (Table 1) are approximately between 1 to 4 % for a very wide range of liquid rates. Compared to modern structured packing like Mellapak 2X, Flexipac 2Y HC, B1-250M and Mellapak 250 X, Holpack liquid hold-up values are lower or equal to the values of liquid hold-up for structured packings [16, 21]. In [21] the values of liquid hold-up have been determined for 3 different systems: air/water, air/sugar/water $5 \times 10^{-3} \text{ Pa}\cdot\text{s}$ and air/sugar/water $12 \times 10^{-3} \text{ Pa}\cdot\text{s}$. In [16] liquid hold-up values are obtained for air /water and air/MEA 30 % wt systems.

Liquid distribution

The uniform radial liquid distribution is a crucial condition for the normal operation of packed columns. For this purpose, uniform initial liquid distributions at the top of the packing layer, as well as its maintenance along the column height must be provided.

For the initial distribution in the industrial columns normally multipoint distributing devices are used. Then the distribution uniformity in the upper zone of the packing depends on the design of the distributing device (mainly the distance between the jet points) and the redistribution (spread) ability of the packing. The latter is expressed by the liquid radial spreading coefficient D_r . This coefficient is usually experimentally determined by the method of Kabakov and Dilman [22]. This method is still in use both for random and structured packing to obtain information about spreading coefficient [16, 23].

Table 2. Geometric dimensions of the investigated Holpack packings for determination of their liquid spreading coefficient and its experimental values

No	Sym- bol	A mm	B mm	C mm	δ mm	s mm	s_1 mm	h_1 mm	h_2 mm	d_h mm	a m ² /m ³	D_r mm
1	○	22.2	30.7	6.4	0.8	5.0	4.0	3.0	10	6.5	125	1.0
2	●	22.2	30.7	6.4	0.8	5.0	4.0	3.0	20	6.5	70.0	1.0
3	◐	22.2	30.7	6.4	0.8	5.0	4.0	3.0	50	6.5	31.0	1.0
4	△	90.0	122	23.8	3.0	13.0	13.0	11.0	10	17.0	70.0	1.8
5	▲	90.0	122	23.8	3.0	13.0	13.0	11.0	20	17.0	47.4	1.8
6	◀	90.0	122	23.8	3.0	13.0	13.0	11.0	50	17.0	23.8	1.5
7	▽	85.0	114	36.0	4.0	16.0	24.0	17.5	10	20.8	61.6	5.7
8	▼	85.0	114	36.0	4.0	16.0	24.0	17.5	20	20.8	45.2	5.7
9	◃	85.0	114	36.0	4.0	16.0	24.0	17.5	50	20.8	25.1	3.5

The investigations for the spreading coefficient of Holpack packing are carried out at spreading a single jet [24]. The device used for this purpose is a cylindrical section with a diameter of 470 mm in which the liquid is fed axially at the top of the packing. The packing layer height is varied from 100 to 370 mm depending on its type. In all cases a “crosswise” arrangement of the packing is used.

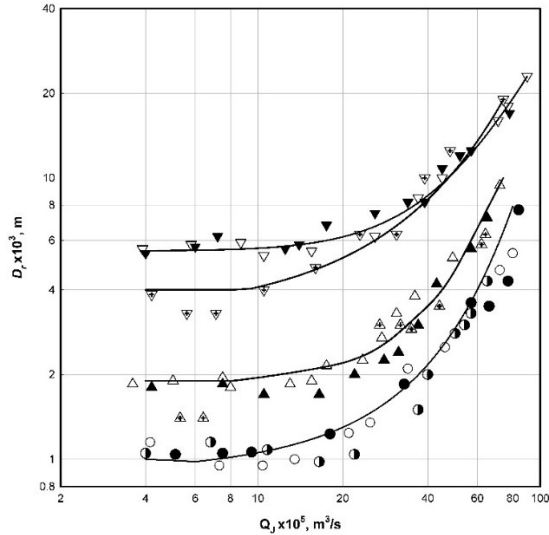


Fig. 5. Dependence of the distribution coefficient of different types of Holpack packing (Table 2) from the flow rate of a single jet.

The liquid, spread in the packing, is collected below the packing in concentrically situated cylinders, which also serves as a supporting grid. The value of D_r is determined by the above-mentioned methodology [22]. The obtained results are presented in Figure 5. The characteristics of the investigated packings and their symbols are given in Table 2.

Figure 5 shows that at a flow rate of the single jet of about $1.4 \times 10^{-4} \text{ m}^3/\text{s}$, the coefficient D_r does not change, while raising the flow rate above this value leads to its increase. The experiments also show that

at a distance between the packing sheets of 10 and 20 mm, the values of the radial spreading coefficient are close to one another. Data at a distance of 50 mm lie lower in the area of the smaller flow rates. At increasing the flow rate of the single jet, the values of the coefficient come closer. Considering the perceived methodology [22], the values of the radial spreading coefficient are determined only at the horizontal section of the dependency on Fig. 5.

Applying the dimensional analysis to the data for all investigated packings in the area, where the flow rate of the single jet does not affect the distribution, the following equation is obtained [24]:

$$\frac{D_r}{s_1} = 27 \left(\frac{h_1}{s_1} \right)^{2.9} \left(\frac{h_1 + h_2}{s_1} \right)^{-0.18} \left(\frac{\delta}{s_1} \right)^{2.2} \quad (8)$$

The mean arithmetic error (MAE) of Equation (8) is 11 % and the confidence interval at 95 % statistical safety is 5.8 %. The maximal error does not exceed 27 %.

Because of the low values of D_r , Holpack packings Nos. 1÷3 are not suitable for a redistribution layer. To determine the radial spreading coefficients of the packings Nos. 4-9 only the following modified equation is proposed [24]:

$$\frac{D_r}{s_1} = 0.133 \left(\frac{h_1}{s_1} \right)^{-2.0} \left(\frac{h_1 + h_2}{s_1} \right)^{-0.38} \quad (9)$$

The mean arithmetical error of Eq. (9) is 8.9 % and the maximal one does not exceed 20 %. The confidence interval at 95 % statistical safety is 5.6 % and at 90 % statistical safety is 4.7 %.

In Table 2 are given the values of the distribution coefficient for the investigated 9 Holpack packings. The higher values for packings Nos. 4÷9 make them rather promising to be used as a redistribution layer above packings with low distribution ability. Additional warranty for this is provided by the higher admissible velocities for them. These values are comparable or a little higher than the

corresponding value for Mellapak 250 X (between 3 and 4 mm, depending on the investigated liquid phase) [16]. The difference in specific surface between Holpack and Mellapak 250 X has to be noted. Higher values of the distribution coefficient D_r lead to lower requirements to the liquid distributors used in columns with Holpack packing. Conditions are created for using more simple design of distributing devices with a smaller number of distributing points per unit of cross-section of the apparatus. The higher spreading ability of this packing combined with the tendency of the liquid in such columns to spread towards the wall, lead to a strengthening of the wall effect [2, 14, 25, 26]. This causes a variation of the gas-liquid ratio along the apparatus cross section and particularly in the wall zone. The liquid there less actively participates in the mass transfer process than in the bulk of the column. Thus, the wall layer appears to be a bypass to a great extent, which significantly decreases the column effectiveness as a whole. Holpack packing construction itself creates conditions for increasing this effect. The sheets usually do not stick tightly to the column wall because of construction tolerance and because of tolerance related to the ellipticity of the column case. This leads to pouring more liquid on the wall from the peripheral elements of the sheet, than they take away and send back to the bulk of the packing. This way a bigger wall flow is formed.

To limit or eliminate the detrimental influence of the wall flow the so-called Wall Flow Deflecting Rings (WFDR) are proposed [25]. They are narrow (about 5 – 25 mm) rings with a profile suitable to deflect the wall flow (Fig. 6), which are situated at a distance of 100 – 300 mm from one another on the internal side of the column. Version (a) is better for pilot investigations at a column diameter up to 200 mm. For industrial apparatuses the exemplary variants (b) and (c) are more suitable because of the simpler implementation.

For determination of the influence of WFDR at Holpack packing, an experimental study is carried out with 4 packing types Nos. 5, 13, 19 and 20 from Table 1 in a column with a diameter of 190 mm [26] and deflecting rings with a width of 5 mm. As a model process/system the desorption of CO₂ from water in air flow is used. The amount of the liquid flowed in the wall zone, as well as the mass transfer in the liquid boundary layer in the wall zone and in the bulk of the packing at the end of the column is investigated. The influence of the distance between the deflecting rings along the apparatus height on these results is also examined [14].

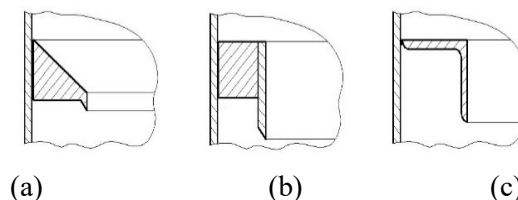


Fig. 6. Sketch of wall flow deflecting rings (WFDR)

Figure 7 shows the influence of the irrigation density on the height of transfer unit (HTU), the wall zone and in the bulk of the packing. For this purpose, special liquid collecting cells for both zones were used. The obtained results [26] show that at density of irrigation from 2×10^{-3} to 1×10^{-2} m³/(m²s), i.e., in the area important for the industrial practice, HTU in the wall zone is between 40 and 80 % bigger than HTU in the bulk of the packing. The data using WFDR are also shown. It can be seen that at a distance between them of 200 mm, HTU in the wall zone is practically equal to that in the bulk zone.

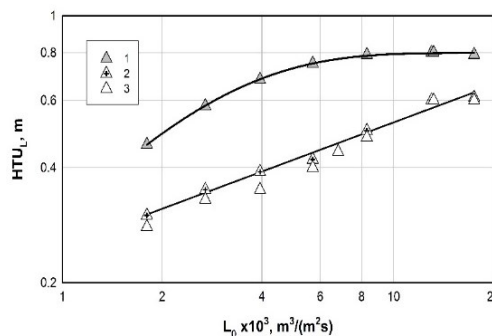


Fig. 7. Influence of the irrigation density on the height of a transfer unit for packing Holpack No. 2 (Table 2). 1 – at the wall zone without WFDR; 2 – at the wall zone with WFDR at a distance of 200 mm; 3 – in the bulk of the packing.

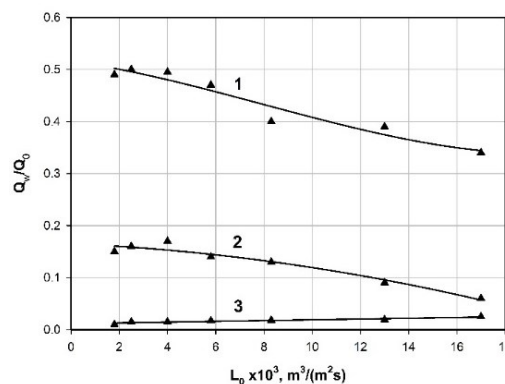


Fig. 8. Influence of the irrigation density on the distribution of the liquid to the wall of the apparatus at different distances between the WFDR. 1 – without rings; 2 and 3 – distance between the rings of 200 and 100 mm.

The results [26] of the study of the flowing of the liquid towards the column wall with and without WFDR are shown on Fig. 8. Almost fully averting of

this flowing is observed at a distance of 100 mm between the rings. The experience at the further application of WFDR shows that they successfully eliminate the wall flow in larger-scale, including industrial apparatuses. The width of the rings should be bigger than the width of the actual slot/gap between the end of the packing sheet and the wall of the apparatus. The rings used in the practice are within 10 and 25 mm wide.

Gas distribution

The uniform distribution of the gas velocity across the packed columns cross-section is an important condition for their normal operation. Non-uniformity conditions for local irregularity of the gas-liquid ratio are created, resulting in decreasing of the actual average concentration difference in the apparatus and thus in lowering of the effectiveness of the mass and heat transfer process.

One of the main sources for unequal gas distribution is its introduction in the apparatus. The equalizing action of the packing is caused by its resistance distributed on the cross-section of the column. It makes the flow to redistribute on the front but at the same time to move through the openings of the packing elements. Holpack packing is actually a system of consecutively situated grids of expanded metal sheet. Owing to the gradual flow from one grid to another at comparatively low values of the resistance coefficient, a fast uniform distribution of the velocity across the cross section is reached. The significant mixing of the gas phase in radial direction in volume between the sheets is essential in this process.

The study of Darakchiev [27] aims to determine the minimal packing height, at which a uniform gas distribution on the column cross section with sufficient accuracy for the practice can be assumed. The experiments are carried out with several types of random packings, plastic Pall rings 50 mm and ceramic saddles Intalox 35 mm among them. Four types of Holpack packings are investigated (packings Nos. 1, 3, 7 and 9 from Table 2), as well as packing No. 1 from Table 1 without distance between the sheets, for comparison. The diameter of the experimental column is 470 mm without irrigating liquid. The air flow velocity is measured with a thermo anemometer. The sensitive element of the device (the probe) is attached to a stand with a possibility for a movement along two perpendicular diameters of the column cross section. It is situated at a small distance from the upper end of the packing. Because of its high sensibility to turbulent pulsations and to increase the measurement accuracy, an averaging of the signal is done with analogue

computing machine.

An estimation of the degree of non-uniformity of the velocity distribution on the cross section is performed with regard to the maximal flow velocity related to the average velocity on the cross section (w_{\max}/w_0). In this research the equalization of the velocity profile is accepted at a maldistribution degree of 1.25.

The expanded metal sheets of the investigated Holpack packings have a big free section (over 80 %). The experiments show that at initial maldistribution reaching 2 (200 %) (see Fig. 9), the number of the sheets needed to reach the wanted degree of maldistribution (equalization of the velocity profile) is 5–12 (Fig. 10). The hydraulic diameter of the openings d_h , as well as the distance between the sheets h_2 , where the radial gas redistribution passes brings influence to bear on this. The determined heights for uniform distribution are: for packing No. 1 - 0.146 m; No. 3 - 0.268 m; No. 7 - 0.320 m and No. 9 - 0.355 m. The plastic Pall rings of 50 mm and ceramic saddles Intalox of 35 mm show equalization of the profile at a layer height of 0.8–1 m. The mean air velocity within the researched range from 1.1 to 2.5 m/s has no significant influence on the flow distribution. The research is also done at different initial maldistributions caused by different gas inlet devices in the column.

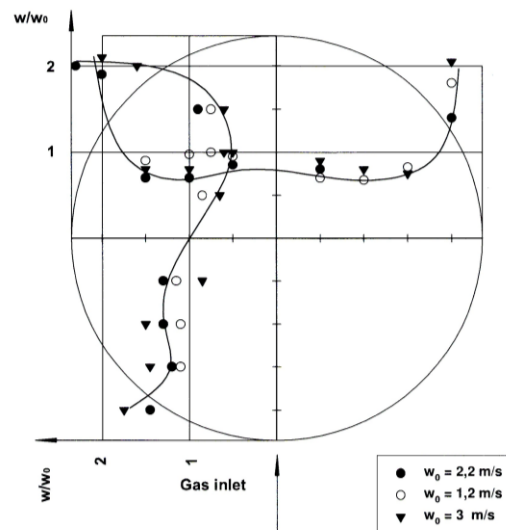


Fig. 9. Distribution of the ratio of local to mean gas velocity on the cross section of a column with a diameter of 470 mm on a distance of 100 mm below the packing grid by two mutually perpendicular directions.

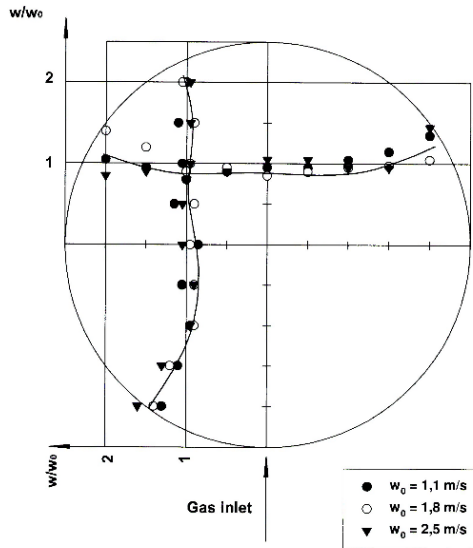


Fig. 10. Distribution of the ratio of local to mean gas velocity on the cross section of a column with a diameter of 470 mm for packing Holpack No. 21 (Table 1) with a height of 0.215 m.

In the presence of a counter-currently moving liquid up to the loading point (the area in which the heat and mass transfer packed apparatuses usually operate), the interaction between the phases can be neglected by definition and the picture would not significantly change. The flowing liquid will occupy a part of the cross section; it will reduce the void section of the packing and will increase the smoothing action of the packing layer. The gas distribution is also estimated by means of the maldistribution factor [28-30], using the same experimental data [30]:

$$M_f = \sqrt{\frac{1}{n} \sum_{i=1}^n \left(\frac{w_i - w_0}{w_0} \right)^2} \quad (10)$$

where: w_i is the local velocity of the gas in the i -th measuring cell, m/s and n is the number of measuring cells.

A very important index, which can be evaluated using this parameter, is the uniformity limit. It shows the minimal possible maldistribution for every packing type and results from its discrete structure. For packings with distance between the sheets of 10 and 50 mm, the uniformity limit is at maldistribution factor $M_f = 0.19$ and $M_f = 0.18$, at the lack of distance [29]. This shows that the distance between the packing sheets is very important for equalizing the gas velocity profile.

Effective surface area

Knowing the effective interphase area is a crucial moment in studying the mass- and heat transfer in packed columns. The research works for determination of the effective area of Holpack packing are carried out mainly by [2, 14, 31]. They are made by the method using a chemical reaction of pseudo-first order. As a model system the absorption of CO_2 from NaOH solution is used.

The obtained experimental data for the investigated packings (Table 1) are presented as a dependence between the specific effective interphase surface area and the density of irrigation (Fig. 11).

Processing the obtained experimental data for determination of the specific effective inter-phase area of Holpack packing the following equation is obtained [14, 31]:

$$\frac{a_e}{a} = C_1 E\ddot{o}^{0.28} Fr^{0.066}, \quad (11)$$

$$\text{for } E\ddot{o} = \frac{\rho_L g}{\sigma a^2} \text{ and } Fr = \frac{L_0^2 a}{g}$$

where $C_1 = 0.95$ for crossed sheet arrangement and $C_1 = 0.82$ for opposite arrangement.

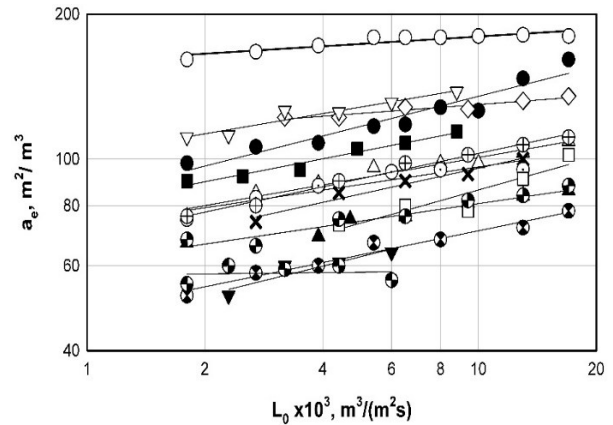


Fig. 11. Dependence of the effective specific surface area of Holpack packing (Table 1) on the irrigation density.

The comparison shows that 93 % of the experimental data have a maximum deviation of ± 15 % from the values computed by Eq. (11) Because of the higher specific effective area at crossed sheet arrangement at equal geometric characteristics, this arrangement has been implemented into practice. The ratio between the effective and the specific geometric area for Holpack packing is of especial interest because of its design and principle of operation. The results [2] are shown on Fig. 12.

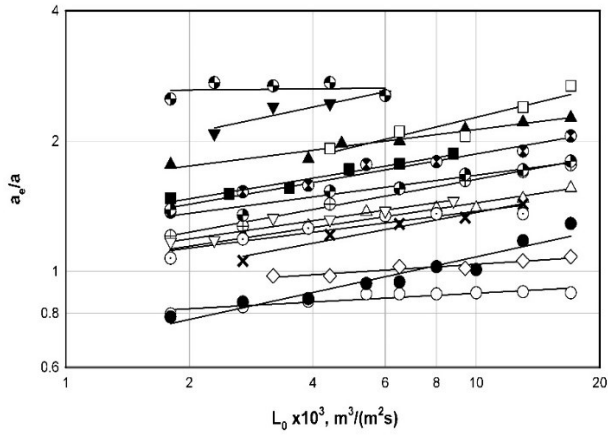


Fig. 12. Dependence of the ratio of the effective to the specific surface area of Holpack packing (Table 1) on the irrigation density.

There can be seen that for this packing, this ratio can reach 3, as the other values are between 1 and 3. This is due to the phase surface of the drops and jets in the empty spaces between the packing sheets. Such effect is also observed for random packings with an open structure and large free volume where the ratio between the effective and the geometric area does not exceed a value of 2 [32].

Axial mixing in the liquid phase

The axial mixing is a hydrodynamic phenomenon which decreases the driving force of the process and at definite conditions can significantly reduce the effectiveness of the packed column [5, 33]. The axial mixing is inevitable and at uniform radial distribution of the phases it reflects the possibly minimal small-scale maldistribution, which is due to the discrete structure of the packing. Particularly important is the influence of the axial mixing in the liquid phase at low irrigation densities, while in the gas phase the influence of the axial mixing is weak and for Holpack it is assumed to be insignificant [5, 34], mainly because of its design, which contributes for the equalization of gas velocities on the column cross-section. The influence of axial mixing is taken into account using the dispersion mathematical

Table 3. Geometric dimensions of Holpack packings, used for the research of the axial mixing in the liquid phase and for the first investigations at rectification.

No.	<i>A</i> mm	<i>B</i> mm	<i>C</i> mm	δ mm	<i>s</i> mm	<i>s_l</i> mm	<i>h₁</i> mm	<i>h₂</i> mm	<i>d_h</i> mm	<i>a</i> m ² /m ³	ε_1 %
1	21.2	29.2	9.3	1.0	6.3	4.6	3.9	50	8.0	24.9	83.4
2	21.2	29.2	9.3	1.0	6.3	4.6	3.9	25	8.0	46.5	83.4
3	21.2	29.2	9.3	1.0	6.3	4.6	3.9	9.3	8.0	102	83.4
4	73.8	114	21.6	3.0	15.4	12.0	11.5	50	20.6	22.7	81.4
5	73.8	114	21.6	3.0	15.4	12.0	11.5	25.1	20.6	38.2	81.4

model with hydrodynamic parameter the dimensionless number of Bodenstein. In this number the axial mixing is reflected by axial mixing coefficient as an analogue of the axial turbulent diffusion.

The axial mixing in the liquid phase in columns with Holpack packing is studied [33, 34] at irrigation with water and without air flow by the method using an electrolyte tracer that is fed above the packing as a δ -impulse. Both flows – water and tracer are uniformly distributed over the column cross-section. To increase the accuracy, the disturbing influence of the conductometric cell is additionally accounted for by the method described in [35]. Five types of packing are investigated (Table 3) in a column with a diameter of 190 mm over a wide range of variation of the irrigation densities from 3.0×10^{-4} to 1.5×10^{-2} m³/(m²s).

One peculiar feature of the axial mixing in the liquid phase is observed for Holpack packing that is due to the packing operating principle. Two regimes are identified [34] provisionally called “drop” and “jet” regimes, where the dependency of the axial mixing by the irrigation density differs significantly. For the “drop” regime is obtained the Equation:

$$Bo_L = 0.029(a h_1)^{0.43} Re_L^{0.39} (aH) \quad \text{for } Re_L < Re_{LCr}, \quad (12)$$

and for the “jet” one:

$$Bo_L = 1.62 \times 10^{-5} Ga_L^{0.81} (a h_1)^{0.31} Re_L^{-0.83} (aH) \quad \text{for } Re_L \geq Re_{LCr}. \quad (13)$$

The mean arithmetic error of Equation (12) is 9.3 % and that of Equation (13) is 16.2 %. The transition between both regimes is determined by the critical value of the Reynolds number, defined by the equation:

$$Re_{LCr} = 2.18 \times 10^{-3} Ga_L^{0.66} (a h_1)^{-0.096} \quad (14)$$

The criteria of Bodenstein, Reynolds and Galilei in Equations (12÷14) are defined as follows:

$$Bo_L = \frac{L_0 H}{\varepsilon_1 H_d D_{TL}}; \quad Re_L = \frac{4L_0}{a v_L}; \quad Ga_L = \frac{g}{a^3 v_L^2}$$

where D_{TL} is the axial mixing coefficient in the liquid phase.

The physical explanation for the existence of these regimes follows by the operating principle of the packing. At low loads the liquid flows down by drops consecutively from sheet to sheet through the packing. On increasing the irrigation density, the small-scale radial uniformity of the flowing drops improves and this leads to a lowering of the axial mixing and respectively increases the apparatus effectiveness. On further increase of the load jets are forming that flow with different velocity and the axial mixing becomes higher again.

From Equations (12÷14) it can be seen that at “drop” regime the Bodenstein number increases with increasing the irrigation density while at the “jet” regime (above the critical value of Reynolds number) the dependency is opposite. Since on increasing the values of Bodenstein number, the influence of the axial mixing goes down, it follows that for Holpack packing there is an optimal operating range with maximal effectiveness around the point of the transition between both the regimes. The comparison between the corresponding equations [5] for determination of Bodenstein number for Holpack packing and for conventional ceramic random packings shows that at equal specific surface area in drop regime (below Re_{LCr}) the coefficient of axial mixing in the liquid phase for Holpack is up to 4 times smaller.

In the study [36] the axial mixing in the liquid and gas phases of metal Pall rings 25, metal Intalox saddles 25 and Mellapak 250Y was investigated. For the liquid phase a similar tracer method was applied, but using stepwise tracer injection instead of δ -impulse and two conductometric sensors located on certain distance in order to improve the experimental accuracy. Equations for Bodenstein number of each type of packing were worked out. The comparison with Holpack, e.g., No. 5 from Table 3 in the optimal operation zone ($\sim Re_{LCr}$) shows that the coefficient of axial mixing for 1 m packing layer of Holpack packing is 10.8 times smaller than of Pall 25, 11.8 times than of Intalox 25 and 5.7 times than of Mellapak 250Y.

The above comparisons give a significant advantage to Holpack packing to carry out processes at the conditions of which the influence of the axial mixing in the liquid phase is high. In the jet regime

(above Re_{LCr}) the axial mixing coefficient can be bigger than that of the random packings but then as a rule the influence itself of the axial mixing on the mass transfer effectiveness in packed columns decreases because of the increase of the height of transfer unit (HTU_L) [33].

Mass transfer controlled by the gas boundary layer

The experiments for determination of mass transfer coefficients at a process controlled by the gas boundary layer are carried out in columns with diameters 190 and 470 mm [2, 37]. The process of absorption of ammonia with a concentration of 0.5÷1 % in pure water is used. Because of the high rate of the absorption process, the gas concentration at the end of the apparatus is quite low. To obtain the desired accuracy of the experimental research, the heights of the investigated packings are within the range of 0.5 ÷ 1 m. The smaller packing heights are related to packings with a small equivalent diameter and smaller distance between the sheets.

Figure 13 shows the dependency of the volumetric mass transfer coefficient for mass transfer controlled by the gas boundary layer on the gas velocity at irrigation densities of $3.3 \times 10^{-3} \text{ m}^3/(\text{m}^2\text{s})$ (for packings Nos. 1, 5, 18 and 20) and only $8 \times 10^{-3} \text{ m}^3/(\text{m}^2\text{s})$ is for packing No. 15 (Table 1). The experimental results are compared with these of the metal structured packing Mellapak 250 X with $a=205 \text{ m}^2/\text{m}^3$ [38]. The comparison is made with Holpack packing No. 20 at $w_0 = 1.5 \text{ m/s}$ and $L=3.9 \times 10^{-3} \text{ m}^3/(\text{m}^2\text{s})$. The coefficient of mass transfer controlled by the gas boundary layer is 2.2 times higher for Holpack packing at equal pressure drop. This coefficient is by 70 % higher for Holpack compared with Mellapak 250 Y at the same velocity and $L=1 \times 10^{-2} \text{ m}^3/(\text{m}^2\text{s})$. This shows its possibilities to be applied in absorption processes and direct heat transfer.

After processing all available data of the mass transfer coefficient at mass transfer controlled by the gas boundary layer for Holpack packing the following equation is obtained [37]:

$$Sh_G = 0.26 Re_G^{0.73} Sc_G^{0.33} \quad (15)$$

where the criteria of Sherwood, Reynolds, and Schmidt are defined by the expressions:

$$Sh_G = \frac{k_G d_h}{D_G}; \quad Re_G = \frac{w_0 d_h}{v_G}; \quad Sc_G = \frac{v_G}{D_G}$$

The comparison between the experimental data and the results from Equation (15), shows that 93 % of them have deviation less than 20 %.

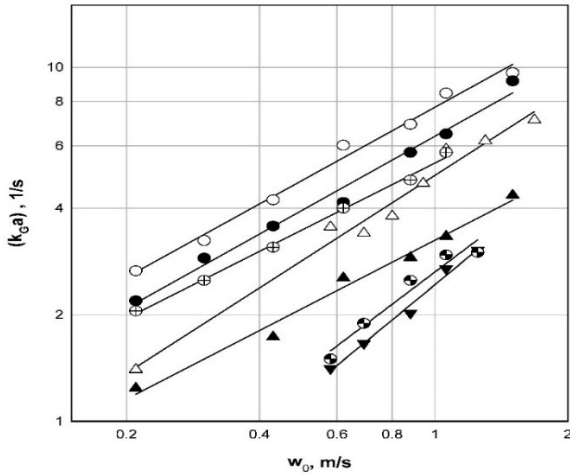


Fig. 13. Dependence of the overall mass transfer coefficient at mass transfer controlled by the gas boundary layer for Holpack packing (Table 1) at $L_0 = 3.9 \times 10^{-3} \text{ m}^3/(\text{m}^2\text{s})$ (for packing No.15 – $L_0 = 8.10^{-3} \text{ m}^3/(\text{m}^2\text{s})$).

Mass transfer controlled by the liquid boundary layer

- *Leaving out of account the axial mixing*

The determination of the mass transfer coefficient for a mass transfer controlled by the liquid boundary layer can be done by data for absorption (desorption) of weakly soluble gases. For Holpack packing research desorption of CO_2 from water solutions in an air flow is used. The experiments are carried out in two stands with diameters of the experimental columns of 190 and 470 mm. The height of the packing layer is within the range of $1 \div 2 \text{ m}$ and the air velocity is $0.5 \div 1 \text{ m/s}$ [2, 39].

The experimental data for the volumetric mass transfer coefficient for a mass transfer controlled by the liquid boundary layer as a function of the irrigation density of all of the investigated packings (Table 1) at 20°C and air velocity of 0.7 m/s are shown on Fig. 14. The obtained experimental results are compared with these of metal structured packings Mellapak 250 X and Mellapak 250 Y [40]. The comparison is made with packings Holpack No. 4 and No. 20 (Table 1) at $w_0 = 1.4 \text{ m/s}$ and $L = 3.4 \times 10^{-3} \text{ m}^3/(\text{m}^2\text{s})$. At a little lower pressure drop the mass transfer coefficients ($k_L a$) are practically equal.

After processing all of the available data for Holpack packing to determine the volumetric mass transfer coefficient for mass transfer controlled by the liquid boundary layer the following equation is obtained [39]:

$$Sh_L = 1.13 \times 10^{-3} Re_L^{0.635} Ga_L^{0.366} Sc_L^{0.5} (s_1/h_1)^{4.0} (ah_1)^{0.1} \quad (16)$$

where the criteria of Sherwood, Reynolds, Schmidt and Galilei are defined by the expressions:

$$Sh_L = \frac{k_L h_1}{D_L}; \quad Re_L = \frac{4L_0}{a_e v_L}; \quad Sc_L = \frac{\nu_L}{D_L}; \quad Ga_L = \frac{g h_1^3}{\nu_L^2}$$

The comparison between the experimental data with Equation (16) shows that the deviations do not exceed $\pm 20 \%$.

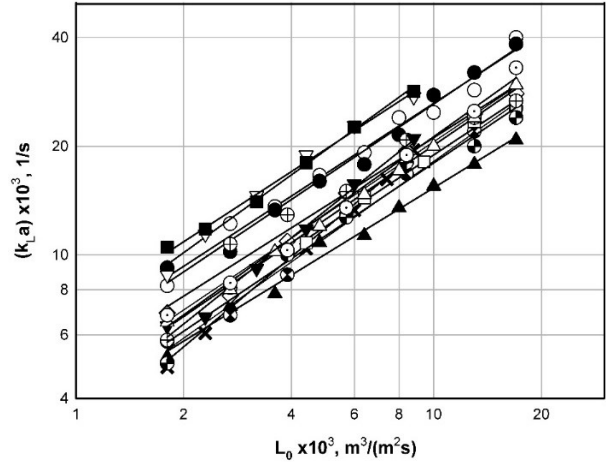


Fig. 14. Dependence of the overall mass transfer coefficient at mass transfer, controlled by the liquid boundary layer from the irrigation density for Holpack packing (Table 1) at $w_0 = 0.7 \text{ m/s}$.

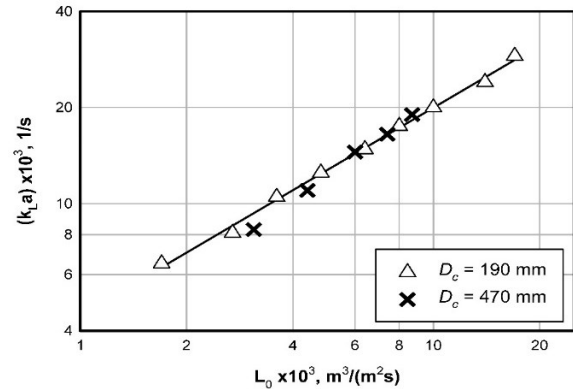


Fig. 15. Influence of the irrigation density on the overall mass transfer coefficient for two different diameters of the experimental column for packing No. 3 (Table 1).

On Figure 15 the experimental data [14] for the influence of the irrigation density on the overall mass transfer coefficient for packings No. 3 and No. 5 (Table 1) with equal geometric sizes, for two different diameters of the experimental column are presented. The good grouping of the points around only one line shows that at maintaining uniform irrigation, the column diameter does not affect the effectiveness of columns with Holpack packing. It should be noted that at processing the experimental data, the influence of the axial mixing for the conditions of the experiment is not considered and

because of that it is implied in Eq. (16). The equation itself can be used only in the plug flow model within the range of its accuracy and at conditions similar or in reasonable deviations from these, at which it is derived in terms of the axial mixing. How to weigh up this is shown further down.

- *Considering the axial mixing*

The mass transfer coefficients in the liquid boundary layer suitable for using in the dispersion model should not include the influence of the axial mixing because it is taken into account in the model through the hydrodynamic parameter – Bodenstein number. The values of such mass transfer coefficients can be determined by experimental data at a process, controlled by the liquid boundary layer and consequent elimination of the axial mixing influence for the specific experimental conditions. Essentially this represents identification of the mass transfer coefficient in the dispersion model k_L^0 at degree of separation obtained from the plug flow model with mass transfer coefficient k_L at the same packing height and irrigation density. For this purpose, a method and a procedure are developed that are firstly applied for different types of random packings [33, 35]. Similarly, are processed all of the experimental data for the mass transfer coefficient for a process controlled by the liquid boundary layer for the Holpack packings from Table 1, used for working out Equation (16). The Bodenstein numbers are determined by Equations (12-14). The obtained results for the mass transfer coefficients, satisfying the dispersion model are generalized in the following equation [4, 5, 33]:

$$Sh_L^0 = 4.88 \times 10^{-3} Re_L^{0.49} Ga_L^{0.40} Sc_L^{0.5} (ah_1)^{-0.074} \quad (17)$$

where the Sherwood number is $Sh_L^0 = \frac{k_L^0 h_1}{D_L}$,

and the other criteria are defined as in Eq. (16). The mean arithmetic error of Eq. (17) is 11 %.

It is interesting to note that as a result of taking into account the axial mixing the exponent of Reynolds number in Equation (17) is considerably (with 25 %) smaller than that in Equation (16), e.g., the role of the most important hydrodynamic factor – the irrigation density, declines. This proceeds from the fact that the influence of the irrigation density is partly accounted for in the axial mixing. The simplex (s_1/h_1) loses its significance in Eq. (17). This simplex characterizes the angle of the inclination of the expanded metal sheet lamellae and it is related to the direct falling of the liquid through the packing sheet. The mixing caused by this outstripping forms a part of the axial mixing and is taken into account

by the dispersion model. However, the influence of s_1 remains with its participation in the effective specific surface area – Eq. (11) and the specific area – Eq. (1).

The importance of the mass transfer coefficient determination taking into account the axial mixing is shown in the study [41] as well. For this purpose, an alternative approach is proposed, the so called “profile method”. This consists in the identification of the mass transfer coefficient on the base of the best fitting from concentration experimental data using the dispersion model and Bodenstein number equations. Experimental data from distillation in pilot plant with Mellapak 250 Y and Intalox 25 saddles were processed. It is highlighted that the dispersion model reproduces the concentration profiles better than the plug flow model.

- *Influence of the axial mixing*

To illustrate the influence of the axial mixing in the liquid phase for Holpack packing and the adequacy of its accounting for by the dispersion model and the plug flow model a comparison of the mass transfer coefficients satisfying the relevant models is made. The results are obtained with a numerical experiment and are presented on Fig. 16 in percent relative deviation between the coefficients as a function of the irrigation density [4]. The accomplished calculations show that from the packing geometric characteristics, the specific surface area has the most significant influence and because of that it is given as a parameter on the figure. The range from 20 to 100 m²/m³ is covered, which corresponds to the packings used in practice. The investigated interval of irrigation densities is 2×10⁻⁴ – 6×10⁻² m³/(m²s), which is the whole range interesting for the practice. The packing height is assumed to be 1 m. The influence of other geometric dimensions is below 5 % and, in this case, average values are assumed ($h_1=9$ mm, $s_1=11$ mm). The liquid properties are accepted as for water at temperature of 20⁰ C and for the coefficient of molecular diffusion – the values for CO₂ in water, e.g., at the conditions for experimental determination of the mass transfer coefficients. At the same conditions, both models have analytical solutions which are used at processing of the results. For all curves presented on Fig. 16 the mass transfer coefficients k_L^0 which satisfy the dispersion model are determined by Eq. (17) and the Bodenstein number needed to obtain the model solution – by Eqs. (12 – 14).

For the curves of family A (Fig. 16) the mass transfer coefficients in the plug flow model k_L are identified by the analytical solution of the model at

a degree of separation equal to that, determined by the dispersion model [4]. In this sense the curves show the effect of the axial mixing. Two branches are distinguished, related to the “drop” and “jet” regime, respectively. There can be observed a clearly pronounced minimum of the axial mixing effect (around 17÷19 %), where obviously is the optimal operating area of Holpack packing. From the curve’s family A it can be also seen (as was mentioned above) that at high irrigation densities in the “jet” regime the influence of the axial mixing on the efficiency remains relatively low although the axial mixing coefficient, determined by Eq. (13), strongly increases. The plug flow mass transfer coefficients for the curve’s family B are determined by Eq. (16). In this sense the curves show what effect of the axial mixing Eq. (16) expresses, applied, respectively, to the plug flow model.

From the comparison between the two curve families it can be seen that at low and high irrigation densities both models approximately equally express the influence of the axial mixing, while in a wide range of medium irrigation densities, important for the industrial practice, the difference is substantial. In this range the plug flow model can show significant deviations for the predicted effectiveness and, respectively, for the height of the packing layer. The good side in this case is that the plug flow model gives a raised value of the height, which is an additional safety oversizing.

The presented axial mixing effect explains the variable success when using the plug flow model especially at modeling the process of rectification with Holpack packing. That is why it is recommendable in all cases the dispersion model to be used with the corresponding equations for determination of its parameters. From the course of curves A on Fig. 16 the presence of optimal liquid load area for ensuring maximal effectiveness for a given packing and process conditions is obvious. This optimal area depends on the process conditions, as well as mostly on the characteristic sizes of the packing, which gives a possibility and guidelines for its improvement.

TECHNOLOGICAL RESEARCH AND INDUSTRIAL APPLICATION

•For performing absorption and desorption

The first studied process with Holpack packing is deaeration in experimental deaeration column. This is a process where oxygen is separated from water designed for feeding of steam boilers.

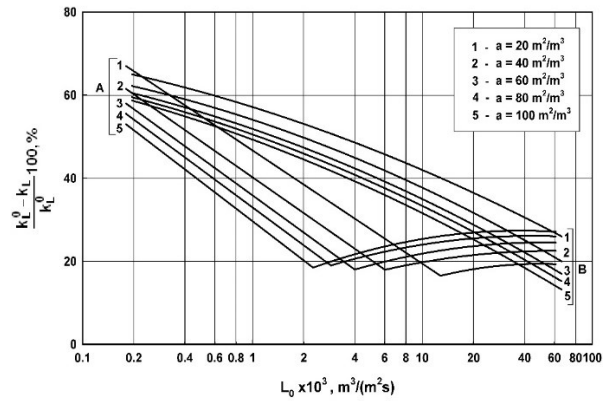


Fig. 16. Influence of the axial mixing in the liquid phase.

The water liable to deaeration is fed uniformly to a column with a diameter of 200 mm and packing No. 20 (Table 1) and steam is moving counter-currently. This packing structure enables quite big irrigation densities and steam velocities to be reached at uniform distribution of the phases on the cross-section of the apparatus and high mass transfer coefficient. The aim of the research carried out in the experimental deaeration column is to check the packing potentialities regarding the liquid and vapor load and applicability of the computing methodology.

For the dimensioning of deaerators, the plug-flow model is applied using the equations of mass balance and mass transfer, controlled by the liquid boundary layer [42]:

$$G = L_0(c_{in} - c_{out}) \quad (18)$$

$$G = k_L a_e H \Delta c_{av} \quad (19)$$

The mass transfer coefficient in Eq. (19) is estimated by the dimensionless Eq. (16) and its specific surface area – by Eq. (11). Because of the practically linear equilibrium concentration of the oxygen in a wide operation range the driving force is a mean logarithmic value of the difference of the incoming, respectively outgoing and the equilibrium concentrations of the oxygen in the apparatus, by the equation:

$$\Delta c_{av} = \frac{(c_{in} - c_{in}^*) - (c_{out} - c_{out}^*)}{\ln \left(\frac{c_{in} - c_{in}^*}{c_{out} - c_{out}^*} \right)} \quad (20)$$

The investigated deaerators [42] operated at atmospheric pressure (0.12 MPa), at vacuum (0.03 MPa) and under pressure (0.7 MPa). The irrigation density at the apparatus with atmospheric and increased pressure is 120 m³/(m²h), and at vacuum - 110 m³/(m²h).

The calculation shows a packing height for the experimental apparatus of 770 mm for atmospheric pressure, 1200 mm for vacuum and 1220 mm for increased pressure. On the walls of the pilot apparatuses deflecting rings are mounted at a distance of 200 mm from one another [42]. At initial (input) concentration of the oxygen in the water of 9.3 mg/kg, the end (outgoing) concentration decreases about 1500 times. It is considered that mounting of deflecting rings leads to a decline of the end concentration of oxygen in the deaerated water from 0.040 to 0.006 mg/kg.

The experiments show that the mass transfer coefficients in these apparatuses coincide with these at model research. Here is interesting to note that at the research conditions (mainly irrigation density around $3.3 \times 10^{-2} \text{ m}^3/(\text{m}^2\text{s})$ and specific packing surface area around $40 \text{ m}^2/\text{m}^3$), the plug flow model, by which the aerator is designed – Equations (19, 20) with mass transfer coefficients, determined by Equation (16), gives practically the same results as the dispersion model (Fig. 16).

The results obtained for deaerators with packing [42] are compared with the results for deaerators with standard perforated plates. The comparison shows that deaerators with Holpack packing have about 4 times smaller volume. The consumption of the ventilated stream is also several times reduced and is only 0.5 kg/t water. Reduced is the specific metal content as well. The oxygen concentration in the water at the end of the deaerators is according to the standard.

The research works carried out confirm the proposed computing methodology. They served for the development of industrial apparatuses with the following productivity: atmospheric and vacuum deaerators – from 2.5 to 25 m^3/h ; atmospheric deaerators – from 50 to 250 m^3/h and deaerators under pressure of 0.7 MPa - from 100 to 350 m^3/h . These apparatuses operate successfully in many power plants.

One of the stages for processing of water for drinking and manufacturing purposes is the decarbonization – the separation of carbon dioxide. It is particularly often used in plants for water treatment for steam boilers. Usually the concentration of CO_2 in the water processed to decarbonization varies from 10 to 100 g/m^3 , but in a number of waters with high carbon hardness, after H-cationization it can reach 500 g/m^3 . The separation of CO_2 from water is performed in degassers, called in this case decarbonizers.

The most commonly occurring apparatuses of this type are packed columns. It was earlier established that the cheapest in terms of energy are

degassers to be filled with Intalox saddles 38 mm. According to this important area of application experiments are carried out in decarbonization columns with Holpack packing No. 19 (Table 1). For determination of the dimensions of the experimental column the Eqs. (19), (20), (16) and (11) are used, since the mass transfer process is controlled by the liquid boundary layer. The aim is to determine the maximum load of the apparatus at a given output CO_2 concentration. The experimental column with capacity of 40 m^3/h is with diameter of 468 mm and packing height of 3400 mm. Wall Flow Deflecting Rings (WFDR) [25, 26] are mounted along the column walls with width of 12 mm and distance between them – 200 mm. The apparatus is mounted after the H-cationite filters of an industrial plant for steam boilers feeding water treatment.

A good conformity between the obtained mass transfer coefficients and those from the model research is established. The comparison of the results [43] with data from other used apparatuses shows the advantage of the degasser with Holpack packing because of the higher allowable loads and regarding the degree of CO_2 separation at given energy expenses. For all experiments at initial concentration of CO_2 40 g/m^3 , the output one is within the range of $1.2 \div 1.8 \text{ g}/\text{m}^3$.

The proposed equations for the Holpack packing characteristics are used for creation of many heat and mass transfer apparatuses. A semi-industrial monoethanolamine absorber with Holpack packing is designed and investigated, with a diameter of 500 mm and packed layer height of 5 m for purification of the technological gas used for methanol synthesis from hydrogen sulfide and CO_2 [44]. The experiments have shown that reloading of the existing absorbers from bubble-cap trays to Holpack packing leads to 5-times intensification of the process at 8-times reduction of the pressure drop. The comparative studies of monoethanolamine absorbers with three types of packings - structured Sulzer BX 500, Mellapak 500 Y and random Pall rings 16×16 mm published recently have shown advantages of the absorber equipped with Sulzer BX500 packing [45].

Application of Holpack in recent years is presented in new type of installation for SO_2 removal from flue gas, producing high-quality gypsum [46].

Also, an apparatus with the same packing for gas processing of the sodium-regeneration boiler at the production of sulfate cellulose is investigated. The aim is purification from dust, sulfur dioxide, other sulfuric compounds and heat utilization [47]. The apparatus has shown very good operation at these heavy technological conditions.

As a result of the research carried out it is established that in all cases the volumetric mass transfer coefficient of the industrial apparatuses coincides well with the coefficient estimated by the equations derived from the pilot research. The deviation, which does not exceed 20 %, is connected with the mass transfer below and above the packing in the industrial apparatuses. The loadings related to a unit packing volume, in industrial columns are bigger than in the apparatuses used before. Moreover, the degree of absorption (desorption) is equal or in most cases higher.

- *For performing distillation and rectification processes*

For the first time Holpack packing (Table 3) is studied for a rectification process by Semkov [33]. The investigations are carried out with a model system tetrachloromethane – chlorophorm at a regime of full reflux return and with four packing configurations. The experiments are performed in a column with a diameter of 0.207 m and packing height – 3 m. The column is mounted above a bottom part, in which electric heaters with total power of 54 kW are built-in, as this power can be gradually switched at intervals of 4.5 kW. The mass transfer and hydrodynamic results show that Holpack packing is suitable for rectification processes.

Later, the same packings (Table 3) are studied with an ethanol – water system [48]. The investigations are carried out at atmospheric pressure with five packing configurations, in a wide range of concentrations and phase velocities. It is established that the effectiveness strongly depends on the experimental operating concentrations. Because of that, further research is done at medium and high concentrations – just like those in the industrial columns for ethanol production.

The investigations at higher concentrations are carried out with two types of Holpack packing – No. 25 with small openings ($d_h = 6.5$ mm) and No. 26 with bigger openings ($d_h = 25.6$ mm (Table 1) [49, 50]. The results are presented as HTU and Height Equivalent to a Theoretical Plate (HETP). The packing with the bigger openings has shown better results.

At the investigations of the packing with the smaller openings (No. 25 from Table 1) experiments with variable reflux ratio are also carried out [51]. It is established that at reducing the liquid-vapor ratio, the effectiveness deteriorates. The effectiveness at a reflux ratio of 3.5, at which the real industrial plants for production of ethyl alcohol at atmospheric pressure operate, is also determined. The value of HTU is 0.42 in this case.

As a result of this research the developed unified

mathematical model for dimensioning of packed columns for mass- and heat transfer processes [5] is verified. It takes into account effects of different origin, which occur as in absorption, as well as in rectification and direct heat transfer. Especially in rectification, particular attention has been paid on the turbulization of the inter-phase surface – the Marangoni effect [52], which affects the mass transfer coefficient in the liquid boundary layer. The axial mixing in the liquid phase is taken into account through the one-parameter dispersion model using Eqs. (12-14) for determination of the Bodenstein number and Eq. (17) – for the mass transfer coefficient in the liquid boundary layer. The axial mixing in the gas (vapor) phase is assumed to be insignificant because of the packing structure itself. The influence of the axial mixing in the liquid phase is studied on experimental data from a rectification of ethanol – water system. It is shown that in the range of the irrigation densities that are typical for this process this influence is essential and has to be taken into account by all means.

The proposed approach for calculating columns with Holpack packing [5] is successfully used in the realization of a large number of industrial projects [53]. On this basis 9 industrial plants for production of ethyl alcohol have been constructed, comprising 35 distillation and rectification columns with this packing (Fig. 17). The installations have productivity from 1,000 to 20,000 l/24 h. The columns are mainly supplied with packings No. 26 and No. 25 (Table 1).

The Holpack packing is successfully implemented in industrial plants for purification of waste waters from butyl acetate and butanol in antibiotics production [54]. This is accomplished in a stripping installation, which consists of two columns – a hollow and a packed column. In the plant for purification from butyl acetate, the column is with diameter of 800 mm and packing height of 2000 mm while in that for purification from butanol the diameter is 1200 mm and the height is 4000 mm.

The initial concentrations of butyl acetate in the waste waters in the plant for purification of butyl acetate are within 5.49 and 19.6 g/l, the steam consumption is from 0.055 to 0.200 kg/kg purified water, and the degree of purification is from 99.1 to 100 %. For the butanol plant the initial butanol concentration varies from 12.6 to 14.0 g/l, the steam consumption is 0.18 kg/kg purified water and the degree of purification is 99.9 %.



Fig. 17. Photograph of a rectification plant for ethanol production with productivity of 20000 litres/24h consisting of five columns with Holpack packing

Another realized application of Holpack packing is again in a stripping column, this time for purification of waste waters from chloroform [55]. The column is with diameter of 400 mm and packing height of 6400 mm. The amount of the treated water is within 1.8 and 2.2 m³/h and the amount of steam is from 160 to 177 kg/h. The initial chloroform concentration in the waste waters is 7 g/l and the final (output) one varies from 0.044 to 0.164 mg/l. The degree of purification is in the range of 99.994 – 99.999 %. For both of the above-mentioned cases packing No. 24 (Table 1) is used.

Holpack packing is also used in the ethereal oil industry. The experiments have established that in cohobating columns for treatment of secondary distillation waters from essential oil production, the packing shows very good properties. As contact elements in the column packing No. 20 (Table 1) is used. The comparison with columns with other types of packing, including some modern random packings, shows that columns with Holpack packing have the highest effectiveness [56].

- *For performing direct contact heat transfer*

Increasing the economy of boilers, furnaces, dryers and other heat facilities depends on the reduction of the waste heat of the exhaust gases, which in the heat balance can be more than 10 %. To reduce the temperature of the outgoing gases various surface-type heat exchangers are commonly used. These facilities are metal-consuming, their sizes and

expenditures are significant and they cause additional high resistance on the way of the gas. Another option is the direct phase contact heat exchange. The apparatuses operating on this principle have simple construction, compactness, low metal capacity and comparatively high heat transfer intensity due to the direct contact between the fluids. Using the contact heat exchangers (economizers) for utilization of the flue gases heat enables not only reducing the price of the utilizer but also assuring deeper gas cooling below the gas original dew point temperature, which is 58 - 61 °C for the products of natural gas combustion. Besides, not only the sensible heat of the flue gases but also the latent heat of condensation of a part of water vapor content is recovered [57–61].

Direct contact gas cooling is accomplished mainly in a counter-current flow by water or another liquid. This liquid is used for heating of water or air for technological purposes. The most prevalent are the contact economizers with packing given that they provide a process possibly closest to a complete counter-current flow. The main part of the contact economizers is the contact camera, i.e., the part of the apparatus where the packing is placed and where the heat- and mass transfer process is going on most actively. There, a developed contact surface for the cooled gases and the liquid and also high intensity of the process per unit volume at possibly lower pressure drop have to be provided.

The available data for determination of the heat transfer coefficient are obtained for specific cases, and are related to processes in rather narrow borders. For this reason, it is advisable to seek other ways of determining it. One simplification of the task comes from the fact that the direct simultaneous heat- and mass transfer in a system water – gas (air) is connected with condensation of water vapors whereupon the process is controlled practically entirely by the gas boundary layer. To determine the heat transfer coefficient, the Lewis and Chilton-Colburn analogy between heat and mass transfer [3, 62, 63] can be used as is proven in [64].

Thus, analogically to equation (10) the following equation for the coefficient of heat transfer in the gas boundary layer can be written:

$$Nu_G = 0.26 Re_G^{0.73} Pr_G^{0.33} \quad (21)$$

where the Nusselt and Prandtl numbers are defined by the expressions:

$$Nu_G = \frac{h_G d_h}{\lambda_G}; \quad Pr_G = \frac{\nu_G}{\alpha_G} = \frac{c_{pG} \mu_G}{\lambda_G} .$$

With its characteristics Holpack packing meets

very well the requirements for performing heat- and mass transfer processes in contact economizers. It has a large interphase surface created in the first place by the surface of the drops and jets flowing from sheet to sheet, whereupon the liquid film is frequently broken and a renewal of the interphase surface is accomplished at a significant free volume.

For the determination of the packing height the plug-flow model consisting of the simultaneous heat- and mass transfer balance equations and the corresponding parameter expressions (11, 15, 21) is used [60, 64-66].

The experiments for verification of the model are carried out on a pilot plant with a contact economizer with packing Holpack No. 22 (Table 1) with a diameter of 470 mm and a height of a 1200 mm [67]. Flue gases are fed, obtained by the combustion of natural gas in a steam boiler with a capacity of 1.5 t/h steam. The gas velocity is varied within the range of $w_0 = 1.3 \div 3.4$ m/s, the irrigation density $1.2 \times 10^{-2} \div 2.8 \times 10^{-2}$ m³/(m²s) and the initial moisture content of the gases $0.12 \div 0.41$ kg/kg dry gas. The higher values are achieved by adding complementary steam to the flue gases. The obtained data are processed with software based on the proposed model.

In most of the cases the hot gases are obtained at the combustion of natural gas (NG). One interesting research of the possibility for using of the contact economizers with Holpack packing is presented in publication [65]. There, the flue gases are produced by the combustion of high-quality coal with low sulfur content.

In all cases considered so far, water is used as a liquid – heat transfer fluid. The maximal temperature, up to which theoretically the fluid can be heated, is the adiabatic saturation temperature of the gas. In a water - air/flue gas system this temperature coincides with the wet bulb temperature and the dew point temperature. For flue gases from NG burning at 1.1÷1.2 air excess it is about 60 °C. Technologies are developed [68] where the water can be heated to higher temperatures using high-temperature heat transfer fluid, for example oil.

- *Other processes suitable for Holpack packing application*

With its low pressure drop, high mass transfer coefficients and large interphase area, the Holpack packing is suitable for all kinds of absorption processes convenient for packed columns. Particularly appropriate for its implementation are those types of processes where the liquid – gas ratio is low. It is usually determined by the requirements of the mass and heat balances. In this case the column operates at low irrigation densities. At operating with Holpack packing, the effective area

depends on the irrigation density weaker than at the random packings widely used in the industry. Such processes are almost all of the processes for purification of industrial flue gases that contain a small amount of absorbable component. One additional, quite important characteristic of the packing at such processes is its very good liquid distribution on the column cross-section.

The continuous change in the direction of the gas phase passing through the Holpack packing makes it appropriate for separation of the liquid phase from the gas flow. Devices made of expanded metal sheet are successfully used for reducing the carrying away of drops in a number of apparatuses. Practically, the total wetting of the packing, combined with the continuous change of the gas phase and the inertia forces arising from this change make the Holpack packing a particularly promising dust-catcher. Besides, its low pressure drop may be crucial for its application in this field. The packing's big free section and the lack of stagnation zones in it, make Holpack packing very convenient for operation with very dirty liquids and gases. This is particularly suitable in the cases where the solid phase does not tend to stick to the walls.

The Holpack packing can find prevalence in the direct cooling of water with air flow. Usually, the adiabatic water cooling in cooling towers is led at comparatively low irrigation densities where the Holpack packing is particularly suitable.

In this regard, cooling towers with this packing are constructed and implemented for cooling of the water from the condensers of the rectification columns of ethanol production plants. The towers are with a capacity of 12 and 40 m³/h and packing height of 1500 and 1800 mm (Holpack No. 23, Table 1). The cross-sections of the towers are 2.25 and 3 m². The long observations and investigations show very good results for possibly the deepest cooling.

PACKING IMPROVEMENT AND INTENSIFICATION OF THE PROCESSES

The detailed research of Holpack packing, regarding its hydrodynamic and mass transfer characteristics, shows very good results. The developed methods for estimation and semi-industrial verification confirm the expected results. The designed and implemented into practice industrial apparatuses operate successfully in different areas of the chemical and food industry, the power sector and environment protection.

The Holpack packing is created on the basis of an existing configuration of expanded metal sheets. This is a standard machinery article, designed for other purposes.

Nevertheless, the results show that it is close enough to the sheet shape, which can lead to still better results. Obviously, the principle of operation is felicitous and the same tendency should be followed to perfect this contact heat- and mass transfer device.

In order to improve the operation parameters of the packing, a detailed preliminary analysis of the factors that determine its characteristics should be done.

The investigation of the pressure drop of Holpack packing showed very low values of this parameter. This is due to its structure and the fact that its main elements are metal sheets with big free void. Our striving for reducing the metal capacity by decreasing the sheet thickness to 0.6 or 0.7 mm will lead to an increase in this section. Moreover, the distance between the sheets, which is usually in the range of 10 – 50 mm, is free and helps for the radial gas spreading and equalization of the velocity profile. Holpack packing provides a very good liquid spreading on the column cross-section. The investigations show that this strongly depends on its geometric characteristics – Eqs. (9) and (10). The packings with bigger geometric dimensions have higher spreading coefficients at smaller distances between the sheets (Fig. 5), which strongly depends on the geometrical dimensions and particularly on the

h_1/s_1 ratio. This gives big possibilities for choosing the appropriate sheet dimensions, especially in accordance with their influence on the mass transfer characteristics.

The opportunities to improve Holpack packing and to intensify the processes in comparison with the current level can be easily identified, for instance, by the integral equation of the mass transfer (19). The quantities, which can be influenced at a given height, are mass transfer coefficients, effective surface area and mean integral driving force. To provide the maximal driving force and generally for the applicability of the mathematical models (plug-flow or dispersion model) it is necessary to create close to the ideal conditions, i.e. formation of uniform gas and liquid distribution on the cross-section of the apparatus and a regime of contact close to ideal counter-current flow. Then, for the plug-flow model the mean integral driving force is determined as a mean logarithmic concentration difference – Equation (20) and for the dispersion model it is obtained as an integral solution by taking into account the reducing influence of the axial mixing.

It can be seen from the research presented above that Holpack packing with its structure and principle of operation offers very good conditions for radial distribution of the phases. The gas quickly equalizes its velocity profile and the liquid, which is promptly

spread, eliminates the risk of bypass flows. On the other hand, the deteriorative effect of the wall flow is avoided using wall flow deflecting rings. From Figures 7 and 8 it can be seen that conditions for uniformity of the flows are created. Hence, the construction of the packing forms conditions for assuring of maximal concentration difference. The other factor, which negatively affects the process driving force, as was pointed out, is the axial mixing in the liquid phase. It is inevitable, it is due to the discreet structure of the packing and the local phase contact surface and reflects the minimum possible non-uniformity of the distribution for a given geometric configuration and hydrodynamics of the liquid phase. Fortunately for Holpack packing, as was shown above, there is an optimal area of operation, which minimizes the detrimental effect of the axial mixing (see Fig. 16). As this area depends on the geometric configuration of the packing too, there is a possibility, using Equations (12-14) and (17), to foresee a packing with dimensions that assure the optimal operation at the conditions of a given process.

The other quantities which can be used to make an impact on the intensification of the processes in Holpack packing are the mass transfer coefficients and the effective surface area. This is thoroughly related to observing the requirements of theory of tearing and renewing the mass transfer surface [3, 7-9].

In any case, apparently it comes into question to find an optimal combination of the values of s_1 , h_1 and h_2 , with a purpose of providing maximal effectiveness at given process conditions. These parameters influence through the specific packing surface – Equations (1); effective specific surface – Eq. (11); mass transfer coefficients – Eqs. (16, 17) and axial mixing coefficients – Eqs. (12 ÷ 14).

For instance, Figure 18 shows the influence of the distance between the packing sheets on the main hydrodynamic and mass transfer characteristics.

The detailed analysis, as well as the results from the practical application of Holpack packing show that the additional research for intensification of the packing has to be focused on a tentative distance between the sheets of about 20 mm. It probably creates the best harmony between the effective area of the packing sheets and that of the drops and jets in the empty space between them. This can be seen on Figure 19, where the number of the expanded metal sheets is given in dependence of the distance between the sheets h_2 at different hydrodynamic diameters of the openings. The work on optimization of the dimensions of the expanded metal sheets is eased by the die created and used for production of

Holpack packing, assembled on an ordinary mechanical press. It is meant to produce sheets with a hydraulic diameter of the openings of 17 – 25 mm. The change of the s_1/h_1 ratio is connected with the change in the step between the axes of the staggered slots, whereupon a change in the s_1 dimension is obtained, which affects the dimension h_1 . Besides, the ambition is to maintain the degree of sheet expansion of about 1.6, i.e., the lengthening of the initial metal sheet to be about 60 %.

All of this gives an idea of a distribution of the effective area between this of the sheets and that of the empty space between them. Besides, the striving is for less metal to be put in, in order to obtain a packing with less specific weight. From technologic point of view, this creates conditions for increasing of the specific and effective area and for intensification of the mass transfer through tearing and renewal of the mass transfer surface, including that from the drops and jets flowing in the empty space. They additionally mix the liquid that flows on the lamellae and intensify the mass transfer.

CONCLUSIONS

This study describes the results of the research and implementation of horizontal expanded metal sheet packing, also called Holpack. The Holpack packing is made of expanded metal sheets placed horizontally at a certain distance from one another along the height of the apparatus. Its principle of operation, connected with the creation of a large phase surface area, created also in the empty space between the sheets, makes it quite effective. This is strengthened by the increased mass transfer as a result of the frequent tearing and renewal of interphase surface. It results in a low pressure drop, which creates favorable conditions for a large number of technological processes. The very good parameters, as regards the uniform gas and liquid distribution, approach the operation of the packing to the ideal conditions for performing heat- and mass transfer.

The detailed research of the hydrodynamic and mass transfer characteristics created a methodology for design of apparatuses for absorption, desorption, rectification and distillation processes and direct heat transfer. The industrial realization confirmed the effectiveness of the Holpack packing in apparatuses for chemical and food industry, power and environmental sectors.

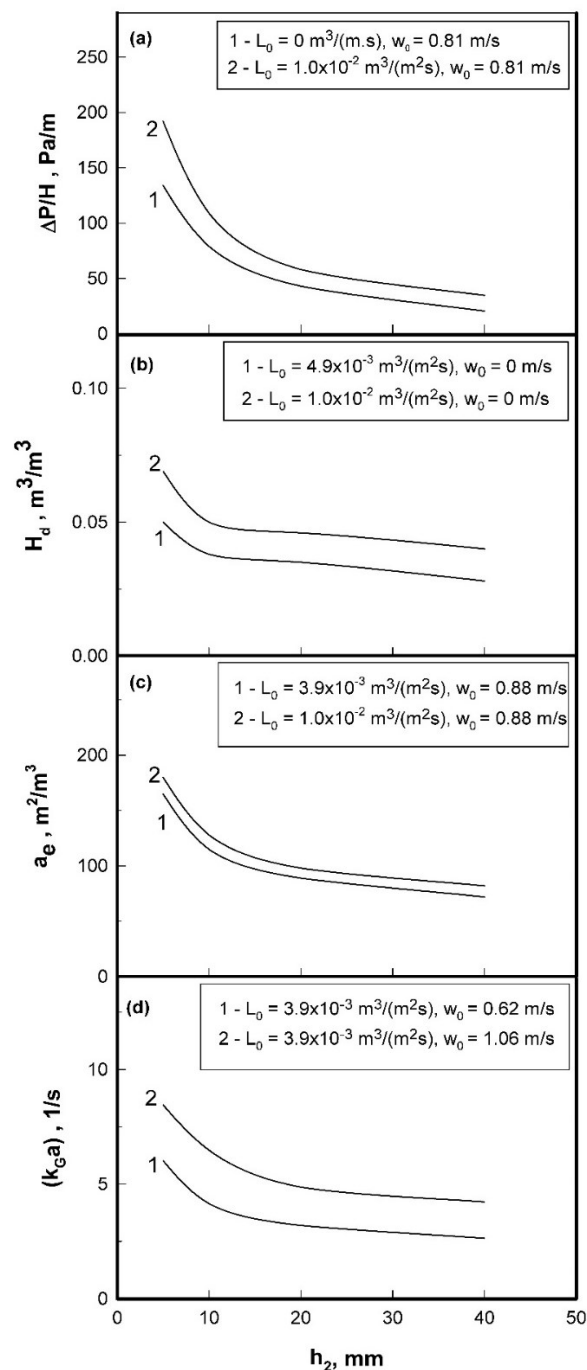


Fig. 18. Influence of the distance between the sheets of packings Nos. 1-4 (Table 1) on: (a) Pressure drop, (b) Hold-up, (c) Effective surface area and (d) Mass transfer coefficient.

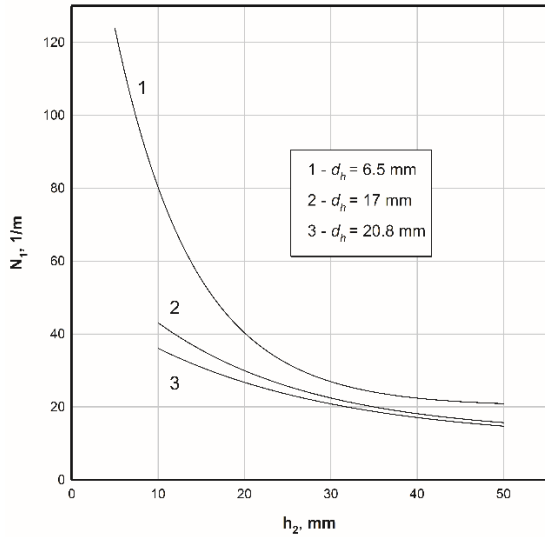


Fig. 19. Dependence of the number of the expanded metal sheets in 1 m height from the distance between them for Holpack packing (Table 1) for different hydraulic diameters of the sheet openings.

The experience gained from the realization of many projects opens up opportunities for improvement and intensification of the apparatuses operating with Holpack packing. The envisaged forthcoming steps are connected with variation of the proportions between some of the main dimensions of the sheets of expanded metal and optimization of the distance between them, according to the requirements of the concrete technological process.

Nomenclature

A - slit length of expanded metal sheet (Fig. 1), m ;
 a - packing specific surface area, m^2/m^3 ;
 a_e - effective specific surface area, m^2/m^3 ;
 B - slit longitudinal (longways) step of expanded metal sheet (Fig. 1), m ;
 C - slit transversal (breadthways) step of expanded metal sheet (Fig. 1), m ;
 C_1 - constant in Eq. (11);
 c - oxygen concentration in water, g/m^3 ;
 c_p - specific heat capacity, $J/(kgK)$;
 D - diffusivity, m^2/s ;
 D_r - radial spreading coefficient, m ;
 D_c - column internal diameter, m ;
 D_{TL} - axial mixing coefficient (part of Bodenstein number) – Eqs. (12, 13), m^2/s ;
 d_h - hydraulic diameter of the slit, m ;
 $F = w_0 \sqrt{\rho_G}$ - gas (vapour) capacity factor (F-

factor), $kg^{1/2}/m^{1/2} s$;
 G - mass of the desorbed component per cross-section unit, $g/(m^2 s)$;
 g - gravity acceleration, m/s^2
 H - packing height, m ;
 H_d - dynamic holdup of the liquid phase, m^3/m^3 ;
HETP - height equivalent to a theoretical plate;
 $HTU_L = \frac{k_L a_e}{L_0}$ - height of the (mass) transfer unit (HTU) for the liquid phase, m ;
 h - heat transfer coefficient, $W/(m^2 K)$;
 h_1 - thickness of the expanded metal sheet (Fig. 1), m ;
 h_2 - distance between the expanded metal sheets (Fig. 1), m ;
 k - mass transfer coefficient, m/s ;
 $(k_G a) = k_G a_e$ - volumetric mass transfer coefficient for the gas phase, $1/s$;
 $(k_L a) = k_L a_e$ - volumetric mass transfer coefficient for the liquid phase, $1/s$;
 L - liquid superficial velocity, $m^3/(m^2 s)$;
 M_f - gas maldistribution factor – Eq. (10);
MAE - mean arithmetical error;
MEA - monoethanolamine;
 N_1 - number of expanded metal sheets per 1 m packing height, $1/m$;
NG - natural gas;
 Q - liquid flow rate, m^3/s ;
SD - standard deviation;
 s - slit width of the expanded metal sheet (Fig. 1), m ;
 s_1 - lamella width of the expanded metal sheet (Fig. 1), m ;
WFDR - wall flow deflecting ring;
 w - gas (vapor) velocity, m/s ;

Greek symbols

$\alpha = \lambda/(\rho c_p)$ - thermal diffusivity, m^2/s ;
 ΔP - pressure drop of packing, Pa ;
 ΔP_0 - pressure drop of dry packing, Pa ;
 δ - thickness of metal sheet (Fig. 1), m ;
 ε - volume void fraction of horizontal expanded metal packing, %;
 ε_1 - free cross-section area of the expanded metal sheet, %;

λ - heat conductivity, $W/(mK)$;
 μ - dynamic viscosity, $Pa \cdot s$;
 ν - kinematic viscosity, m/s^2 ;
 ρ - density, kg/m^3 ;
 σ - surface tension, N/m .

Subscripts

A - air;
G - gas phase;
L - liquid phase;
in - inlet value;
j - single jet;
max - maximum value;
out - outlet value;
O - related to the overall cross-section;
w - related to the wall.

Superscripts

0 - excluded axial mixing value;
 * - equilibrium value.

REFERENCES

- N. Kolev, R. Darakchiev, A method for performing of mass transfer processes, Bulg. Patent No. 16783/17.06.1971, 1971.
- N. Kolev, Packed bed columns: For absorption, desorption, rectification and direct transfer, 1st edn., Elsevier, Amsterdam, 2006. <https://doi.org/10.1016/B978-0-444-52829-2.X5000-6>
- T. K. Sherwood, R.L. Pigford, C.R. Wilke, Mass Transfer, 3rd ed., McGraw-Hill, New York, 1975.
- K. Semkov, N. Kolev, *Commun. Dept. Chem. Bulg. Acad. Sci.*, **22** (2), 329 (1989) (in Bulgarian).
- N. Kolev, K. Semkov, *Chem. Eng. Process.*, **29**, 83 (1991), [https://doi.org/10.1016/0255-701\(91\)87017-W](https://doi.org/10.1016/0255-701(91)87017-W)
- N. Kolev, R. Darakchiev, *Verfahrenstechnik*, **7** (7), 214 (1973) (in German).
- R. Higbie, *Trans. Am. Inst. Chem. Eng.*, **31**(2), 365 (1935).
- P. V. Danckwerts, *Ind. Eng. Chem.*, **43** (6) 1460 (1951). <https://doi.org/10.1021/ie50498a055>
- N. Kolev, K. Winkler, R. Darakchiev, E. Brosh, *Sov. Chem. Ind.* **18**(8) 43 (1986).
- Explaining expanded metal mesh, <http://www.nilesfence.com/files/technical-information-mesh.pdf> (Accessed April 3th 2023).
- Z. Olujic, A. F. Seibert, J. R. Fair, *Chem. Eng. Process.* **39** 335 (2000). [https://doi.org/10.1016/S0255-2701\(99\)00095-1](https://doi.org/10.1016/S0255-2701(99)00095-1)
- Rib mesh packing type BSH. High performance streampacking for thermal mass exchange, <https://www.montz.de/en-gb/streckmetallpackung-typ-bsh>, (Accessed April 3th 2023).
- N. Kolev, R. Darakchiev, *Chem. Ing. Tech.*, **46** (1) 33 (1974) (in German). <https://doi.org/10.1002/cite.330460109>
- R. Darakchiev, Hydrodynamic and mass transfer characteristics of a horizontal packing of expanded metal sheets, PhD Thesis, Bulgarian Academy of Sciences, Sofia, 1974 (in Bulgarian).
- E. Brunazzi, A. Paglianti, *AIChE J.*, **43**, 317 (1997). <https://doi.org/10.1002/aic.690430205>
- M. Fourati, V. Roig, L. Raynal, *Chem. Eng. Sci.*, **80**, 1 (2012). <https://doi.org/10.1016/j.ces.2012.05.031>
- Z. Olujic, *Chem. Biochem. Eng. Q.* **11**, 31 (1997).
- Z. Olujic, R. van Baak, J. Haaring, *ICHEME Symp. Ser.*, **152**, part B, 252 (2006). <https://folk.ntnu.no/skoge/prost/proceedings/distillat-ion06/CD-proceedings/paper023.pdf>
- C. F. Petre, F. Larachi, I. Iliuta, B. P. Grandjean, *Chem. Eng. Sci.*, **58**, 163 (2003). [https://doi.org/10.1016/S0009-2509\(02\)00473-6](https://doi.org/10.1016/S0009-2509(02)00473-6)
- K. A. Semkov, T. St. Petrova, *Bulg. Chem. Commun.*, **52** (F) 80 (2020). <https://doi.org/10.34049/bcc.52.F.0014>
- N. Kolev, R. Darakchiev, *Theor. Found. Chem. Eng.* **10**(6) 828 (1976a).
- M. I. Kabakov, V. V. Dilman, *Theoret. Found. Chem. Eng.*, **7** (4), 539 (1973).
- P. Zhang, W. Huang, H. Chi, S. Wang, *Chinese J. Chem. Eng.*, **14** (4) 464 (2006). [https://doi.org/10.1016/S1004-9541\(06\)60100-6](https://doi.org/10.1016/S1004-9541(06)60100-6)
- R. Darakchiev, A. Boev, N. Kolev, *Chem. Eng. Process.*, **20** 73 (1986) (in German). [https://doi.org/10.1016/0255-2701\(86\)85010-3](https://doi.org/10.1016/0255-2701(86)85010-3)
- N. Kolev, R. Darakchiev, Device for prevention of the spreading of the liquid phase on the column wall, Bulg. Patent No 18018/15.05.1972, (1972).
- R. Darakchiev, N. Kolev, *Chem. Petrol. Eng.*, **22** (8), 379 (1986). <https://doi.org/10.1007/BF01179356>
- R. Darakchiev, *Chem. Eng. Process.*, **18**(6), 317 (1984) (in German). [https://doi.org/10.1016/0255-2701\(84\)87008-7](https://doi.org/10.1016/0255-2701(84)87008-7)
- R. Darakchiev, C. Dodev, *Chem. Eng. Process.* **41** (5), 385 (2002). [https://doi.org/10.1016/S0255-2701\(01\)00151-9](https://doi.org/10.1016/S0255-2701(01)00151-9)
- S. Darakchiev, *Bulg. Chem. Commun.* **42** (4), 323 (2010). http://bcc.bas.bg/BCC_Volume-42-4.html
- T. Petrova, R. Darakchiev, S. Darakchiev, K. Semkov, *Chem. Eng. Technol.*, **31** (12), 1723 (2008). <https://doi.org/10.1002/ceat.200800321>
- N. Kolev, *Verfahrenstechnik* **8**(5), 145 (1974) (in German).
- S. Nakov, N. Kolev, L. Ljutzkanov, D. Kolev, *Chem. Eng. Process.*, **46**, 1385 (2007). <https://doi.org/10.1016/j.ces.2006.11.002>
- K. Semkov, Accounting for the influence of axial mixing for rectification packed columns based on the diffusion model, PhD Thesis, Bulgarian Academy of Sciences, Sofia, (1981) (in Bulgarian).
- K. Semkov, N. Kolev, G. Paskalev, C. Sapundzhiev, *Commun. Dept. Chem., Bulg. Acad. Sci.*, **15** (3), 334 (1982) (in Russian).
- N. Kolev, K. Semkov, *Verfahrenstechnik* **17** (8) 474 (1983) (in German).

36. L. Valenz, F.J. Rejl, V. Linek, *Ind. Eng. Chem. Res.*, **49**, 10016 (2010). <https://doi.org/10.1021/ie101092e>
37. R. Darakchiev, N. Kolev, G. Tchapanova, *Chem. Ing. Tech.*, **46** (1), 31 (1974) (in German). <https://doi.org/10.1002/cite.330460108>
38. C. Wang, M. Perry, G. Rochelle, F. Seibert, *Energy Procedia*, **23**, 23 (2012). <https://doi.org/10.1016/j.egypro.2012.06.037>.
39. N. N. Kolev, R. D. Darakchiev, *Theoret. Found. Chem. Eng.*, **10**(4), 545 (1976b).
40. C. Wang, M. Perry, F. Seibert, G. Rochelle, *Energy Procedia*, **63**, 1727 (2014). <https://doi.org/10.1016/j.egypro.2014.11.180>
41. L. Valenz, F. J. Rejl, V. Linek, *Ind. Eng. Chem. Res.*, **50**, 2262 (2011). <https://doi.org/10.1021/ie101656m>
42. N. Kolev, R. Darakchiev, L. Kolev, *Teploenergetika*, **8**, 91 (1975) (in Russian).
43. N. Kolev, R. Darakchiev, L. Kolev, *Energetika*, **24** (10), 15 (1973) (in Bulgarian).
44. N. Kolev, *Chem. Ing. Techn.*, **47** (16), 685 (1975) (in German).
45. J. Gao, J. Yin, F. Zue, X. Chen, M. Tong, W. Kang, Y. Zhou, J. Lu, *Separ. Purif. Technol.*, **163**, 23 (2016). <http://dx.doi.org/10.1016/j.seppur.2016.02.043>
46. N. Kolev, L. Ljutzkanov, D. Kolev, D. Dzhonova-Atanasova, E. Razkazova-Velkova, *Journal of International Scientific Publication: Materials, methods and technologies*, **5** (1), 375 (2011). <https://www.scientific-publications.net/download/materials-methods-and-technologies-2011-1.pdf>
47. N. Kolev, G. Paskalev, K. Semkov, R. Darakchiev, *Chem. Petrol. Eng.*, **23** (5), 231 (1987). <https://doi.org/10.1007/BF01149769>
48. K. Semkov, *Commun. Dept. Chem., Bulg. Acad. Sci.*, **22** (2), 319 (1989), (in Bulgarian).
49. S. Darakchiev, K. Semkov, *Chem. Eng. Techn.*, **31** (7), 1039 (2008). <https://doi.org/10.1002/ceat.200800029>
50. S. Darakchiev, K. Semkov, *Journal of International Scientific Publications: Materials, Methods & Technologies*, **4** (2), 263 (2010a).
51. S. Darakchiev, K. Semkov, *Scientific Works of Food Science, Engineering and Technologies 2010*, **52** (2) (2010) 561-566.
52. K. Semkov, N. Kolev, *Chem. Eng. Process.* **29** 77 (1991). [https://doi.org/10.1016/0255-701\(91\)87016-V](https://doi.org/10.1016/0255-701(91)87016-V)
53. K. Semkov, *News of the Bulgarian Academy of Sciences*, **6**, 39 (2006).
54. N. Kolev, R. Darakchiev, K. Semkov, *Water Research*, **30** (5), 1312 (1996). [https://doi.org/10.1016/0043-1354\(95\)00289-8](https://doi.org/10.1016/0043-1354(95)00289-8)
55. N. Kolev, R. Darakchiev, K. Semkov, *Ind. Eng. Chem. Res.*, **36** 238 (1997). <https://doi.org/10.1021/ie9506532>
56. S. Tasheva, Research into energy efficiency of cohobating installations, PhD Thesis, UFT- Plovdiv, 2005 (in Bulgarian).
57. I. Z. Aronov, Contact heating of water by burning natural gas, 1st edn., Nedra, Leningrad, Russia, 1987, (in Russian).
58. Considerations when selecting a condensing economizer, Energy efficiency & Renewable energy, U.S. Department of energy, https://www.energy.gov/sites/prod/files/2014/05/fl6/steam26b_condensing.pdf, (accessed April 3th 2023).
59. R. Guillet, The best of a humid combustion: The water vapor pump cycle (WVP Cycle) and other additive water cases, <https://www.econologie.com/fichiers/partager3/1447504733J2gfRJ.pdf> (accessed at April 3th, 2023).
60. N. Kolev, R. Daraktschiev, K. Semkov, in: P. A. Pilavachi, (ed.) *Energy Efficiency in Process Technology*, Springer, Dordrecht, 1993. https://doi.org/10.1007/978-94-011-1454-7_61
61. N. Kolev, *J. Environ. Protec. Ecol.*, **2** (2), 510 (2001).
62. S. Anisimov, D. Pandelidis, *Int. J. Heat & Mass Trans.*, **84**, 974 (2015). <https://doi.org/10.1016/j.ijheatmasstransfer.2015.01.087>
63. W. K. Lewis, *ASME Transactions*, **44** 325 (1922).
64. [N. Kolev, N. Philipova, R. Darakchiev, K. Winkler, *Chemische Technik*, **38** (7), 287 (1986) (in German).
65. K. Semkov, T. Zhelev, *Bulg. Chem. Commun.* **33** (3/4), 395 (2001).
66. K. Semkov, E. Mooney, M. Connolly, C. Adley, in: 8th World Conference on Experimental Heat Transfer, Fluid Mechanics and Thermodynamics, June 16-20, (2013), Lisbon, Portugal, Book of Abstracts, p. 170, (Full text in FD).
67. R. Darakchiev, N. Kolev, G. Paskalev, E. Istatkova, *Teploenergetika*, **3**, 71 (1985) (in Russian).
68. R. Darakchiev, K. Semkov, N. Kolev, *Teploenergetika*, **6**, 75 (1988) (in Russian).

Modeling of rectification in a laboratory single-sieve tray column

D. R. Koleva*, M. K. Karaivanova

Chemical Technologies Department, Technical Sciences Faculty, Prof. Dr Assen Zlatarov University, Burgas,
Prof. Yakim Yakimov Blvd. 1, Burgas 8010, Bulgaria

Received: December 27, 2023; Revised: February 28, 2024

The design of rectification columns is based on the method of the "theoretical tray" and the actual setup of real-life trays is carried out with the help of various kinetic characteristics, such as tray efficiency. A theoretical method for calculating tray efficiency has not yet been proposed due to the complex hydrodynamic setting and the influence of a range of factors. Empirical correlations for calculating the local or integral efficiency of the tray can be found in the literature. The aim of the present work is to make a comparison between the experimentally obtained data from the rectification of a model tetrachloromethane-toluene binary mixture in a laboratory single-sieve tray column and the local efficiency data calculated by means of a model known from the literature, as well as to determine the parameters of the applied model. A good match was established between the calculated and experimental data about the local efficiency and the total number of mass-transfer units of the tetrachloromethane-toluene mixture, the maximum error being below $\pm 25\%$. A match of the LPR% obtained by the model was found: with the percentage given when applying Zuderweg's model (1982) and Chen and Chuang's model (1993) at HVC concentrations in the initial mixture 38.6% and 22.9%, respectively. The studied model can be used to predict the local efficiency in the rectification of any binary mixture depending on its physicochemical properties even at low vapor velocities.

Key words: distillation, sieve trays, local efficiency, number of mass-transfer units, percentage of liquid-phase resistance over total mass-transfer resistance

INTRODUCTION

Sieve tray columns are widely used in practice to separate liquid mixtures by means of rectification. Rectification tray columns are a kind of bubble apparatus where mass transfer between the two phases is carried out on trays located one above the other [1]. Optimizing distillation equipment and processes can improve both the profitability and the greenness of an operation [2]. One approach to optimizing distillation is to design green columns. As a more effective approach, Pilling and Summers [2] discussed to build columns with smart designs. The most important operating characteristics of a tray column are its performance (loads on both phases) and efficiency. The type and dimensions of the tray determine the working loads with regard to vapor and liquid at which it will most efficiently operate [3, 4].

The design of rectification columns is based on the method of the "theoretical tray", that is a tray where equilibrium concentrations of the interacting phases are assumed to occur. The actual setup of real trays is carried out with the help of different kinetic characteristics. One such characteristic is the tray efficiency. The efficiency of the mass exchange process on the individual tray is determined by the differential and integral characteristics [4]. The

differential characteristics of mass-transfer efficiency (E_{OG}) depend on the kinetic parameters of the process and mainly reflect the diffusion resistances of the two contacting phases.

The initial studies of tray efficiency in rectification were based on the generalized experience gained in the operation of industrial columns and suggested empirical correlations for the calculation of the overall column efficiency or tray efficiency, especially of bubble cap and sieve trays. The first proposed correlations and their modifications were derived by summarizing the experience of operating rectification columns in the oil refining industry, where a small number of parameters affect the process (α, μ_L, x_F). Today, they are still used for initial calculation of the local efficiency in the separation of hydrocarbon mixtures.

Later, the proposed correlations included constructional and operating parameters, but remained valid only for a certain type of trays and operating conditions. Syeda and Afacan [5] reported a new model for predicting point efficiency of cross-flow sieve trays that has been developed based on the hydrodynamics of an operating sieve tray represented by the proposed froth structure model. This efficiency model is applicable for both froth

* To whom all correspondence should be sent:
E-mail: desikol@abv.bg

and spray regime [5]. In work [6] appropriate ways are established for estimating the efficiencies of valve trays with downcomer and dualflow trays of industrial distillation columns. Different methods to predict the efficiency in valve trays and dualflow trays are developed and compared against data from three industrial distillation columns under different operating conditions [6, 7]. Lamprecht [8] focused on the development and experimental validation of two simplistic and cost-effective methods that can be used to quantify column internal efficiency. The ADIBAA (aqueous desorption of isobutyl acetate in air) and HA (humidification of air) methods are proposed for efficiency measurements in packed and tray columns, respectively [8, 9]. Chen and Chuang [10] have developed correlations for predicting the number of individual mass-transfer units and the liquid-phase resistance consistent with mass-transfer theories, and to compare the prediction with distillation data from commercial-size sieve tray columns.

The aim of the present work is to compare the local efficiency data obtained experimentally from rectification of a model tetrachloromethane-toluene binary mixture in a single-sieve tray laboratory column [11, 12] and the data calculated using a model known from the literature [10], as well as to determine the parameters of the applied model. The studied method is semi-empirical and allows for the calculation of the number of mass-transfer units and the local efficiency, as well as the determination of the percentage of the liquid phase resistance over the total resistance of the mass-transfer process. The present study is a continuation of the work of Karaivanova and Koleva [13].

Model structure

The differential (local or point) characteristic defines the mass transfer in an elementary volume of the gas-liquid system and the integral characteristic does so on the entire tray. The local efficiency coefficient, E_{OG} , (local efficiency) is used as a differential characteristic of the efficiency of mass transfer while the tray efficiency coefficient or Murphree efficiency, E_{MV} , is used as an integral characteristic of the mass transfer efficiency of the entire tray. By assuming that the flow rates are constant along the height of a counter-current column, we distinguish Murphree efficiency- E_{MV} , for the vapor phase of the n^{th} tray as follows:

$$E_{MV} = \frac{y_n - y_{n-1}}{y^* - y_{n-1}}, \quad (1)$$

where: y_n, y_{n-1} are the average compositions of the outflowing and inflowing vapor flows on the n^{th} tray, respectively; y^* is the composition of the vapors in

equilibrium with the liquid outflowing from the tray with composition x_n .

To define the local (point) efficiency an analytical expression similar to equation (1) is used, the difference being that all concentrations refer to inflows and outflows of a randomly selected elementary volume of the gas-liquid layer. Thus, the vapor phase local efficiency will be determined by equation (2):

$$E_{OG} = \frac{y_p - y_{p-1}}{y^* - y_{p-1}}, \quad (2)$$

where $p, p-1$ refer to the inflows and outflows of an elementary volume.

Due to the complex hydrodynamic state and the influence of a number of factors, a theoretical method for calculating tray efficiency has not yet been proposed [13]. To determine the local efficiency, the model of Chen and Chuang [10] and a semi-empirical method for determining the model parameters were used. The studied semi-empirical method allows for the calculation of the local efficiency under the following assumptions and operating conditions [13]:

- The mass transfer mechanism on the dividing surface (interfacial area) between two phases is described by the Lewis and Whitman two-film theory. Mass transfer is regarded as a two-stage process of consecutive transfer of the substance through the liquid and vapor phases by molecular means. The dividing surface is assumed to have no resistance on the transfer, since a phase equilibrium between the concentrations of the transferred component in the two phases is established on it.
- The total resistance of the process is the sum of the resistances in the individual phases, with the distribution of the total resistance between the phases being also dependent on the phase equilibrium and the resistance through the dividing surface being zero.
- It is assumed that the transfer of the substance through a moving interfacial area is described by the penetration mechanism or the surface renewal mechanism.
- Ideal flow structures on the tray are assumed: a model of complete mixing of the liquid and a model of ideal (full) displacement for the vapor phase.
- Rectification is assumed to proceed under the conditions of total reflux ($G = L$) [13].

As a result of the above assumptions, the local efficiency calculation model was derived using the following scheme:

$$E_{OG} = 1 - \exp(-N_{OG}) \quad (3)$$

$$N_{OG} = K_{OG} \cdot a \cdot t_G = \frac{N_G}{1 + \lambda \frac{N_G}{N_L}} = \frac{N_G}{1 + m \frac{G}{L} \frac{N_G}{N_L}} \quad (4)$$

$$N_G = k_G \cdot a \cdot t_G = C_1 \cdot \frac{1}{\mu^{0.1} \cdot \phi^{0.14}} \cdot \left[\frac{F_S^2 \cdot \rho_L}{\sigma^2} \right]^{\frac{1}{3}} \cdot (D_G \cdot t_G)^{0.5} \quad (5)$$

$$N_L = k_L \cdot a \cdot t_L =$$

$$C_2 \cdot \frac{1}{\mu^{0.1} \cdot \phi^{0.14}} \cdot \left[\frac{F_S^2 \cdot \rho_L}{\sigma^2} \right]^{\frac{1}{3}} \cdot \left(\frac{M_G \cdot G}{M_L \cdot L} \right) \cdot (D_L \cdot t_L)^{0.5} \quad (6)$$

$$N_{OG} = \frac{N_G}{1 + \lambda \frac{N_G}{N_L}} = \frac{C_1 \cdot \frac{1}{\mu^{0.1} \cdot \phi^{0.14}} \cdot \left[\frac{F_S^2 \cdot \rho_L}{\sigma^2} \right]^{\frac{1}{3}} \cdot (D_G \cdot t_G)^{0.5}}{\lambda \cdot \frac{C_1}{C_2} \cdot \left(\frac{D_G \cdot \rho_G}{D_L \cdot \rho_L} \right)^{0.5} \cdot \left(\frac{M_L \cdot L}{M_G \cdot G} \right) + 1} \quad (7)$$

The percentage of the liquid-phase resistance over the total mass-transfer resistance can be defined as:

$$LPR\% = \frac{\lambda / N_L}{1 / N_G + \lambda / N_L} = \frac{m}{\frac{C_2}{C_1} \cdot \left(\frac{D_L \cdot \rho_L}{D_G \cdot \rho_G} \right)^{0.5} \cdot \left(\frac{M_G}{M_L} \right) + m} \quad (8)$$

where C_1 , C_2 are the constants fitting by experimental data [11, 12].

In the model it is assumed that for the gas-liquid layer of the sieve tray, the time that the gas remains in the layer (holdup time) is equal to the contact time of the vapor phase in Higbie's model [13].

$$\theta_G = \frac{h_L}{W_V} = t_G \quad (9)$$

$$t_L = \frac{t_G \cdot \rho_L}{\rho_G} \quad (10)$$

The height of the clear liquid on the sieve tray plays an important role in the mass transfer process and is influenced by the holdup times of the vapor and liquid phases in the gas-liquid layer, t_G and t_L . In the present work, the height of the clear liquid on sieve trays was calculated using equation (11) proposed by Zuiderweg [14]:

$$h_L = 0,6 \cdot h_w^{0,5} \cdot p^{0,25} \cdot \left[\frac{(\rho_G / \rho_L)^{0,5}}{b} \right]^{0,25} \quad (11)$$

This allowed to determine the contact time in Higbie's model, which cannot be calculated or determined experimentally so far. The contact time for the liquid phase was calculated by the contact time of the vapor phase observing the condition that the two phases have equal volumetric flow rates.

The interfacial area was calculated using equation (12), proposed by Chen and Chuang [10].

$$a = \frac{1}{\mu^{0.1} \cdot \phi^{0.14}} \cdot \left[\frac{F_S^2 \cdot \rho_L}{\sigma^2} \right]^{\frac{1}{3}} \quad (12)$$

$$F_S = W_V \cdot (\rho_G)^{0.5} \quad (13)$$

To compare the experimentally obtained local efficiency data and the data calculated by the model, a model tetrachloromethane-toluene binary mixture was chosen. The experiments were carried out using

a laboratory single-sieve tray glass column with a diameter of 0.032 m and external outlet weirs [12]. The small diameter of the column and the outlet weirs ensured the inflow of the liquid for complete mixing on the tray and allowed for a direct experimental determination of the local efficiency. For complete mixing of the liquid on the tray and full displacement of the vapor phase in height of the gas-liquid layer, the two efficiencies have the same values [13]:

$$E_{MV} = E_{OG} \quad (14)$$

To determine the experimental number of mass-transfer units in rectification, the following dependence was used:

$$N_{OG-exp} = -\ln(1 - E_{OG-exp}) \quad (15)$$

Equation (1) was used to determine the experimentally obtained local efficiency E_{OG-exp} .

RESULTS AND DISCUSSION

Constants C_1 and C_2 of the model were determined under the conditions of total reflux $G/L = 1$ from equation (7) by using experimental data for N_{OG} , as a function of the slope of the equilibrium line m by the following equations:

$$N_{OG-cal} = \frac{C_1 \cdot A}{m \cdot z_1 \cdot B + 1} \quad (16)$$

$$A = \frac{1}{\mu^{0.1} \cdot \phi^{0.14}} \cdot \left[\frac{F_S^2 \cdot \rho_L}{\sigma^2} \right]^{\frac{1}{3}} \cdot (D_G \cdot t_G)^{0.5} \quad (17)$$

$$B = \left(\frac{D_G \cdot \rho_G}{D_L \cdot \rho_L} \right)^{0.5} \cdot \left(\frac{M_L \cdot L}{M_G \cdot G} \right) \quad (18)$$

$$z_1 = C_1 / C_2 \quad (19)$$

The values of the constants obtained for the tetrachloromethane-toluene model mixture were published in [13].

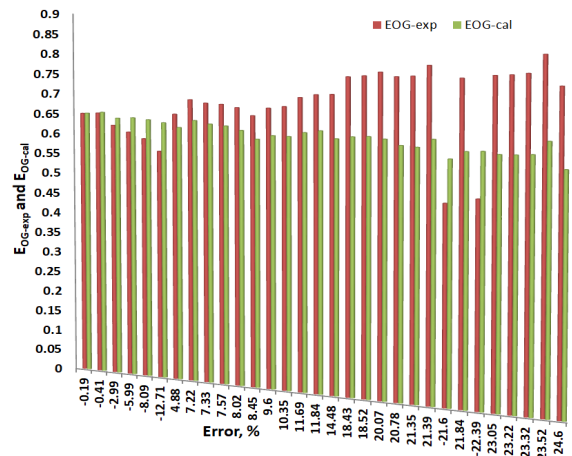


Fig. 1. Comparison between the experimental data on the local efficiency for the tetrachloromethane-toluene mixture and those calculated by the model.

Fig. 1 shows a comparison between the experimentally obtained data on the local efficiency and those calculated by the model. For the tetrachloromethane-toluene mixture, the applied model enabled the prediction of the local efficiency by vapor phase, in this case, with a maximum error below $\pm 25\%$ compared to that obtained experimentally.

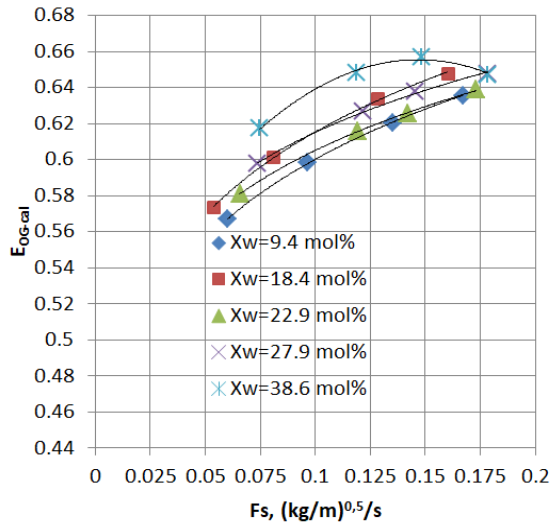


Fig. 2. Dependence of E_{OG-cal} calculated by equation (3) on the load factor (F-factor) at HVC concentrations of the initial mixture of 9.4%; 18.4%; 22.9%; 27.9% and 38.6%.

For the studied tetrachloromethane-toluene mixture, the range of the load factor is $F_s = 0.05 \div 0.18 \text{ kg}^{0.5}/(\text{m}^{0.5}\cdot\text{s})$ at vapor velocity $W_V = 0.0288 \div 0.0874 \text{ m/s}$ at concentrations of highly volatile components (HVC) in the initial mixture of 9.4%; 18.4%; 22.9%; 27.9% and 38.6%. As can be seen from Fig. 2, the increase of the load factor leads to an increase of the local efficiency calculated by the model and it reaches 66% at a load factor of 0.15 $\text{kg}^{0.5}/(\text{m}^{0.5}\cdot\text{s})$ at HVC concentration of the initial mixture of 38.6%.

When the load factor changes in the interval $F_s = 0.075 \div 0.16 \text{ kg}^{0.5}/(\text{m}^{0.5}\cdot\text{s})$, there is a coincidence of the local efficiency E_{OG-cal} calculated by the model at HVC concentrations of the initial mixture of 18.4% and 27.9%. The values of the local efficiency E_{OG-cal} calculated by the model also coincide in the load factor interval $F_s = 0.125 \div 0.175 \text{ kg}^{0.5}/(\text{m}^{0.5}\cdot\text{s})$ at HVC concentrations of the initial mixture of 9.4% and 22.9% (Fig. 2).

The dependence of the number of vapor phase mass-transfer units N_{G-cal} on the flow parameters under total reflux conditions is shown in Fig. 3.

In a narrow range of variation of the flow parameters there is an increase from 1 to 1.04 in the number of mass-transfer units by vapor phase

calculated by the model. There is little research in the literature on this small interval of flow parameters $FP = 0.0576 \div 0.0604$ corresponding to low vapor velocities. For the tetrachloromethane-toluene mixture studied, a coincidence of the number of mass-transfer units per vapor phase N_{G-cal} calculated by equation (16) with those of Zuideweg [14] is observed when FP changes from 0.0576 to 0.0604 (Fig. 3).

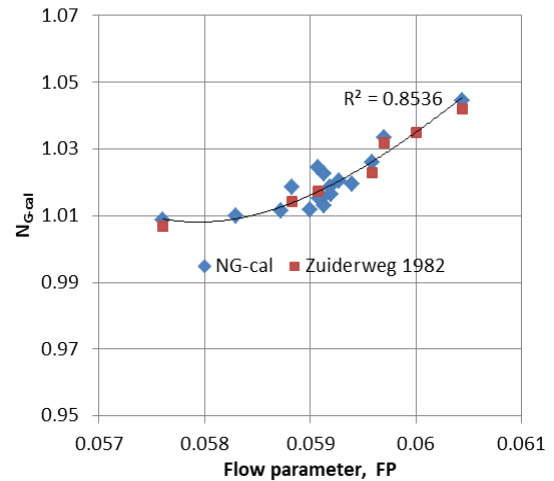


Fig. 3. Comparison between the number of vapor phase mass-transfer units N_{G-cal} with results of [14].

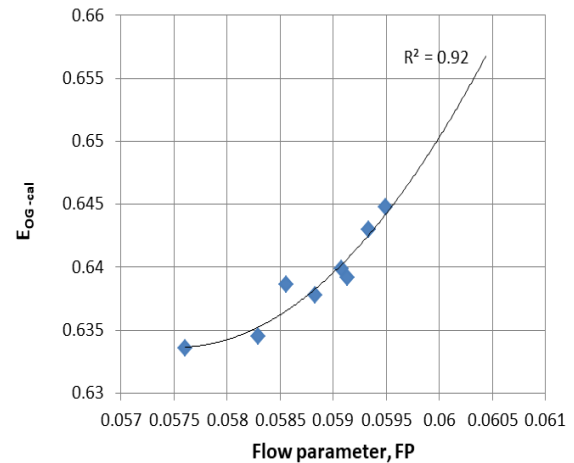


Fig. 4. Effect of the flow parameters under total reflux conditions (FP) on the vapor phase local efficiency calculated by the model, E_{OG-cal} .

With the increase of HVC concentration in the initial mixture from 22.9%; 27.9% to 38.6% and changes in the flow parameters in the interval $FP = 0.0576 \div 0.0595$, corresponding to vapor velocity $W_V = 0.0705 \div 0.088 \text{ m/s}$, a smooth increase in the local efficiency by vapor phase calculated by the model E_{OG-cal} can be seen, the maximal error being below $\pm 25\%$ (Fig. 4).

The applied model also allows the prediction of the total number of mass-transfer units, in this case

by vapor phase, at maximum error below 25%, as compared to those obtained in the tetrachloromethane-toluene mixture experiment (Fig. 5).

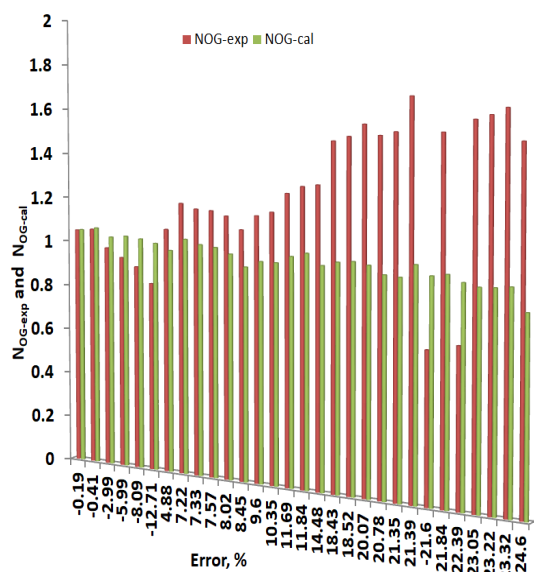


Fig. 5. Comparison between the experimental data on the total number of mass-transfer units for the tetrachloromethane-toluene mixture and those calculated by the model.

Porter and Jenkins [15] pointed out that under the conditions of total reflux all properties of a system can be expressed as a function of the flow parameters $FP = \left(\frac{\rho_G}{\rho_L}\right)^{0.5}$. The flow parameters can be used as a variable to compare the local efficiency, the number of transfer units in the mass-exchange process, the resistance of the liquid phase on the total resistance of the mass-transfer process and to predict them by existing models.

Fig. 6 shows a match of the LPR% obtained by the applied model for the tetrachloromethane-toluene mixture at a concentration of HVC in the initial mixture of 38.6% with the percentage given by applying Zuiderweg's model [14] and, at a concentration of HVC in the initial mixture of 22.9%, with those presented by applying Chen and Chuang's model [10]. The match of the LPR% values obtained by the applied model with those presented by Zuiderweg [14] and Chen and Chuang [10] corresponds to a variation of the flow parameters $FP = 0.0580 \div 0.0596$. For a small range of flow parameters Chen and Chuang's FP model [10] gives high LPR% values compared to other models. For the studied mixture, higher LPR% values were obtained compared to Chen and Chuang's model [10] at an HVC concentration in the initial mixture of 9.4% for LPR% from 61% to 68% and at an HVC concentration in the initial mixture of

18.4% for LPR% from 70.1% to 70.8% (for variation of flow parameters $FP = 0.0586 \div 0.0604$). LPR% values of 47.8% to 56.2% were obtained at an HVC concentration in the initial mixture of 27.9% in a narrow variation range of the flow parameters $FP = 0.0581 \div 0.0596$ (Fig. 6).

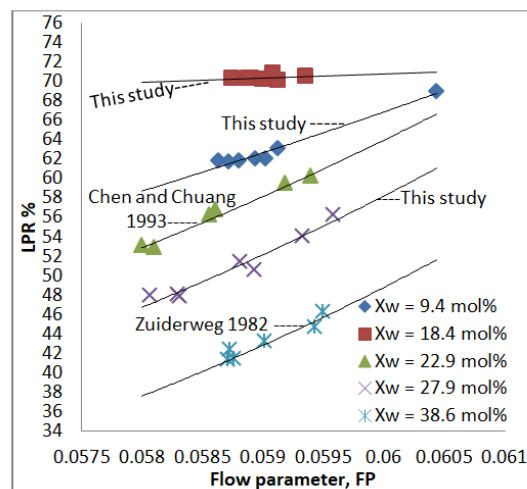


Fig. 6. Comparison of the resistance of the liquid phase over the total resistance of the mass-transfer process, LPR% for the tetrachloromethane-toluene mixture with that obtained by other models.

CONCLUSIONS

The feasibility of a semi-empirical model developed on the basis of Lewis and Whitman's model and the penetration model for calculating the local efficiency for a tetrachloromethane-toluene model mixture was checked. The values of the constants in the model were determined, based on a comparison between the experimentally obtained local efficiency data and those calculated by the model. A good match was established between the calculated and experimental data about the local efficiency and the total number of mass-transfer units of the tetrachloromethane-toluene mixture, the maximum error being below $\pm 25\%$. For the studied mixture, a match of the number of mass-transfer units by vapor phase calculated by the model with those of Zuiderweg [14] was found for FP from 0.0576 to 0.0604. With the increase of HVC concentration in the initial mixture from 22.9% to 38.6% and changes in the flow parameters in the interval $FP = 0.0576 \div 0.0595$, corresponding to vapor velocity $W_V = 0.0705 \div 0.088 \text{ m/s}$, a smooth increase in the local efficiency by vapor phase calculated by the model was established, the maximal error being below $\pm 25\%$. A match of the LPR% obtained by the model was found: with the percentage given when applying Zuiderweg's model [14] at an HVC concentration in the initial mixture

of 38.6%, and with the percentage presented when applying Chen and Chuang's model [10] at an HVC concentration in the initial mixture of 22.9%. Higher LPR% values were obtained compared to Chen and Chuang's model [10]: LPR% from 61 to 68% at an HVC concentration in the initial mixture of 9.4% and LPR% from 70.1 to 70.8% at an HVC concentration in the initial mixture of 18.4%. The studied model can be used to predict the local efficiency in the rectification of any binary mixture depending on its physicochemical properties even at low vapor velocities.

Nomenclature

N_{OG}, N_G, N_L – number of overall vapor-phase mass-transfer units, number of vapor-phase units, number of liquid phase mass-transfer units;

$K_{OG}, a, k_G, a, k_L, a$ – overall volume mass-transfer coefficient, vapor phase volume mass-transfer coefficient, liquid phase volume mass-transfer coefficient, s^{-1} ;

$\lambda = \frac{m \cdot G}{L}$ – diffusion potential;

m – slope of vapor-liquid equilibrium line;

G and L – vapor and liquid flow rate, kmol/s;

K_{OG}, k_G, k_L – overall mass-transfer coefficient based on vapor, vapor-phase, and liquid-phase mass-transfer coefficients, m/s;

a – interfacial area per unit volume of two-phase dispersion m^2/m^3 ;

t_G, t_L – holdup time of vapor and liquid phases in the gas-liquid layer, s;

C_1, C_2 – constants in the studied model determined by processing experimental and calculated data;

θ_G – contact time, time that each elementary vapor volume spends on the interfacial area, s;

h_L – clear liquid height on a sieve tray, m;

LPR% – the percent of liquid-phase resistance over total mass-transfer resistance;

h_W – outlet weir height, m;

p – pitch of holes in a sieve tray, m;

ρ_G, ρ_L – vapor and liquid phase densities, kg/m^3 ;

b – length of overflow threshold per unit working (bubbling) area of the tray, m^{-1} ;

W_V – vapor velocity relative to the working area of the tray, m/s;

F_s – load factor, $F_s =$ superficial F-factor, $kg^{0.5}/(m^{0.5} \cdot s)$;

ϕ – fractional perforated tray area;

σ – surface tension, N/m^2 ;

A and B – variables calculated using equations (17) and (18), respectively;

FP – flow parameter under total reflux conditions

$$FP = \left(\frac{\rho_G}{\rho_L} \right)^{0.5}$$

REFERENCES

1. J. F. Richardson, J. H. Harker, J. R. Backhurst, *Particle Technology and Separation Processes*, **2**, 542 (2006).
2. M. Pilling, D. R. Summers, *AIChE CEP Journal*, **November**, 32 (2012).
3. F. S. Engel, H. Klein, S. Rehfeldt, *Chem. Eng. Res. Des.*, **194**, 478 (2023).
<https://doi.org/10.1016/j.cherd.2023.04.055>.
4. R. Brahem, A. Royon-Lebeaud, D. Legendre, *Chem. Eng. Sci.*, **126**, 517 (2015).
<http://dx.doi.org/10.1016/j.ces.2014.12.010>.
5. S. R. Syeda, A. Afacan, K. T. Chuang, *Chem. Eng. Res. Des. Trans IChemE.*, **85 (A2)**, 269 (2007).
<https://doi.org/10.1205/cherd06111>.
6. T. L. Dominique, A. R. Secchi, T. F. Mendes, *2nd Mercosur Congr. Chem. Eng. 4th Mercosur Congr. Procs. Sys. Eng.*, 1 (2005).
7. A. Ujile, L. G. Amgbo, *Intern. J. Eng. and Technol. (IJET)*, **3(8)**, 787 (2013).
8. J. H. Lamprecht, Thesis of master of engineering (Chemical Engineering), Faculty of Engineering at Stellenbosch University, 2017.
9. E. Ch. Uys, PhD Thesis of Chemical Engineering, Faculty of Engineering at Stellenbosch University, 2012.
10. G. X. Chen, K. T. Chuang, *Ind. Eng. Chem. Res.*, **32**, 701 (1993).
11. Zh. Ivanov, M. Karaivanova, D. Georgiev, *Proceed. Univ. Ruse*, **56 (10.1)**, 51 (2017).
12. M. Karaivanova, PhD Thesis of Chemical Engineering, Prof. Dr Assen Zlatarov University, Burgas, 2016.
13. M. Karaivanova, D. Koleva, *Intern. J. Adv. Res.*, **11(03)**, 1082 (2023).
<http://dx.doi.org/10.21474/IJAR01/16538>.
14. F. J. Zuiderweg, *Chem. Eng. Sci.*, **37(10)**, 1441 (1982).
15. K. E. Porter, J. D. Jenkins, *Inst. Chem. Eng. Symp.*, **56**, 5.1/1 (1979).

Influence of the synthesis surfactants on the electrochemical and physicochemical properties of copper zinc tin sulfide

S. Stankov, K. Banov, O. Kostadinova*

Institute of Electrochemistry and Energy Systems "Acad. Evgeni Budevski" - Bulgarian Academy of Sciences, Acad. Georgi Bonchev Str., Block 10, 1113 Sofia, Bulgaria

Received: January 23, 2024; Revised: March 18, 2024

Cu₂ZnSnS₄ (CZTS) materials were obtained using two synthesis protocols. Ascorbic acid (ASC sample) and polyvinylpyrrolidone (PVP sample) were used as surfactants. X-ray diffraction data reveal a single phase CZTS (kesterite) material for the PVP sample, while the ASC sample is a mixture of Cu₂ZnSnS₄, ZnS, ascorbic acid and possibly Cu₂SnS₃. UV-vis spectroscopy was used in complementary manner in order to determine the presence of ascorbic acid in ASC final product. The morphology shows particles of 2-5 nm "fused" in larger agglomerates. The delivered initial capacities are 1148 mAh g⁻¹ (ASC) and 1141 mAh g⁻¹ (PVP). The capacity loss is more than 90% for ~12 cycles for both samples. The conversion of Cu₂ZnSnS₄ to Li₂S and alloys seems to be partially reversible, most likely due to Li₂S dissolution in the electrolyte.

Keywords: solution-processed materials, eco-friendly surfactants, ascorbic acid, polyvinylpyrrolidone, Cu₂ZnSnS₄, Li-ion battery

INTRODUCTION

Sustainable energy sources hold the key for the future economic, secure and ecology-oriented worldwide progress [1-5]. The major challenges that need to be overcome concerning the "green" energy sources are increased efficiency, conversion and storage. This trend is valid at full strength for lithium-ion batteries. Being devices capable of storing energy and releasing it on demand, their usage extends from commercial electronics and transportation, to industrial and power-storage applications [6-8]. Extensively studied during 1980s and commercialized in early 1990s, graphite (and its variations) is a dominant anode material for commercial lithium-ion batteries (LIB) with aprotic electrolytes [8, 9]. As a matter of fact, anodes have a vital role in improving the electrochemical LIBs performance. However, graphite and its derivatives confine the delivered power and energy density [9]. Therefore, approaches for further development pass by searching of alternative anode materials. Materials that exhibit higher energies and power densities include metal oxides (Fe₂O₃, SnO₂, Li₄Ti₅O₁₂), metals, and metalloids (Si, Sn, and Ge), as the Sn-based compounds (already mentioned SnO₂ and also SnS₂, SnSb, FeSn₂) being among the most widely investigated [8, 9]. Yet, these materials suffer from high volume expansion issues during lithiation and delithiation processes leading to severe structure degradation, which in turn results in short cycle life and low rate capability [9].

Lately, another family has drawn significant attention as potential candidates for LIB anodes, namely the multicomponent copper-containing semiconductor chalcogenides, Cu₂ZnSnS₄ (CZTS) in particular. An important advantage of these semiconductors is their tolerability to solution-processing synthesis, which is an economically viable alternative of vacuum-based methods due to lower electricity consumption and consequently, lower environmental impact [10].

Therefore, the aim of the present work is the comparative study of solution-processed Cu₂ZnSnS₄ materials obtained *via* two different eco-friendly synthesis protocols using different surfactants: ascorbic acid and polyvinylpyrrolidone.

EXPERIMENTAL

Synthesis of CZTS material

Copper zinc tin sulfides were obtained through a sol-gel method followed by solvothermal conditions. Two different synthesis protocols were employed to prepare the materials.

Synthesis 1 (ASC sample)

In separate beakers 4.55 mmol Cu(CH₃COO)₂·H₂O (98+% Alfa Aesar), 2.275 mmol Zn(CH₃COO)₂·2H₂O (98%, VWR), 2.275 mmol SnCl₂·2H₂O (98%, Merck), 2.5 mmol L-(+)-ascorbic acid (99% Alfa Aesar) and 9.1 mmol thiourea (Sigma Aldrich, 99%) were dissolved in 50 ml of C₂H₅OH (96%, Valerus, Bulgaria) each, at 50 °C and constantly stirred. Ascorbic acid was used as

* To whom all correspondence should be sent:
E-mail: ofeliya.kostadinova@iees.bas.bg

a capping agent to suppress the single crystal growth of CZTS during the solvothermal synthesis. The solutions of copper and zinc acetates (sol 1) were mixed followed by the ones of ascorbic acid and thiourea (sol 2). Thereafter, sol 1 and sol 2 were slowly mixed. The $\text{SnCl}_2 \cdot 2\text{H}_2\text{O}$ solution was added to the newly formed main solution. The final solution was evaporated at $80\text{ }^\circ\text{C}$ and constantly stirred upon reaching 40 ml, then left to cool down to room temperature. To this solution was added 40 ml ethylene glycol (99%, Valerus) then the mixture was transferred into a 100 ml Teflon-lined autoclave at $200\text{ }^\circ\text{C}$ for 24 h. After cooling to room temperature, the suspension was filtered and washed with deionized water several times. This sample was denoted as ASC.

Synthesis 2 (PVP sample)

1.02 mmol SnCl_4 (98% Alfa Aesar), 0.51 mmol $\text{CuCl}_2 \cdot 2\text{H}_2\text{O}$ (99% Alfa Aesar) and 0.51 mmol ZnCl_2 (98% Alfa Aesar) were added to 20 ml ethylene glycol (99%, Valerus) at room temperature and constant stirring. After complete dissolution of the precursors, 5.1 mmol thiourea was added to the solution and stirred for *ca.* 10 min until completely dissolved. Finally, 0.0026 mmol polyvinylpyrrolidone MW 40000 (PVP, Alfa Aesar) was employed as a capping agent. The volume of the solution was supplemented to 50 ml with ethylene glycol and transferred into a 100 ml Teflon-lined autoclave at $200\text{ }^\circ\text{C}$ for 24 h. After cooling to room temperature, the suspension was filtered and washed with deionized water several times. This sample was denoted as PVP.

CZTS characterization

X-ray powder diffraction (XRD) data of the samples were collected on a Philips APD 15 diffractometer, using $\text{Cu K}\alpha$ radiation ($\lambda = 1.5418\text{ \AA}$). UV-visible spectra were recorded of two drops of the CZTS colloidal solutions ($\sim 4.5\text{ mg cm}^{-3}$) diluted in 2 ml of deionized water using Metash UV-5800 spectrophotometer. The morphology of the material was observed by transmission electron microscopy (TEM) on JEOL JEM 2100, 80-200 kV.

Electrochemical testing in a lithium system

The active materials (AM) were tested electrochemically in a two-electrode laboratory cell. The working electrodes were prepared by mixing the active material, PVDF (Alfa Aesar) and carbon

black (CB) in N-methyl-2-pyrrolidone (NMP). The ratio of the slurry in wt.% was 70:10:20 (AM:PVDF:CB). The slurry was stirred for $\sim 24\text{ h}$ and then cast onto copper foil. The electrodes were dried in an oven at $60\text{ }^\circ\text{C}$ for 24 h under air. Cells were assembled in an argon filled glove box ($< 0.1\text{ ppm H}_2\text{O}$ and $< 0.1\text{ ppm O}_2$) using lithium foil as the counter electrode, Whatman (GF/C) separator soaked in 1M LiPF_6 in a 1:1 (v/v) mixture of ethylene carbonate (EC) and dimethyl carbonate (DMC) as an electrolyte. The assembled cells were left for six hours at rest mode before the electrochemical measurements in order to ensure good electrolyte penetration in the pores of the AMs. Constant Current Constant Voltage (CCCV mode) tests were performed on Neware BTS (model: CT-4008-5V10mA-164) in the voltage ranges 0.05 - 3.0 V vs. Li/Li^+ at 15 mA g^{-1} . The end condition for the constant voltage in CCCV mode was decrease of the current to 20% of initial current used during galvanostatic charge. Cyclic voltammetry (CV) was performed on a Multi PalmSens4 (PalmSens BV) multi-channel potentiostat/galvanostat, in the voltage range 0.05 - 3.0 V vs. Li/Li^+ , with a sweep rate of 0.05 mV s^{-1} , where the counter Li electrode was also used as a reference, as its polarization is negligible.

RESULTS AND DISCUSSION

The XRD data of the samples fitted well to the tetragonal structure of $\text{Cu}_2\text{ZnSnS}_4$ (Figures 1a and 1b) with space group I-42m (ICSD 171983). Additional peaks are observed in the ASC sample (Figure 1a), which correspond to ZnS with hexagonal symmetry and space group P63mc (ICSD 31076). The presence of Cu_2SnS_3 (ICSD 50965) is very probable as a compensatory phase considering that the stoichiometric calculations were performed for $\text{Cu}_2\text{ZnSnS}_4$ product and the appearance of ZnS. However, closer look in the patterns disclosed that it is hard to determine whether Cu_2SnS_3 is present due to the reflection positions overlapping with $\text{Cu}_2\text{ZnSnS}_4$ phase (Figure 1a). Moreover, there is a peak at $\sim 20^\circ 2\theta$ (asterisk in Figure 1a) implying presence of ascorbic acid [11] although the ASC sample was filtered and washed several times. A peak at $\sim 255\text{ nm}$ in the UV-vis spectra (Figure 1c) shows further evidence for ascorbic acid residue in the final material [12]. The extracted band gap from Tauc plot (Figure 1c inset) was found to be 5.8 eV and 5.5 eV for ASC and PVP, respectively.

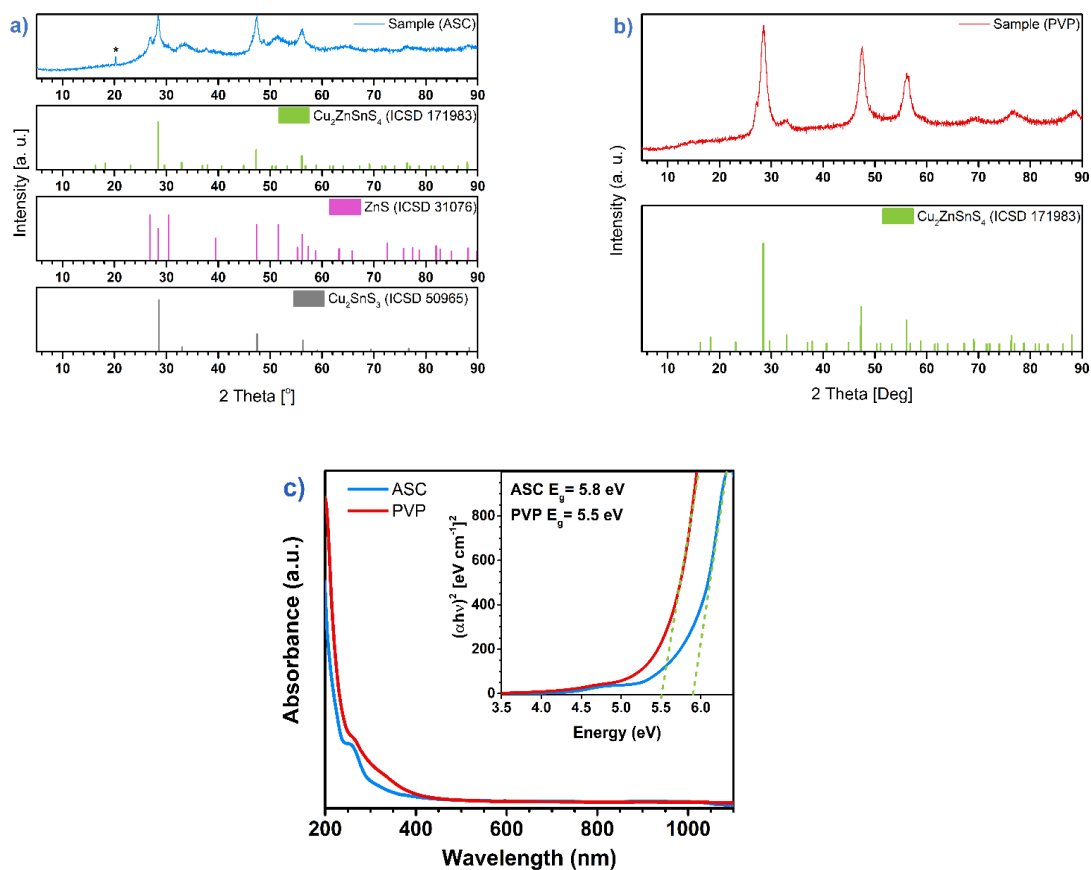


Figure 1. XRD patterns of (a) ASC and (b) PVP samples; c) UV-vis absorption spectrum and Tauc plots to determine the optical band gap (inset graph)

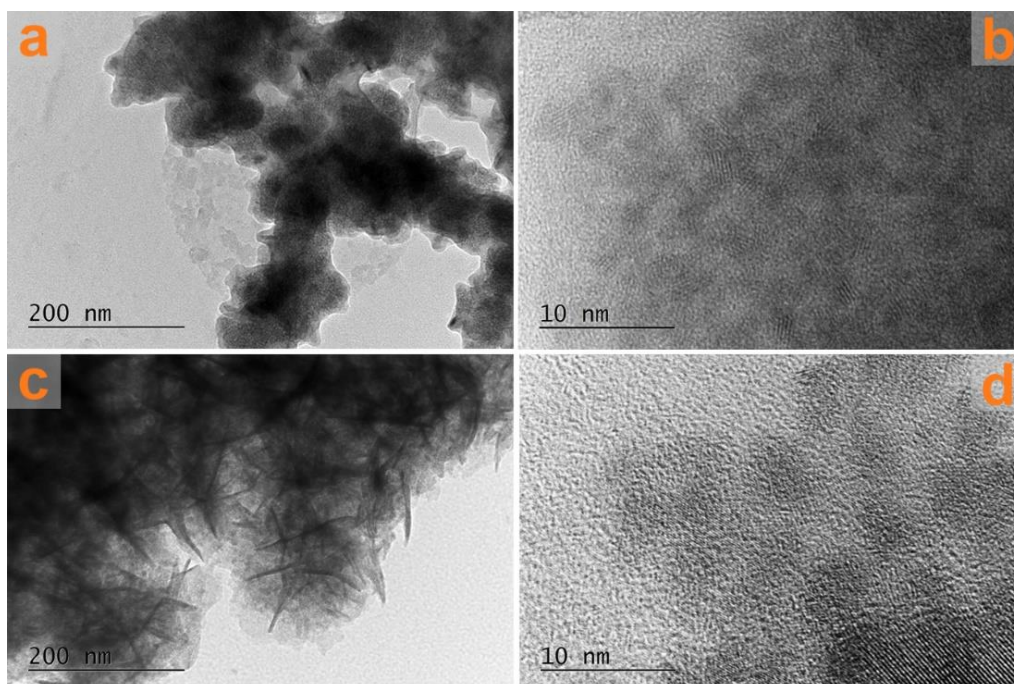


Figure 2. TEM micrographs of (a-b) ASC and (c-d) PVP

The TEM images of the two samples reveal presence of bulk agglomerates (Figures 2a and 2c). It is an evident flower-like morphology of the PVP agglomerates (Figure 2c). Both samples show agglomerates composed of nanoparticles with size of 2-5 nm (Figures 2 b and 2d).

Cyclic voltammetry (CV) was carried out at a scan rate of $0.05 \text{ mV}\cdot\text{s}^{-1}$ in the potential range 0.05–3.00 V vs. Li/Li⁺ in order to verify the electrochemical activity of the synthesized material (Figure 3).

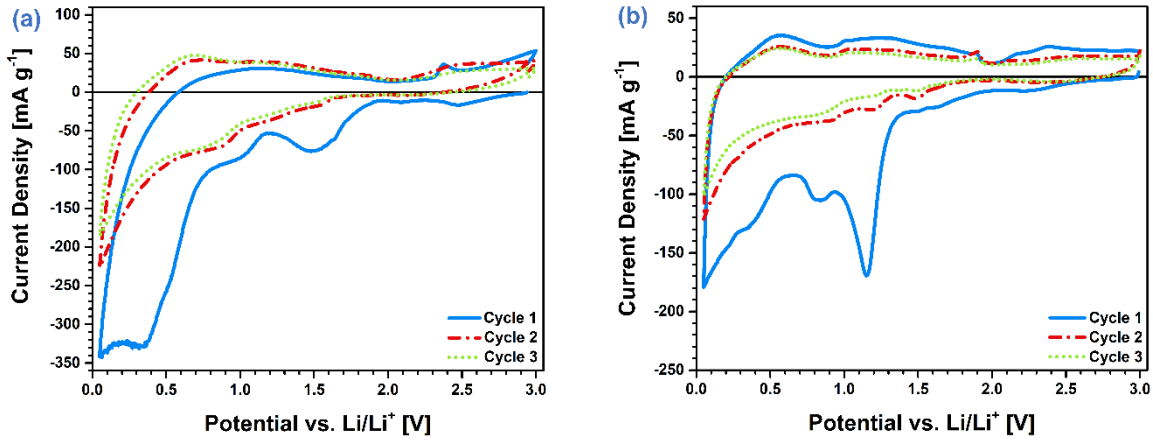


Figure 3. Cyclic voltammetry of (a) ASC and (b) PVP in the voltage range 0.05–3.00 V vs. Li/Li⁺ at a scan rate of 0.05 mV s^{-1} .

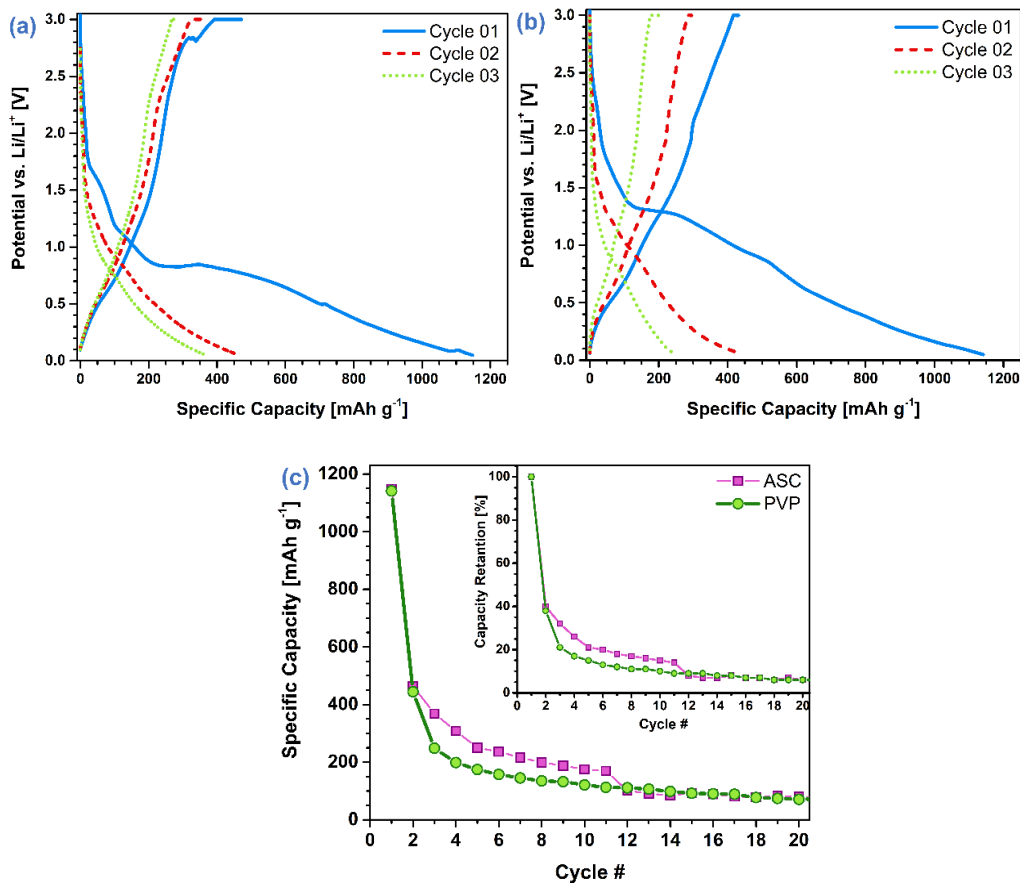


Figure 4. Galvanostatic tests: charge-discharge profiles in the voltage range 0.05–3.00 V vs. Li/Li⁺ (a) ASC and (b) PVP; (c) specific discharge capacity and capacity retention (inset) as a function of the cycles.

The electrochemical mechanism of these chalcogenide compounds is *via* conversion instead

of intercalation, which leads to formation of Li₂S and Cu-Zn/Cu-Sn alloys during the reduction process

[13]. The tested materials show different reduction curves. ASC first peak appears at 1.5 V vs. Li/Li⁺ followed by one at ~1 V vs. Li/Li⁺ and two strongly pronounced at 0.35 V and 0.05 V vs. Li/Li⁺ (Figure 3a). In contrast, PVP shows two strongly (at 1.15 V and 0.05 V) and two slightly pronounced (at 0.82 V and 0.35 V vs. Li/Li⁺) peaks (Figure 3b). The reduction curve of PVP sample seems to have closer resemblance to the reported in literature [9, 14-16] in comparison to the material synthesized with ascorbic acid. The reduction curve shape of ASC is most likely caused by ascorbic acid ligands on the surface of the active material particles, which prevent lithiation at higher potentials. Another contributor to the electrochemical behavior might be the ZnS phase, which main reduction electrochemical activity is within the 0.5-0.0 V vs. Li/Li⁺ range with peak maximum at 0.15 V vs. Li/Li⁺ [17]. Indirect proof for the presence of Cu₂SnS₃ phase in the ASC sample comes from the broad reduction peak at ~1.5 V vs. Li/Li⁺. The main electrochemical activity of Cu₂SnS₃ occurs in the ranges 1.5-1.0 and 0.5-0.05 V vs. Li/Li⁺ [6, 7, 18]. The oxidation curves of both materials are similar showing much lesser current density, which indicates poor reversibility. Peaks disappearance and current density decrease after the first cycle are evident. However, the materials performance stabilizes in the next cycles.

The performance of ASC and PVP materials was evaluated by employing galvanostatic tests at 15 mA g⁻¹ in the 0.05–3.00 V vs. Li/Li⁺ range (Figure 4). The first discharge curve plateaus are observed at different potentials: ~0.8 V (Figure 4a) and ~1.3 V (Figure 4b) for ASC and PVP, respectively. Both samples exhibit similar initial discharge specific capacities of 1148 mAh g⁻¹ (ASC) and 1141 mAh g⁻¹ (PVP) while the following charge capacities are less than a half (472 mAh g⁻¹ for ASC and 431 mAh g⁻¹ for PVP) indicating poor reversibility. The ASC shows slightly better performance in the first 10 cycles, thereafter both materials have similar outputs (Figure 4c). The capacity loss is more than 90% for ~12 cycles for the two CZTS samples (Figure 4c inset). Apparently, the conversion of Cu₂ZnSnS₄ to Li₂S and alloys seems to be partially reversible most likely due to the Li₂S dissolution in the electrolyte [19].

CONCLUSIONS

The present work is a comparative study of solution-processed Cu₂ZnSnS₄ materials obtained via two different eco-friendly synthesis protocols and surfactants: ascorbic acid (ASC) and polyvinylpyrrolidone (PVP). The X-ray diffractograms of both materials were indexed as Cu₂ZnSnS₄ phase with tetragonal structure.

However, additional peaks were observed in the ASC sample corresponding to ZnS, ascorbic acid and possibly Cu₂SnS₃. Further proof for the presence of ascorbic acid came from UV-vis spectroscopy. The morphology of the two samples consists of agglomerates composed of nanoparticles with size of 2-5 nm. The CV shows two different reduction curves for the studied samples. The PVP reduction curve shape is closer to that reported in literature, while the ASC behavior is most likely affected by the presence of ascorbic acid and ZnS. The galvanostatic tests displayed high initial capacities of 1148 mAh g⁻¹ (ASC) and 1141 mAh g⁻¹ (PVP). However, the capacity loss over the cycles is significant for both materials.

Acknowledgement: This study is funded by the Bulgarian National Science Fund (BNSF) under the scope of the “Competition for financial support of basic research projects on societal challenges 2018” program within the research project “Multifunctional Applications of Composite Graphene-Quantum Dots Systems (MULTIGRAPH)” contract No KII-06-OIIP04/2 14.12.2018.

REFERENCES

1. F. Chien, L. Huang, W. Zhao, *Journal of Innovation & Knowledge*, **8**, 100298 (2023).
2. F. Teng, Z. Ding, Z. Hu, P. Sarikprueck, *IEEE Transactions on Industry Applications*, **56**, 5684 (2020).
3. M. Andrei, P. Thollander, A. Sannö, *Renewable and Sustainable Energy Reviews*, **159**, 112168 (2022).
4. S. R. Paramati, U. Shahzad, B. Doğan, *Renewable and Sustainable Energy Reviews*, **153**, 111735 (2022).
5. I. Javid, A. Chauhan, S. Thappa, S. K. Verma, Y. Anand, A. Sawhney, V.V. Tyagi, S. Anand, *Journal of Cleaner Production*, **309**, 127304 (2021).
6. B. Qu, H. Li, M. Zhang, L. Mei, L. Chen, Y. Wang, Q. Li, T. Wang, *Nanoscale*, **3**, 4389 (2011).
7. J. Lin, J.-M. Lim, D. H. Youn, K. Kawashima, J.-H. Kim, Y. Liu, H. Guo, G. Henkelman, A. Heller, C.B. Mullins, *ACS Nano*, **11**, 10347 (2017).
8. J. Li, J. Shen, Z. Li, X. Li, Z. Sun, Z. Hu, S. Huang, *Materials Letters*, **92**, 330 (2013).
9. Z. Syum, T. Billo, A. Sabbah, A.K. Anbalagan, S. Quadir, A. G. Hailemariam, P. Sabhapathy, C.-H. Lee, H.-L. Wu, L.-C. Chen, K.-H. Chen, *Chemical Engineering Journal*, **465**, 142786 (2023).
10. S. Engberg, F. Martinho, M. Gansukh, A. Protti, R. Küngas, E. Stamate, O. Hansen, S. Canulescu, J. Schou, *Scientific Reports*, **10**, 20749 (2020).
11. B. Nicolăi, M. Barrio, J. L. Tamarit, R. Céolin, I. B. Rietveld, *The European Physical Journal Special Topics*, **226**, 905 (2017).

12. A. Gęgotek, E. Ambrożewicz, A. Jastrząb, I. Jarocka-Karpowicz, E. Skrzydlewska, *Archives of Dermatological Research*, **311**, 203 (2019).
13. B. Venugopal, Z. Syum, S.-Y. Yu, A. Sabbah, I. Shown, C.-W. Chu, L.-C. Chen, C.-H. Lee, H.-L. Wu, K.-H. Chen, *ACS Omega*, **7**, 9152 (2022).
14. X. Yang, J. Xu, L. Xi, Y. Yao, Q. Yang, C. Y. Chung, C.-S. Lee, *Journal of Nanoparticle Research*, **14**, 931 (2012).
15. Q. Jiang, X. Chen, H. Gao, C. Feng, Z. Guo, *Electrochimica Acta*, **190**, 703 (2016).
16. W.-H. Zhou, Y.-L. Zhou, J. Feng, J.-W. Zhang, S.-X. Wu, X.-C. Guo, X. Cao, *Chemical Physics Letters*, **546**, 115 (2012).
17. Q. H. Nguyen, T. Park, J. Hur, *Nanomaterials*, **9**, 1221 (2019).
18. X. Chen, J. Lin, Y. Chen, J. Zhang, H. Jiang, F. Qiu, R. Chu, H. Guo, *Journal of Alloys and Compounds*, **842**, 155619 (2020).
19. B. Jache, B. Mogwitz, F. Klein, P. Adelhelm, *Journal of Power Sources*, **247**, 703 (2014).

Acknowledgement to Reviewers for vol. 55 (2023)

The Editors of the *Bulgarian Chemical Communications* would like to take this opportunity to thank you for the effort and expertise that you contributed to reviewing, without which it would be impossible to maintain the high standards of our journal:

A	E	I		S
A. Eliyas	E. Bala	I. Hinkov	M. Mitov	S. Manev
A. Gendjova	E. Chorbadzhiyska	I. Ivanova	M. Mladenov	S. R. Bt. Hassan
A. Girginov	E. Ganev	I. Al-Saraieh	M. Nedyalkov	S. Singh
A. Kaçal	E. Razkazova	I. Stambolova	M. Ruskova	S. Sivakumar
A. Momchilov	E. Yakar	K	M. Shopska	Sv. Zhivkova
A. Popova	F	K. Nikolova	N	T
A. Stoyanova	F. Khanramaki	K. Petrov	N. Bozhkov	T. Petrova
A. Stoyanova-Ivanova	G	K. Yogendra	N. Kaneva	U
B	G. Atanasova	L	N. Stamenov	U. Kolak
B. Tsyntsarski	G. Gergov	L. Antipova	N. Velitchkova-Keskinova	V
B. Tzaneva	G. Kadinov	L. Vladimirova	P	V. Beschkov
C	G. Marinova	M	P. Mandjukov	V. Manev
C. Rosmini	G. Radeva	M. Aleksandrova	P. Popova	V. Simeonov
D	H	M. Atanasova	Krumova	Y
D. Karashanova	H. Badaruddin-Ahmad	M. Lazarova	P. Denev	Y. Rasouli
D. Vyas			R	Z
			R. Athlingham	Z. Nikfarjam
			R. Rajesh	

Instructions about Preparation of Manuscripts

General remarks: Manuscripts are submitted in English by e-mail. The text must be prepared in A4 format sheets using Times New Roman font size 11, normal character spacing. The manuscript should not exceed 15 pages (about 3500 words), including photographs, tables, drawings, formulae, etc. Authors are requested to use margins of 2 cm on all sides.

Manuscripts should be subdivided into labelled sections, e.g. INTRODUCTION, EXPERIMENTAL, RESULTS AND DISCUSSION, *etc.* **The title page** comprises headline, author(s)' names and affiliations, abstract and key words. Attention is drawn to the following:

a) **The title** of the manuscript should reflect concisely the purpose and findings of the work. Abbreviations, symbols, chemical formulae, references and footnotes should be avoided. If indispensable, abbreviations and formulae should be given in parentheses immediately after the respective full form.

b) **The author(s)**' first and middle name initials and family name in full should be given, followed by the address (or addresses) of the contributing laboratory (laboratories). **The affiliation** of the author(s) should be listed in detail (no abbreviations!). The author to whom correspondence and/or inquiries should be sent should be indicated by an asterisk (*) with e-mail address.

The abstract should be self-explanatory and intelligible without any references to the text and containing up to 250 words. It should be followed by keywords (up to six).

References should be numbered sequentially in the order, in which they are cited in the text. The numbers in the text should be enclosed in brackets [2], [5, 6], [9–12], etc., set on the text line. References are to be listed in numerical order on a separate sheet. All references are to be given in Latin letters. The names of the authors are given without inversion. Titles of journals must be abbreviated according to Chemical Abstracts and given in italics, the volume is typed in bold, the initial page is given and the year in parentheses. Attention is drawn to the following conventions: a) The names of all authors of a certain publications should be given. The use of "*et al.*" in the list of references is not acceptable; b) Only the initials of the first and middle names should be given. In the manuscripts, the reference to author(s) of cited works should be made without giving initials, e.g. "Bush and Smith [7] pioneered...". If the reference carries the names of three or more authors it should be quoted as "Bush *et al.* [7]", if Bush is the first author, or as "Bush and co-workers [7]", if Bush is the senior author.

Footnotes should be reduced to a minimum. Each footnote should be typed double-spaced at the bottom of the page, on which its subject is first mentioned. **Tables** are numbered with Arabic numerals on the left-hand top. Each table should be referred to in the text. Column headings should be as short as possible but they must define units unambiguously. The units are to be separated from the preceding symbols by a comma or brackets. Note: The following format should be used when figures, equations, *etc.* are referred to the text (followed by the respective numbers): Fig., Eqns., Table, Scheme.

Schemes and figures. Each manuscript should contain or be accompanied by the respective illustrative material, as well as by the respective figure captions in a separate file. As far as presentation of units is concerned, SI units are to be used. However, some non-SI units are also acceptable, such as °C, ml, l, etc. Avoid using more than 6 (12 for review articles) figures in the manuscript. Since most of the illustrative materials are to be presented as 8-cm wide pictures, attention should be paid that all axis titles, numerals, legend(s) and texts are legible.

The authors are required to submit the text with a list of three individuals and their e-mail addresses that can be considered by the Editors as potential reviewers. Please note that the reviewers should be outside the authors' own institution or organization. The Editorial Board of the journal is not obliged to accept these proposals.

The authors are asked to submit **the final text** (after the manuscript has been accepted for publication) in electronic form by e-mail. The main text, list of references, tables and figure captions should be saved in separate files (as *.rtf or *.doc) with clearly identifiable file names. It is essential that the name and version of the word-processing program and the format of the text files is clearly indicated. It is recommended that the pictures are presented in *.tif, *.jpg, *.cdr or *.bmp format.

The equations are written using "Equation Editor" and chemical reaction schemes are written using ISIS Draw or ChemDraw programme.

EXAMPLES FOR PRESENTATION OF REFERENCES

REFERENCES

1. D. S. Newsome, *Catal. Rev.–Sci. Eng.*, **21**, 275 (1980).
2. C.-H. Lin, C.-Y. Hsu, *J. Chem. Soc. Chem. Commun.*, 1479 (1992).
3. R. G. Parr, W. Yang, *Density Functional Theory of Atoms and Molecules*, Oxford Univ. Press, New York, 1989.
4. V. Ponec, G. C. Bond, *Catalysis by Metals and Alloys (Stud. Surf. Sci. Catal., vol. 95)*, Elsevier, Amsterdam, 1995.
5. G. Kadinov, S. Todorova, A. Palazov, in: *New Frontiers in Catalysis (Proc. 10th Int. Congr. Catal., Budapest (1992), L. Gucci, F. Solymosi, P. Tetenyi (eds.), Akademiai Kiado, Budapest, 1993, Part C, p. 2817.*
6. G. L. C. Maire, F. Garin, in: *Catalysis. Science and Technology*, J. R. Anderson, M. Boudart (eds.), vol. 6, Springer Verlag, Berlin, 1984, p. 161.
7. D. Pocknell, *GB Patent 2 207 355* (1949).
8. G. Angelov, PhD Thesis, UCTM, Sofia, 2001, pp. 121-126.
9. JCPDS International Center for Diffraction Data, *Power Diffraction File*, Swarthmore, PA, 1991.
10. *CA* **127**, 184 762q (1998).
11. P. Hou, H. Wise, *J. Catal.*, in press.
12. M. Sinev, private communication.
13. <http://www.chemweb.com/alchem/articles/1051611477211.html>.

Texts with references which do not match these requirements will not be considered for publication!!!

V. Slavova, Application of mobile fluorescence spectroscopy as a method in the determination of varietal differences in black radish (<i>Raphanus sativus</i> L. var. Niger) during storage under uncontrolled conditions	5
N. O. Appazov, M. I. Syzdykbayev, A. N. Appaz, E. A. Nazarov, K. Kh. Darmagambet, G. T. Balykbayeva, B. B. Abzhalelov, G. Sh. Askarova, Yu. A. Kim, Microwave activation of isovaleric acid monoglyceride synthesis and its antimicrobial activity	9
V. Slavova, Application of mobile fluorescence spectroscopy as a method for the analysis of representatives of different varieties of carrots (<i>Daucus carota</i>) during storage under uncontrolled conditions	14
<i>Selected papers presented on the Seventh International Scientific Conference Alternative Energy Sources, Materials and Technologies - AESMT'24, 14 - 15 May, 2024, Sofia, Bulgaria</i>	
D.N. Kolev, Increasing the energy efficiency of combustion processes using contact economizer systems and finned tube heat exchanger	21
A. Brusov, M. Azoulay, G. Orr, G. Golan, Influence of a weak pulsed magnetic field on the recovery and recrystallization in aluminum	27
A. Auce, A. Jermuss, A. Rucins, I. Auce, I.A. Horns, Solar and heat pump hybrid heated greenhouse in Latvia: energy storage and CO ₂ reduction	32
S. Bolegenova, A. Askarova, A. Georgiev, M. Beketayeva, S. Bolegenova, V. Maximov, N. Adilbayev, Selection of the optimal kinetic scheme for the formation of nitrogenous substances in the simulation of low-quality coal combustion	38
R. Płowens, M. Baraniak, K. Lota, J. Baraniak, M. Bajsert, G. Lota, carbon materials used as additives to active mass of semi-traction lead-acid batteries	44
<i>Selected papers presented on the seminar Sustainable Processes and Systems in Chemical and Biochemical Technologies - SPSChBT-2023, 30th November, 2023, Sofia, Bulgaria</i>	
K.Semkov, R. Darakchiev, T. Petrova, S. Darakchiev, Horizontal expanded metal sheet packing (Holpack) for mass and heat transfer processes in column apparatuses – study of research, mathematical modeling and industrial application	53
D.R. Koleva, M. K. Karaivanova, Modeling of rectification in a laboratory single-sieve tray column	76
S. Stankov, K. Banov, O. Kostadinova, Influence of the synthesis surfactants on the electrochemical and physicochemical properties of copper zinc tin sulfide	82
ACKNOWLEDGEMENT TO REVIEWERS FOR VOL. 55 (2023)	88
INSTRUCTIONS TO AUTHORS.....	89